COMPARING THE INVISCID AND VISCOUS FLOWS IN A SHOCK TUBE TO ANALYZE THE BOUNDARY LAYER EFFECTS

BY CHRISTEL M. SEITEL

A thesis submitted to the

Graduate School—New Brunswick

Rutgers, The State University of New Jersey

in partial fulfillment of the requirements

for the degree of

Master of Science

Graduate Program in Mechanical and Aerospace Engineering

Written under the direction of

Doyle D. Knight and Tobias Rossmann

and approved by

_____

_____

_____

New Brunswick, New Jersey

January, 2009

ABSTRACT OF THE THESIS

COMPARING THE INVISCID AND VISCOUS FLOWS IN A SHOCK TUBE TO ANALYZE THE BOUNDARY LAYER EFFECTS

by CHRISTEL M. SEITEL

Thesis Director: Doyle D. Knight and Tobias Rossmann

The purpose of the present work is to analyze the effects of viscosity in the Mechanical and Aerospace Engineering Undergraduate Laboratory shock tube at a pressure ratio (p_4/p_1) of approximately 1.54. Ten tests were performed at this ratio to check for consistency in the system. The experimental results from this facility were compared with results obtained from the typical shock tube equations, as well as computer simulations in Matlab and GASP. Among these methods, GASP was the only one which took viscosity into consideration. Multiple simulations were run with this program to determine the appropriate grid size (coarse or fine), as well as compare the inviscid and viscous results. The other methods (theory and Matlab) assumed a one-dimensional inviscid flow for simplification of the computation. The results showed that all of the data from the latter three methods matched relatively well for the flow in the center of the shock tube. However, near the wall, the viscous GASP computation showed a variation in density, temperature, and velocity, while the others remained at a constant value. This is due to the no-slip boundary condition at the walls used for the viscous flow. By taking a specific point along the shock tube with viscous flow and comparing the velocity profiles from when the incident wave

and when the reflected wave passes, it was discovered that a wall jet was created in the boundary layer. This jet moves in the opposite direction of the mainstream flow and at a much higher speed (more than 20 m/s greater).

Keywords: boundary layer, viscosity, shock tube, GASP

Acknowledgements

The first person that I need to thank is Dr. Tobias Rossmann. Under his supervision, I began my research in shock tubes with Dhaval. This was my first hands-on project at Rutgers University, and I learned a great deal about how to use the theory that was taught in class and apply it to a real world situation. With this came the use of understanding tolerances, machining parts on the shock tube, learning to seal connections and check for leaks, as well as learning software such as LabView. Dr. Rossmann was very helpful in providing guidance and making lots of suggestions about how to proceed when I was hopelessly lost. His open door policy also facilitated the process. I could not have had a better research experience.

I owe a great deal to Dr. Doyle Knight for picking me up and taking me under his wing when my research seemed to be going in circles. He suggested that I alter my topic to analyze the boundary layer effects, which is what is presented in this thesis. He helped to combine the experimental and computational aspects of the topic, so that I could get the best of both worlds. Dr. Knight was always willing to answer any question, no matter how simplistic or complicated, and made sure that the answer was understood before leaving. His belief that the best way to learn something is to teach it to someone else is something that I firmly believe, and one of life's lessons that will not be soon forgotten. His constant encouragement, support, and enthusiasm about the topic is what has kept me going to finish my research and write my thesis, as well as making sure that I did not give up on my quest for a job.

I am grateful that the Mechanical and Aerospace Engineering Department at Rutgers, with the suggestion from Dr. Haim Baruh, was able offer me a teaching assistant position for two years for the Design of Mechanical Systems class. It was a blessing and a burden, but it is the most rewarding class to be able to manage. The class taught me great deal about time management, how to resolve group conflicts, and everything that goes behind

creating a purchase order. I have never and will never regret accepting this position. I would love to personally thank all of the students who have made the class such a pleasure to instruct, but unfortunately there is not enough room for 213 names, so I hope that they will settle for this note.

I would also like to thank my family and friends for their continued support through the years. I am grateful for all of the people I have meet over the years at TKD. Many of us have grown up together to become a big family. Having the support and advice of so many people has helped make me who I am today and never let me forget where I came from. Aiesha, no matter how crazy things were, you would always find the time to help everyone and greet them with a smile. It is your kind words of encouragement and your heart of gold that show how much you care. Dhaval, it has been great to see a friendly face from day one during the Rutgers commuter/engineering orientation through our years in graduate school. I would not have been able to create my GASPex files and results without the help of Farnaz and Hadassah in B-112, and Reece Neel at Aerosoft Inc. Thanks to Kellie, who modified a file for me written in C, I had something to base my initial results on. For Jeremy, Sam, Joey, and Stefan, even though we are now miles apart, our phone conversations have kept us in touch. Thank you for your support to help me finish. A special thanks goes to Megan who sat across from me in D-115A. Through the ups and downs of graduate school, we have multiplied each other's happiness and divided our frustrations. I could not have asked for a better friend.

It is always the hardest to express how thankful you are to the people that mean the most to you. Words just cannot give the emotions behind them the justice they deserve. Ryan, my number one supporter through everything, has helped me to hang on and not give up no matter what the situation was. It is all of the little things that you do to make me laugh and try to get me to relax, that have kept me going through the long hours and difficult days. I am so grateful to have you in my life.

Table of Contents

List of Tables

List of Figures

Chapter 1

Introduction

1.1 Background

Aeronautics is the study of objects moving through the air, and aids in the design, construction, and maintenance of such vehicles. Aerodynamics, a branch of aeronautics, studies the flow of a fluid passed a body. Here, the gravitational forces can be ignored, and the viscous forces are considered to be only found in the thin boundary layer [11]. The flow can either be slow, with a Mach number less than 0.3 and where the compressibility effects can be neglected, or fast, where they cannot be. For Mach numbers greater than 1, the flow is considered to be supersonic, which originally proved difficult for man to attain. Before 1947, an airplane approaching the speed of sound encountered a "mysterious barrier" (later known as the sound barrier) which would cause it to be knocked about to the point that there would be no control over the plane's functions. The reason this occurred was because the sound waves created by the vehicle traveled faster than the plane could. This resulted in a time fluctuating boundary layer separation which was coupled with the development of shock waves on its wings and body [14]. The unsteady airflow around the plane would ultimately cause it to crash. It also proved difficult for some aircrafts to penetrate the sound barrier because their engines did not have enough thrust to overcome the rise in drag encountered in the transonic region (the region between subsonic and supersonic flow) [14]. Finally, on October 14th, Captain Charles (Chuck) Yeager flew the first successful supersonic aircraft, the Bell XS-1, displayed in Figure 1.1 [8]. This aircraft was dropped from the bay of a B-29 bomber at an altitude of about 20,000 feet. At a Mach number of 0.95, it was found that small shock waves began to form over the top surface of the wings. Passing the sonic barrier at M = 1.06 and an altitude of 43,000 feet, a strong bow shock wave was created in front of the needle-like nose [8]. It was later realized that although for

low speed fluids a constant density can be assumed, this is not valid for high-speed flows. For these faster flows, the density can vary from the changes in pressure, implying that the flow is compressible, by multiple orders of magnitude [8].

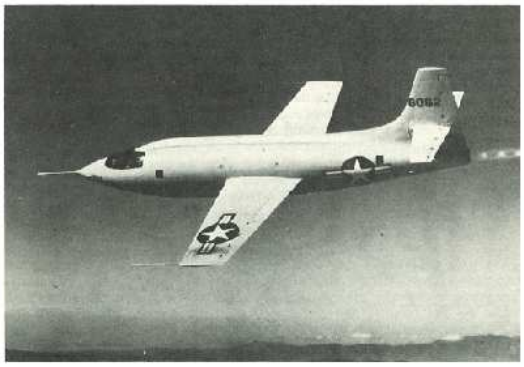

Figure 1.1: Image of the Bell XS-1, the first supersonic aircraft [8].

About 22 years later, on October 1, 1969, the Concorde (shown in Figure 1.2) made its first supersonic flight. Soon after, it was used for commercial services (beginning January 21, 1976). The appearance of the Concorde is much different than the Bell XS-1. The former has thin wings to reduce the drag and assist in delaying the shock wave formation. The wings are also angled back to decrease the drag even further to give the appearance that they are thinner in the airstream [1]. The latter, on the other hand, has a bullet-like shape with two straight, stubby wings attached [8]. Also, while the Bell XS-1 was only able to achieve Mach 1.06, the Concorde was capable of reaching a speed of Mach 2. Another 29 years later on October 12, 1998, the F-22 Raptor (displayed in Figure 1.3), a joint result of Lockheed Martin, Boeing, and Pratt & Whitney, flew over Edwards Air Force Base in California at Mach 1.1 during a three hour flight. Although this does not seem as impressive as the Mach 2 achieved by the Concorde, the flight did show advancement toward the ability to supercruise, or to fly without using afterburners for long periods at supersonic speeds [3]. By achieving this, the amount of fuel which is used during the flight is greatly reduced, unlike the Concorde which uses approximately 25,629 L or 6,771 gal per hour [1].

Although the intensity of shock waves that are produced on the body have been reduced

Figure 1.2: Image of the Concorde [2].

Figure 1.3: Image of the F-22 Raptor [4].

by taking various measures, such as altering the shape of the plane to follow a more sleek design, it does not completely eliminate them. In order to better understand shock waves, a shock tube can be utilized. A shock tube is a tube of either constant or varying cross-section, which is divided into a high pressure section and a low pressure section. When the barrier between them is ruptured, a shock wave is produced. The shock tube can serve multiple uses, such as a short-duration wind tunnel [12]. It can be used to produce quick changes in a fluid state so that observations in reaction rates, among others, can be made [12]. A shock tube can also be applied to determine the physical and chemical effects of high temperature gases [8]. Since the duration of the experiment is so small, the structure is not compromised from the sudden rise in temperature because there is not enough time for the heat to transfer to the metal. As a result, this facility can be used numerous times to check for repeatability of a given test.

The flow in a shock tube is typically approximated as generated by a moving piston. Here, the shock wave is represented as the piston being pushed in, thereby compressing the air, and the expansion wave is when the piston is being pulled out. For the shock, when the piston is moved, it causes a pressure wave to form and influences the gas directly ahead of it. As the piston continues to move, the first region sees an increase in pressure and velocity, causing the pressure wave to move down further, and again effecting the gas directly in front of it. Each of these pressure waves travels at the local speed of sound with respect to the fluid in which it is passing. Due to the higher pressure and velocity near the piston, the pressure waves here tend to overtake the ones that lie farther from the piston. This increasingly steeper wave profile will continue to grow until the pressure gradient becomes

infinite [16]. On the other hand, the wave profile becomes less steep as time passes for the expansion wave. As a result, the shock waves (or compression waves) create a discontinuity, whereas the expansion waves are unable to support this (due to its trend of flattening out with increasing time). Theoretically and experimentally, it has been found that a normal shock's thickness is on the order of 10^{-5} inches, which is comparable with the mean free path of the molecules [16]. Since this thickness is so small, the shock wave is considered to be a discontinuity so the properties that occur within it can be ignored.

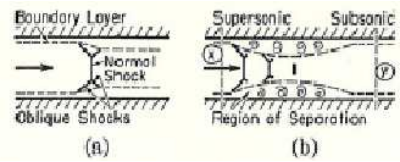

Figure 1.4: Shock-boundary layer interactions for (a) thin boundary layer and weak shock and (b) thick boundary layer and strong shock [16].

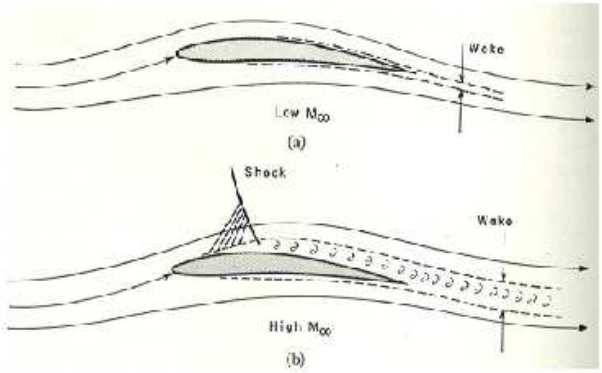

Figure 1.5: Flow passed an airfoil at (a) low Mach number (b) high Mach number [16].

For supersonic flow in a duct, the normal shock (a shock which is perpendicular to the walls through which the fluid flows) exerts a large adverse pressure gradient on the entire fluid motion [16]. The wall friction causes the boundary layer flow to form behind the shock. There are two typical shock-boundary layer interactions that can result, as shown in Figure 1.4. The first can usually be seen a little downstream from the throat

of a supersonic nozzle, where there is a weak shock and a thin boundary layer. Here, the normal shock almost extends over the entire cross-section, and the boundary layer becomes thicker [16]. The second interaction is for a strong shock and a thick boundary layer, which can be found in long ducts fed by supersonic nozzles. For this case, the flow separates from the walls, and then moves through a succession of accelerations and shocks. After the fluid slows down to subsonic speeds, it diverges and once again extends towards the walls. A similar phenomenon occurs with flow over an airfoil, where the adverse pressure gradient causes a quick thickening of the boundary layer. It can cause the flow to become turbulent, and also cause separation of the boundary layer from the airfoil (see Figure 1.5). This in turn results in the growth of the wake thickness. In essence, it alters the shape of the object, which typically will cause the lift to decrease and the drag to increase. Performing tests on a symmetric NACA 0012 wing at zero incidence, it was found that as the Mach number increased, the wake grew and there was a greater loss in total pressure, which was especially seen in the boundary layer [16]. These were the reasons why it proved to be challenging for an aircraft to reach supersonic speeds, and the forces that the Bell XS-1 and all of its successors must overcome.

1.2 Literature Review

1.2.1 The Shock-Boundary Layer Interaction

The interaction of a shock wave with the boundary layer, found in structures such as over-expanded nozzles, air intakes, and shock tubes, may result in a large regions of unsteady boundary layer detachment. This causes unsteady aerodynamic forces, mixing of the fluid(s) at the endwall thereby altering the test conditions, and also causes a reduction in the performance level [9]. In a shock tube, the shock wave accelerates the fluid to a finite velocity. The boundary layer is formed as a result of the viscous stresses acting on the fluid. As the boundary layer grows, the strength of the shock wave before reflection occurs is reduced [13]. Mark [13] has showed that in regions 1 and 3 (see Figure 1.6), the initial shock and reflected shock, respectively, the boundary layer stagnation pressure is greater than the pressure behind the undisturbed shock. Therefore, the fluid in the boundary layer

should pass under the shock and end up in the region behind the reflected shock. On the other hand, in region 2, the flow behind the initial shock, the stagnation pressure is greater than the pressure which is found behind the undisturbed *reflected* shock. In this case, the fluid from the boundary layer is collected in an area next to the foot of the shock [13]. After many experiments in this region (for $M_1 \geq 2$ and $M_{BL} \geq 1$, where M_{BL} is the Mach number of the fluid in the boundary layer), the trends could be summarized, and the result is illustrated in Figure 1.7. Here, the boundary layer flow travels through a normal shock, and afterwards is compressed subsonically to the stagnation pressure [13]. The diffusion angle is utilized to estimate the angle of the front leg of the interaction structure. The rear line separates the fluid which has passed through two oblique shocks and the flow that has only passed through the normal shock. The point where the shock and the two legs coming off it meet is referred to as the triple point. The Reynolds number (Re) is defined by Mark [13] in Eq (1.1). Here, the subscript w represents the density (ρ_w) and dynamic viscosity (μ_w) at the wall. The velocities of the reflected wave and initial shock wave are given as u_3 and u_1, respectively, and u_4 is the velocity of the wall in the frame of reference attached to the shock. Finally, x is the distance between the endwall and the reflected shock wave. For Reynolds numbers (Re) greater than 900,000, the trends of Figure 1.7 slowly alter to the point where only a normal shock with slight concavities near the wall is seen. This is assumed to be due to the flow becoming turbulent in the boundary layer [13].

$$Re = \frac{\rho_w (u_3 - u_4)^2 x [1 + u_1/u_4]}{\mu_w u_1} \tag{1.1}$$

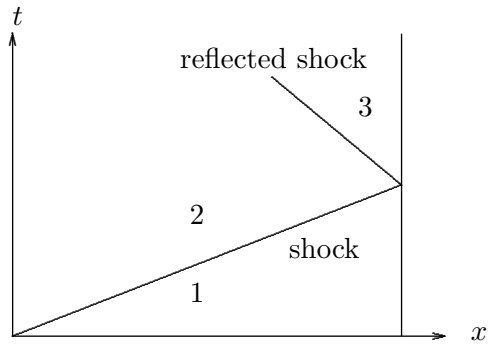

Figure 1.6: Diagram to illustrate the shock tube regions, according to Mark [13].

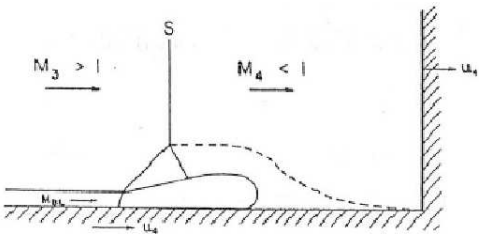

Figure 1.7: Interaction of the reflected shock wave with the boundary layer (Re $\leq$ 900,000) [13].

Effects of the shock-boundary layer interaction were also found computationally. In order to attain highly converged results to better record the discontinuities as well as smooth regions of the flow without increasing computation time, Daru and Tenaud [9] developed OSMP7. The boundary conditions used in the computations are summarized in Table 1.1. To test that the OSMP7 scheme was operating correctly, a one-dimensional inviscid condition was applied. As expected, the shock wave traveled through the low pressure side, followed by the contact surface (or contact discontinuity), whereas the expansion wave (or rarefaction wave) proceeded in the opposite direction. All of the calculations performed were with nondimensional terms, using the reference values of density, velocity, and length scale. The shock wave, traveling faster than the expansion wave, reached the endwall first and reflected off at about time $t = 0.21$, compared to $t = 0.5$ for the expansion, which is to be expected. This is because the velocity used to nondimensionalize the time is the same as the velocity of the expansion wave, *i.e.* the local speed of sound. Therefore, the only difference between the dimensional time and the properties used to make it nondimensional lies in the length scale. The length scale used represents the entire length of the tube, so only half is necessary for the expansion section because the diaphragm splits the tube into two equal pieces. Hence, the dimensionless time for the expansion wave to reach the endwall is 0.5. Shortly after leaving the wall, the reflected shock encounters the contact surface. As time advances, the reflected shock proceeds towards the expansion wave and reaches it at $t = 0.4$, whereas the contact surface remains near the endwall. A constant velocity exists during the reflected shock-contact surface interaction, but was found to decrease for the reflected shock-expansion wave interaction [9].

Table 1.1: Boundary conditions applied at the walls for computational tests run by Daru and Tenaud [9].

Property	Boundary Condition Applied
velocity components	no-slip
density	continuity equation
wall temperature	adiabatic
normal to the wall derivatives	4th-order upwind formula

Unlike the one-dimensional case, when the two-dimensional viscous test was computed,

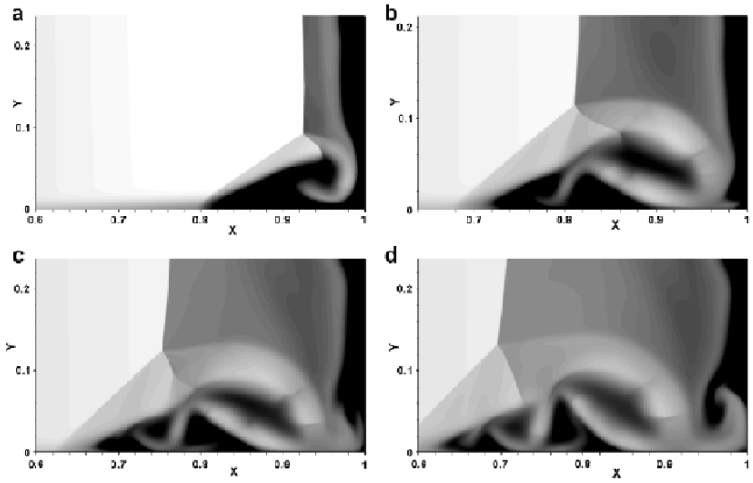

Figure 1.8: Temperature contours showing the interaction of the reflected shock wave with the boundary layer (Re = 200), at (a) $t = 0.4$, (b) $t = 0.6$, (c) $t = 0.7$, and (d) $t = 0.8$. (Note that a darker shade refers to a higher temperature.) [9]

a thin boundary layer was found to form on the tube walls due to the no-slip condition. Once the shock wave reaches the endwall, it reflects off and soon begins to interact with the boundary layer. It was found that in the boundary layer, the stagnation pressure was smaller than the pressure seen downstream of the normal shock [9]. The hotter fluid at the endwall quickly moves to the tube wall, thereby forming a hot countercurrent jet near the corner. This causes the flow to recirculate, thereby creating a "bubble" due to the separation of the boundary layer [9]. A lambda shock is formed as a consequence of cold fluid flowing above the slip line (or the supersonic shear layer) and the hot "bubble" below it. This phenomenon is illustrated in Figure 1.8a. Shortly after this time, the contact surface arrives and interacts with the reflected shock. The flow between the lambda shock and the wall jet curls around the bubble, thereby creating a high-speed cold jet. This jet then strikes the tube wall, closing the bubble and separating it from the endwall, where more hot fluid exists. As time progresses, the countercurrent part of the jet bounces between the tube wall and the supersonic shear layer, thereby forming counter-rotating vortices as shown in Figures 1.8b, c, and d [9]. There are three "layers" of fluid which comprise these vortices. The hottest shock fluid is contained in the middle. A colder fluid from the boundary layer surrounds the previous layer. The final layer, encompassing the

others, consists of the coldest layer which comes from the external flow at the periphery [9]. A high pressure region is created as a result of the jet flow, which reaches supersonic speeds in some areas, colliding with the wall or oblique slip line. This in turn causes the slip line to deform and secondary shock waves to be created above it [9].

1.2.2 Layered Experiments

For a closer look at the shock-boundary layer interactions, some researchers have, experimentally and computationally, created layers of fluid of different properties near the walls. For example, Reichenbach [15] created a setup which injected helium through a ceramic porous plate in the test section, creating a diffusion zone between the two gases (helium at the wall and air above it). For a constant temperature, since $\gamma_{He} = 1.667$ is greater than $\gamma_{air} = 1.4$ and $R_{He} = 2078$ J/kg*K is greater than $R_{air} = 287$ J/kg*K, the speed of sound is therefore greater for helium than for air. If a shock wave moves along a gas which has a higher speed of sound than that of atmospheric air, a precursor shock is created because the interaction of these gases causes the wave to refract ahead into this layer (i.e. the helium layer) [15]. A reflected wave is created from the interaction of the leading edge of the helium layer and the incident shock wave, and is labeled as A in Figure 1.9. Two triple points with corresponding sliplines were found to be created along with a Mach wave (labeled M, for the triple point TP' and the slip line SL') and a turning shock (labeled T, for TP and SL). A jet is formed when the gas between these two sliplines is moved down to the wall and then forced into a forward-oriented direction [15]. As shown in Figure 1.9, the layer of helium gas above the wall jet is rolled up in a counter-clockwise motion. After some time, the reflected wave (A) and the slip line (SL') reach the top of the test section and reflect off, beginning the transition phase, illustrated in Figure 1.10. It was found that if there was a sizeable difference in the velocity at the slipline, the flow here could change from laminar to turbulent [15]. As a result, the jet creates shocklets, or small shock waves. The Mach lines, formed on the left side of Figure 1.10, develop due to the rough surface of the ceramic plate. These lines also imply that the flow in the jet is supersonic [15].

Glowacki et al [17], performed a computational analysis using layers in a flow, but unlike Reichenbach [15] who used different gases, temperature layers were utilized. By increasing

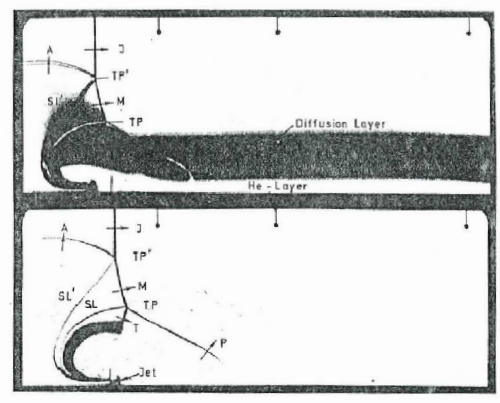

Figure 1.9: Precursor startup [15].

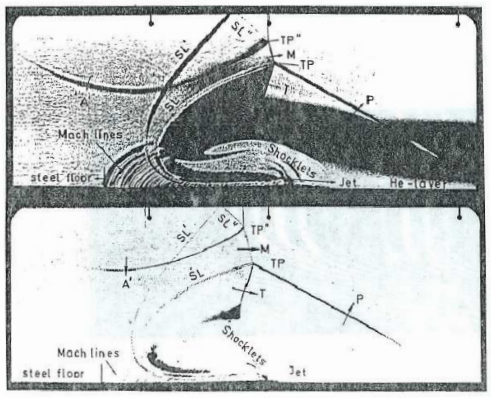

Figure 1.10: Transition phase [15].

the temperature, the speed of sound is increased, which will cause an oblique shock wave to form between the two temperature layers [17]. In one test, a thin layer (less than 10% of the height of the computational domain) was created close to the wall at a temperature of 2124 K (with a temperature ratio of the thin layer to the fluid above it equal to 7.25). Above this layer, the pressure ratio of the air across the shock was 3. The results of the density and pressure fields are shown in Figure 1.11. The density field shows that the cooler, ambient air moves under the higher temperature layer and rolls up with it creating a vortex. As this vortex travels with the shock in increasing time, it becomes larger in size [17]. The main shock, the oblique shock to the precursor (the pressure wave moving through the layer), and a second turning shock all meet to form the triple point, as illustrated in the pressure field graphs. It was found that the triple point, the precursor, the downstream tip of the vortex, and the stagnation point were found to move at a constant velocity, and therefore seem to imply a self-similar flowfield [17]. However, upon further investigation, the flowfield was found to be non-similar because of the "growth of complex and 'coherent' structures" [17]. A linear temperature distribution was also applied, where the temperature varied from 293 K on the border of the ambient air to the hotter temperature of 2124 K at the wall. The results were found to be similar to the thin layer case, previously discussed, where the cool air travels under the hot layer near the wall and rolls into a vortex [17].

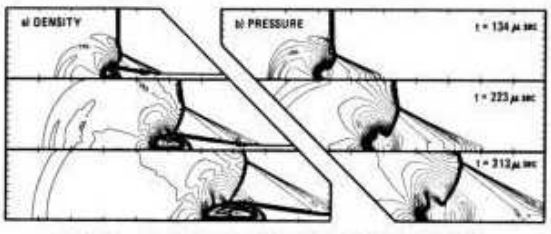

Figure 1.11: Density (left) and pressure (right) fields for a constant temperature layer [17].

1.2.3 Reducing the Effects of the Shock-Boundary Layer Interaction

Other experiments, such as those performed by Ligong, Gourlay, and Stalker [18], were focused on ways to decrease the test gas contamination due to the shock-boundary layer interactions. In order to accomplish this they proposed inserting slots, of widths that could be altered (0.35 - 1.0 mm), in each of the four walls of the square test section [18]. The intensity of suction could also be changed by moving the endwall of the test section. The experiment used air as the test gas along with piezoelectric transducers (to measure the transient pressures) and a schlieren system (for visualization of the flow). The purpose of having the slots before the reflected shock wave is to decrease boundary layer thickness at the wall caused by the shock wave, which in turn reduces the extent of the jet flow without altering the shock speed. The slots are also useful behind the reflected shock wave in order to eliminate the high speed jet of gas along the walls so it will not reach the end of the tube [18]. Performing the experiment without suction, it was found that after the shock wave passed, the boundary layer at the wall grew with time, which was to be expected. On the other hand, it was shown that increasing the suction velocity will decrease the boundary layer thickness. The amount of suction was also found to affect the reflected shock speed, in that the more suction that exists, the slower this wave travels [18]. It was also discovered that the height of the triple point of the bifurcation foot decreased with a large amount of suction, but was only minimally reduced with a small amount of suction [18]. This occurred due to the removal of some of the trapped gas, carried by the bifurcation foot by suction [18]. Suction increased the angle of the rear leg of the bifurcation foot (β), meaning that there existed a velocity component towards the wall. The size of the separation bubble was

also found to decrease due to the use of suction.

1.3 About the Thesis

1.3.1 Scope of the Thesis

In order to describe what occurs in a shock tube, it is typically assumed that the flow is inviscid and one-dimensional. This assumption greatly reduces the complexity of the fluid dynamics equations necessary to describe the flow in the tube. As a result, the pressure, density, temperature, and velocity can be easily determined. However, flow in a pipe has viscous effects due to interactions with the tube wall, and the endwalls where the waves reflect off and travel in the opposite direction. The purpose of this thesis is to examine the effects of viscosity on the unsteady flowfield in the Mechanical and Aerospace Engineering Undergraduate Laboratory shock tube.

Chapter 2

Problem Statement

2.1 Problem Statement

Although viscous effects take place in the shock tube, many times the problem is simplified and assumed to be inviscid. As a result, the one-dimensional fluid dynamics equations are utilized (to be discussed in Chapter 3) to determine the pressure, density, temperature, and velocity for various sections of the tube. The time for the shock wave and expansion wave to travel along the tube can also be computed. By comparing the experimental results with that obtained from the computational results, the assumption of inviscid effects will be tested to determine if it is valid.

2.1.1 The Experiment

The shock tube is comprised of two constant diameter sections, the driver side and the driven side, which are separated by a thin, plastic diaphragm. The shorter driver side is pressurized with 8 psig of air (22.69 psia), whereas the longer driven section is left at atmospheric conditions (14.69 psia). Once the diaphragm is broken, two pressure transducers, located in the driven section, record the voltage (later to be converted to pressure) and time for a given number of data points. From this information, all of the gas properties of the shock tube can be determined.

2.1.2 The Computation

Matlab

The computational program Matlab R2007a was used to compute the inviscid equations for comparison with the experimental results of pressure, density, temperature, and velocity

along the tube versus the tube distance (length of the tube). The only values necessary to solve these equations are the initial driver and driven pressures, the initial temperature in both of these sections, and the desired time during the experiment at which they would like to be viewed.

GASPex

The inviscid and viscous cases were analyzed with GASP. Here, the initial pressures and temperatures of the driver and driven sections were entered, as well as the boundary conditions and flow type (inviscid or laminar) which varied depending on which case was being solved. The pressure and time data points for a desired length of time were output during the run, for a specific location along the tube, corresponding to the location of the pressure transducers. The pressure, density, temperature, and tube-wise velocity (in the x-direction) in comparison to the distance along the tube (x-direction) and the tube diameter (y-direction) for a specific time can be output after the run is complete. The GASP results for the inviscid case were compared to that from Matlab to determine if the Matlab equations were solved correctly and to ensure that the correct boundary conditions were selected in GASP. These results could then be compared to the viscous case and the experimental results to determine if they are all in agreement and thereby conclude how valid is the inviscid assumption.

Chapter 3

Theory: Equations for the 1-D Case

3.1 The Shock Tube

The basic shock tube is comprised of two parts, denoted as the driver section and the driven section. The driver section contains the high pressure gas at pressure p_4, whereas the driven section holds the low pressure gas at p_1. These two sections are separated by a diaphragm, which is clamped into place, as illustrated in Figure 3.1.

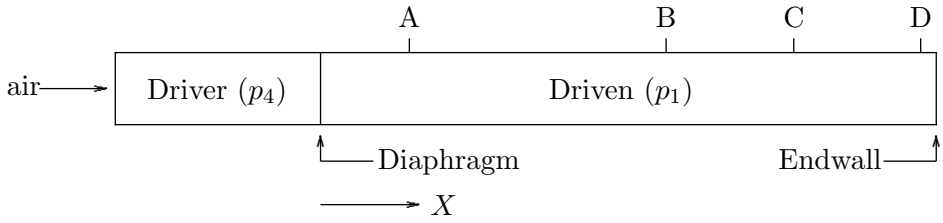

Figure 3.1: Diagram to illustrate experimental setup, labeling, and sign convention.

Once the desired pressures are reached on both sides, a plunger is inserted and the diaphragm is ruptured, thereby sending a shock wave through the driven section (to the right in the positive x direction) and an expansion wave through the driver section (to the left in the negative x direction). The region of the driven section in front of the shock wave is referred to as region 1, which is at rest and contains the initial properties of the gas. Likewise, region 4 has the initial properties of the gas in front of the expansion wave, as shown in Figure 3.2. Region 2 is the region behind the shock wave and is separated from region 3 by the contact surface. Region 3 represents how the expansion fan effects the gas properties. Once each of the waves reach the endwall, they are reflected back in the opposite direction as the same type of wave (*i.e.* a shock wave reflects as a shock wave, and an expansion wave as an expansion wave). Region 5 is the region behind the reflected shock wave.

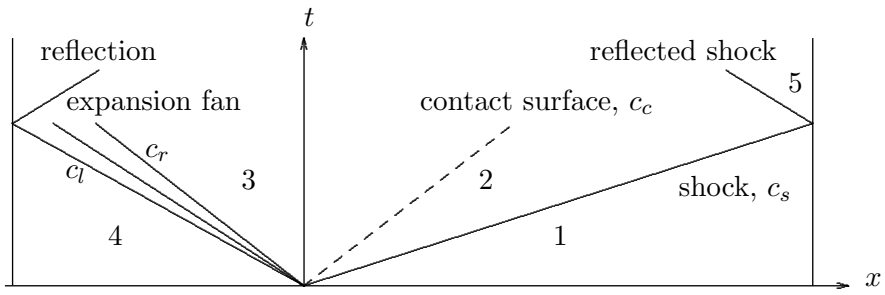

Figure 3.2: Shock propagating regions.

Since air was the only gas being used in both sections (driver and driven), certain properties and conditions were always constant. Table 3.1 lists these properties, where γ is the ratio of specific heats (and since $\gamma_4 = \gamma_1$ it will therefore only be referred to as γ from this point forward), R is the species gas constant, T is the temperature (of the room since the gas was not initially heated or cooled), and a is the speed of sound, calculated by using Eq (3.1).

$$a = \sqrt{\gamma RT} \tag{3.1}$$

Table 3.1: Known Properties

Constants	Values
$\gamma_4 = \gamma_1 = \gamma$	1.4
$R_4 = R_1$	287 J/kg*K
$T_4 = T_1$	290 K
$a_4 = a_1$	341.35 m/s

3.1.1 Pressure

Given all of the constants listed in Table 3.1 and knowing the initial pressures in the driver (p_4) and driven (p_1) sections, the basic shock tube equation, Eq (3.2), can be utilized to find p_2/p_1 [12]. This was accomplished by creating a Matlab code and utilizing the bisection function to iterate to the value of p_2/p_1 that would make the statement true. From this pressure ratio, also known as the shock strength, the pressure in region 2 (p_2) can easily be calculated.

$$\frac{p_4}{p_1} = \frac{p_2}{p_1}\left(1 - \frac{(\gamma-1)(a_1/a_4)(\frac{p_2}{p_1}-1)}{\sqrt{2\gamma}\sqrt{2\gamma+(\gamma+1)(\frac{p_2}{p_1}-1)}}\right)^{-2\gamma/(\gamma-1)} \tag{3.2}$$

The pressure on either side of the contact surface (regions 2 and 3) is always the same, meaning that $p_2 = p_3$. The expansion strength is the pressure ratio of p_3/p_4 and can be found by dividing the shock strength by the initial conditions of the driver and driven sections at which the shock tube was operating, Eq (3.3) [12].

$$\frac{p_3}{p_4} = \frac{p_2/p_1}{p_4/p_1} \tag{3.3}$$

3.1.2 Velocity

Just as with the pressures, the velocities are the same on either side of the contact surface (*i.e.* $u_2 = u_3$). Therefore, the velocities for regions 2 and 3 can be found using Eq (3.4) [12].

$$u_2 = u_3 = a_1\left(\frac{p_2}{p_1}-1\right)\sqrt{\frac{2/\gamma}{(\gamma+1)p_2/p_1+(\gamma-1)}} = \frac{2a_4}{\gamma-1}\left[1-\left(\frac{p_3}{p_4}\right)^{(\gamma-1)/(2\gamma)}\right] \tag{3.4}$$

The shock speed (c_s), or speed at which the shock wave is traveling at, is calculated by using the following equation, Eq (3.5) [10].

$$c_s = a_1\sqrt{\frac{(\gamma+1)}{2\gamma}\left(\frac{p_2}{p_1}-1\right)+1} \tag{3.5}$$

In order to calculate the speed to the left and right of the expansion fan, Eq (3.6) and Eq (3.7) [10] must be utilized, where the subscript l corresponds to the left side and r corresponds to the right. The negative sign in front of both equations is due to the sign convention developed for the shock tube (refer to Figure 3.1).

$$c_l = -a_4 \tag{3.6}$$

$$c_r = -a_4\left[\frac{\gamma+1}{\gamma-1}\left(\frac{p_2/p_1}{p_4/p_1}\right)^{(\gamma-1)/2\gamma} - \frac{2}{(\gamma-1)}\right] \tag{3.7}$$

The velocity of the contact surface is calculated by using the equation listed below, Eq (3.8) [10]. It is important to note that this is the same value as that calculated for u_2 and u_3 since, as previously mentioned, the velocity is not changing over the contact surface. The velocities of the shock wave, expansion fan (left and right), and contact surface (c_s, c_l, c_r, and c_c) are also labeled in Figure 3.2.

$$c_c = \frac{a_1}{\gamma}\left(\frac{p_2}{p_1} - 1\right)\left[\frac{(\gamma+1)}{2\gamma}\frac{p_2}{p_1} + \frac{(\gamma-1)}{2\gamma}\right]^{-1/2} \tag{3.8}$$

3.1.3 Temperature and Density

Although the pressure and velocity are the same across the contact surface, the temperature and density are different. This is because when the diaphragm bursts, the shock wave heats the flow as it travels into the driven section, whereas the expansion wave cools the flow as it travels back into the driver. The contact surface forms where the diaphragm used to be and therefore acts as a dividing line between these two sections. Eq (3.9) and Eq (3.10) are used to determine the temperature ratios, and thus, the temperatures on their respective sides of the contact surface [12].

$$\frac{T_3}{T_4} = \left(\frac{p_3}{p_4}\right)^{(\gamma-1)/\gamma} = \left(\frac{p_2/p_1}{p_4/p_1}\right)^{(\gamma-1)/\gamma} \tag{3.9}$$

$$\frac{T_2}{T_1} = \frac{1 + \frac{\gamma-1}{\gamma+1}\frac{p_2}{p_1}}{1 + \frac{\gamma-1}{\gamma+1}\frac{p_1}{p_2}} \tag{3.10}$$

By combining Eqs (3.9) and (3.10), the ratio of temperatures across the contact surface (T_3/T_2) can be obtained, Eq (3.11).

$$\frac{T_3}{T_2} = \frac{(T_3/T_4)T_4}{(T_2/T_1)T_1} = \left(\frac{T_3}{T_4}\right)\left(\frac{T_4}{T_1}\right)\left(\frac{T_2}{T_1}\right)^{-1} \tag{3.11}$$

Assuming that the gas is an ideal gas, the relation $p = \rho RT$ is valid (where R is the gas constant). Therefore, by remembering that $p_2 = p_3$, the density ratio (ρ_3/ρ_2) is found to be inversely related to the temperature ratio, Eq (3.12).

$$\frac{\rho_3}{\rho_2} = \left(\frac{T_3}{T_2}\right)^{-1} \tag{3.12}$$

3.1.4 Mach Number

The Mach number of the initial shock is defined as the shock speed c_s divided by the speed of sound in the driven section a_1 and is given by Eq (3.13). The Mach numbers in regions 2 and 3 are defined as the ratio of the fluid velocity to the speed of sound in the respective regions, and are given by Eqs (3.14) and (3.15). The speed of sound (a) for each Mach number is calculated by using Eq (3.1), where the only variable is the temperature for the given region. The equations for temperature, Eqs (3.9), (3.10), and (3.11), can be substituted into the Mach number equations, thereby making them dependent only on the pressure ratio p_2/p_1 and the constant γ. The Mach numbers of the shock, the flow behind the shock, and the flow behind the contact surface are thereby determined using equations, Eqs (3.13), (3.14), and (3.15), respectively [12].

$$M_1 = M_s = \frac{c_s}{a_1} = \sqrt{\frac{\gamma - 1}{2\gamma} + \frac{\gamma + 1}{2\gamma}\frac{p_2}{p_1}} \tag{3.13}$$

$$M_2 = \frac{u_2}{a_2} = \frac{1}{\gamma}\left(\frac{p_2}{p_1} - 1\right)\left[\frac{p_2}{p_1}\left(\frac{\gamma + 1}{2\gamma} + \frac{\gamma - 1}{2\gamma}\frac{p_2}{p_1}\right)\right]^{-1/2} \tag{3.14}$$

$$M_3 = \frac{u_3}{a_3} = \frac{2}{\gamma - 1}\left[\frac{p_4/p_1}{p_2/p_1}^{(\gamma-1)/2\gamma} - 1\right] \tag{3.15}$$

3.1.5 Reflection

Once the shock wave hits the endwall, it reflects back in the opposite direction. The Mach number of the reflected shock (M_r) is defined as the ratio of the flow velocity approaching the shock (relative to a frame of reference attached to the reflected shock) to the speed of sound of the flow approaching the reflected shock. The reflected Mach number is determined by using Eq (3.16). Since the speed of the gas into which the wave is moving is now u_2, the wave speed (W_r) can be found using Eq (3.17). The value obtained here is only the magnitude of W_r. Since the wave is traveling to the left, by the adopted sign convention, this value should be negative. The pressure ratio p_5/p_2 is found by combining the reflected continuity and momentum equations, Eqs (3.18) and (3.19), derived in Appendix A, thereby resulting in Eq 3.20, and since p_2 is known, the value of p_5 can also be determined [8].

$$\frac{M_r}{M_r^2-1} = \frac{M_s}{M_s^2-1}\sqrt{1+\frac{2(\gamma-1)}{(\gamma+1)^2}(M_s^2-1)\left(\gamma+\frac{1}{M_s^2}\right)} \tag{3.16}$$

$$W_r = M_r a_2 - u_2 \tag{3.17}$$

$$\text{continuity: } \rho_2(W_r+u_2) = \rho_5 W_r \tag{3.18}$$

$$\text{momentum: } p_2+\rho_2(W_r+u_2)^2 = p_5+\rho_5 W_r^2 \tag{3.19}$$

$$\frac{p_5}{p_2} = 1+M_r\left(\frac{p_2}{p_1}-1\right)\sqrt{\frac{2\gamma}{(p_2/p_1)[(\gamma+1)+(\gamma-1)(p_2/p_1)]}} \tag{3.20}$$

3.1.6 Time

The difference in time for the shock wave to travel from one pressure transducer to the other is calculated by Eq (3.21). The value for the distance between the pressure transducers (Δx_1) is known from the shock tube setup. Since the pressure transducers are not evenly spaced, it is important to know which transducers are taking the data so the correct values can be calculated.

$$\Delta t_1 = \frac{\Delta x_1}{c_s} \tag{3.21}$$

$$\Delta t_2 = \frac{\overrightarrow{\Delta x_2}}{c_s} + \frac{\overleftarrow{\Delta x_2}}{W_r} \tag{3.22}$$

The time it takes for the shock wave to pass the second transducer, travel to the endwall, reflect back, and once more pass the same transducer is calculated by breaking the times into the shock time difference (using c_s) and the reflected shock time difference (using W_r). The total time difference, denoted Δt_2, is the sum of these two terms, Eq (3.22), where Δx_2 refers to the distance from the second transducer to the endwall. The arrow placed over each term indictates the direction that the shock wave is traveling (the right-pointing arrow referring to the shock time difference where the shock is traveling to the right end of the tube, and the left-pointing arrow to the reflected shock time difference, where the shock is traveling to the left end of the tube).

Chapter 4

Methodology

4.1 Experiment

4.1.1 Equipment

Shock Tube

The aluminum shock tube used in this experiment has an inside diameter of 2.5 inches with a 0.25 inch wall thickness. A 0.001 inch thick mylar diaphragm, held in place by four latches, separates the longer (driven) section from the shorter (driver) section. The driver section is pressurized with air to 8 psig (or 22.69 psi, p_4), read by a digital pressure gauge. On the other side of the diaphragm, the air in the driven section of the shock tube remained at atmospheric conditions ($p_1 = 14.69$ psi). Since neither of the tube sections were initially heated, the temperature was taken to be the atmospheric room temperature (290 K), where $T_4 = T_1$. Since air was the only gas being used in both sections, certain properties were always constant, as previously listed in Table 3.1, Chapter 3. The driven section of the shock tube has four pressure transducers attached to it to record the data during the experiment. Figure 4.1 displays the location of these transducers with respect to each tube section, and Table 4.1 lists all of the shock tube dimensions including the distances between the pressure transducers.

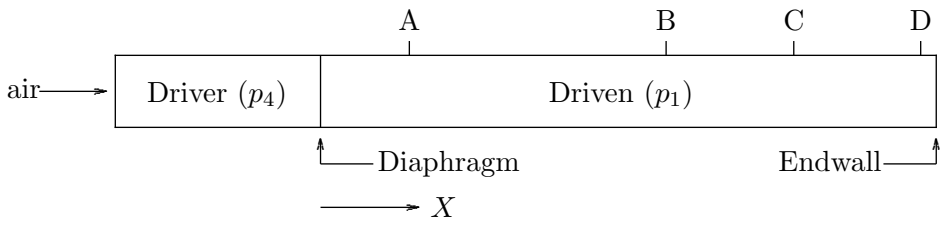

Figure 4.1: Diagram to illustrate experimental setup, labeling, and sign convention.

Table 4.1: Shock tube dimensions.

Object Measured	English (in)	Metric (cm)
L_{Driver}	39.5	100.33
L_{Driven}	103.875	263.84
Tube ID	2.5	6.35
Tube OD	3	7.62
A to B	43.375	110.173
B to C	21.563	54.769
C to D	21.438	54.451
D to Endwall	2.5	6.35

Pressure Transducers and Coupler

A sheath, which houses each pressure transducer, is screwed into threaded, tapered holes in the shock tube. The threads of this sheath are wrapped in teflon tape to prevent air from leaking out of the holes. Each of the four Kistler piezoelectric pressure transducers are inserted into one of these sheaths, so that the they are secured in place and that their bottom-most edge is flush with the inside wall of the shock tube. If the transducer edge were protruding or inset, this would disrupt the flow by causing an anomaly and thereby lead to false data readings.

The pressure transducers used can only measure changes in pressure (dynamic pressure) or pressure impulses. When the pressure rises from a passing shock, for example, the diaphragm at the bottom of the transducer deflects, thereby compressing the stack of alternating quartz plates and gold electrodes, which outputs a charge. The Kistler Piezotron Coupler 5126A converts this charge into a voltage, which is then transmitted to the oscilloscope. From the provided manufacturer's specifications of the pressure transducers, listed below as Eq (4.1), the voltage output (V) can be converted into a pressure (p) in units of psi, which can then be easily converted to N/m^2. The subscripts (A, B, C, D) correspond to the transducer that the data was read from (refer to Figure 4.1 for the shock tube location). Note that the term after the $\pm$ sign indicates the uncertainty in the pressure measurements.

$$
\begin{aligned}
p_A &= 14.69 + (20.800 \pm 0.207) V_A \\
p_B &= 14.69 + (18.471 \pm 0.185) V_B \\
p_C &= 14.69 + (35.200 \pm 0.411) V_C \\
p_D &= 14.69 + (18.389 \pm 0.184) V_D
\end{aligned}
\tag{4.1}
$$

Oscilloscope

The Hewlett Packard 54522A Oscilloscope is programed to continuously read in the voltage from the coupler. The data will begin to be recorded once the rising edge of the voltage it detects from the first transducer is increased above a certain point (20 mV DC for this experiment). At this point the system is considered to be "triggered". After all 1024 data points are collected at a rate of 50 kSa/s (50,000 samples per second), the system is "stopped" meaning that the system cannot be triggered again (unless reset), so no more data points are recorded or overwritten by reflected waves. The final results of voltage versus time are displayed on the oscilloscope screen. In order to better view these results, the two voltage traces can be offset from one another by shifting them horizontally on the screen. The data collected from each channel is then saved to a 3 1/2 inch floppy A as a text (.TXT) file.

4.1.2 Setup

When a test is run, air travels from the house air supply, through the air line and connects to the driver side of the shock tube. The rate at which the air enters the driver section is coarsely adjusted by slowly opening the ball valve. Once the pressure is close to the desired amount (8 psig), the regulator is used to finely adjust it. These pressures are measured by a pressure gauge with a digital readout, located between the regulator and the driver section as illustrated in Figure 4.2. This gauge only reads gauge pressure (the amount of pressure above atmospheric), so to obtain the absolute pressure, the atmospheric pressure of 14.69 psi must be added to the amount read on the display.

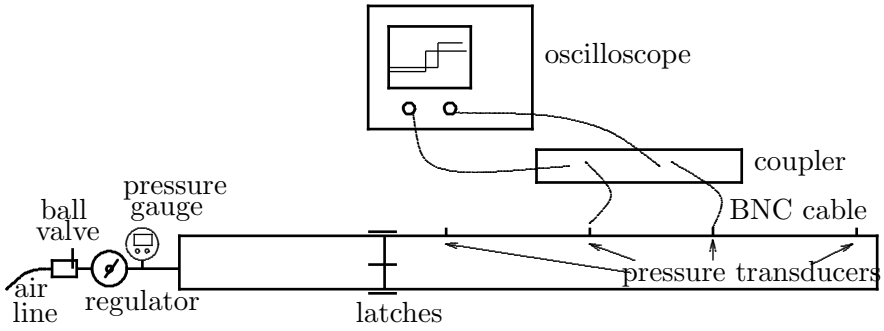

Figure 4.2: Diagram to illustrate experimental setup (not drawn to scale).

The pressure transducers (located on the driven section) are linked to the coupler via a connecting cable with a KIAG 10-32 positive end on the transducer side and a BNC positive end on the other side. The BNC end is inserted into one of the input slots of the coupler. Another connecting cable with a BNC positive end is placed in the corresponding output slot for a given transducer, and the other BNC positive end is connected to one of the channels of the oscilloscope. Since there are only two input slots for the oscilloscope, only data from two pressure transducers can be read at a time. Channel 1 corresponds to the transducer which is closest to the diaphragm location, whereas channel 2 is for the downstream transducer. In the current setup, transducers B and C will be used (Figure 4.1).

Once the desired pressure is obtained, a sharp plunger is carefully inserted into a hole in the driven section to break the diaphragm. Since the oscilloscope triggers off of a small rise in voltage (20 mV), the device must be checked right before this break to ensure that the system has not falsely been triggered, and therefore "stopped". If it has been triggered, the oscilloscope simply needs to be reset to once again await the trigger. After the diaphragm ruptures, a shock wave propagates to the right end of the tube (through the driven section) and an expansion wave travels to the left (through the driver section). When the shock wave reaches the first pressure transducer, the oscilloscope reads a voltage greater than the trigger limit, causing it to record the time and voltage for the specified number of time steps. Once complete, the data, also displayed on the screen, can be saved onto a disk to be transferred to a computer for analysis.

4.2 Computation

4.2.1 Matlab

A code was generated in Matlab to compute the basic shock tube equations for a given time depending on the region (or location on the shock tube) and the initial conditions listed in Table 4.2. The m-file outputs four ASCII format files containing the results of either non-dimensionalized pressure, density, temperature, or velocity versus a non-dimensionalized x coordinate in matrix form. The number of data points (n) to analyze between the driver end and driven end was taken to arbitrarily be 1000. The time (t) was chosen to be 0.00147 seconds, or half the time it takes the expansion to reach the driver endwall. The results for this time are to be compared to the results obtained from GASPex under the same conditions.

Table 4.2: Matlab initial conditions.

Properties	Values
p_4	22.69 psi = 156483 N/m^2
p_1	14.69 psi = 101325 N/m^2
L_{driver}	1.003 m
L_{driven}	2.638 m
γ	1.4
R	287 $J/kg * K$
$T_4 = T_1$	290 K
ρ_4	1.880 kg/m^3
ρ_1	1.217 kg/m^3
$u_4 = u_1$	0 m/s
$a_4 = a_1$	341.35 m/s

The shock strength (p_2/p_1) was found by using the basic shock tube equation, Eq (3.2) [12], and iterating it with the bisection Matlab function. Once determined, the expansion strength (p_3/p_4) can be found by taking the ratio of the shock strength and the ratio of the initial conditions, Eq (3.3) [12]. From these calculations, the pressures in regions 2 and 3 can easily be found and are equivalent since pressure does not change across the contact surface. The shock speed (c_s), the speed to the left and right of the expansion fan (c_l and c_r, respectively), and the speed of the contact surface (c_c) are calculated by using Eqs (3.5),

Table 4.3: Initial conditions entered into Matlab.

Properties	(1)	(n+1)	(n+2)
x	$-L_{driver}/(a_1 t)$	$x(n)$	$L_{driven}/(a_1 t)$
p	p_4/p_1	p_1/p_1	p_1/p_1
ρ	ρ_4/ρ_1	ρ_1/ρ_1	ρ_1/ρ_1
T	T_4/T_1	T_1/T_1	T_1/T_1
u	u_4/a_1	u_1/a_1	u_1/a_1

(3.6), (3.7), and (3.8), respectively [10].

For a better comparison, all properties calculated were non-dimensionalized by the property from region 1, as follows: streamwise distance along the tube (x) by $a_1 * t$, pressure (p) by p_1, density (ρ) by ρ_1, temperature (T) by T_1, and velocity (u) by a_1 since $u_1 = 0$ and would therefore be an unreasonable choice. The x values were calculated by using Eq (4.2). The position in the x vector is denoted by i which contains the integer values of 2 through n (where $n = 1000$ was chosen). Since the time is taken before either wave can strike the endwall, the values at these extremes are calculated outside of the loop and the formulas utilized are displayed in Table 4.3 for $x(1)$, $x(n+1)$, and $x(n+2)$. These data points are then added at the beginning ($i = 1$) or end ($i = n+1$ and $i = n+2$) of the corresponding property vectors in order to include the non-dimensionalized conditions of regions 1 and 4. This provides a more complete picture of what is occurring throughout the shock tube. It is important to note that all of the equations in this section are only valid for the times before any reflection (of either the expansion wave or shock wave) occurs.

$$x(i) = \frac{-a_4}{a_1} + \left[\left(\frac{c_s}{a_1} + \frac{a_4}{a_1}\right)\frac{1}{n-2}\right] * (i-2), \text{ for } i = 2, n \tag{4.2}$$

The shock wave and expansion fan, before reflection with the endwalls, separate the shock tube into 4 regions, where the properties in each of these regions is different. As a result, the Matlab code used conditional statements to determine which region the point was in, and then applied the proper formulas. For example, the driver section, Region 4, contained all x values that were less than or equal to c_l/a_1. The other areas include the expansion (between Regions 3 and 4), between the expansion and contact surface (Region 3), between the contact surface and shock (Region 2), and the driven section (Region 1).

The equations for the non-dimensionalized pressure, density, temperature, and velocity for each of these sections are listed as follows [10].

	$p = p_4/p_1$
in driver:	$\rho = \rho_4/\rho_1$
$x \leq \frac{c_l}{a_1}$	$T = T_4/T_1$
	$u = u_4/a_1$
	$p = \frac{p_4}{p_1}\left[\frac{(\gamma-1)}{(\gamma+1)}\frac{1}{a_4}\left(\frac{x}{t}-u_4\right)+\frac{2}{(\gamma+1)}\right]^{\frac{2\gamma}{(\gamma-1)}}$
in expansion:	$\rho = \frac{\rho_4}{\rho_1}\left(\frac{p}{p_4}\right)^{1/\gamma}$
$x \leq \frac{c_r}{a_1}$	$T = \frac{p}{\rho R T_1}$
	$u = \frac{2}{\gamma+1}\left(\frac{x}{t}+\frac{(\gamma-1)}{2}u_4+a_4\right)\frac{1}{a_1}$
	$p = p_3/p_1$
between expansion	$\rho = \rho_4/\rho_1\left(\frac{p_2}{p_4}\right)^{1/\gamma}$
& contact surface:	$T = \frac{p}{\rho R T_1}$
$x \leq \frac{c_c}{a_1}$	$u = c_c/a_1$
	$p = p_2/p_1$
between contact	$\rho = \rho_1/\rho_1\left[(\gamma-1)+(\gamma+1)\left(\frac{p_2}{p_1}\right)\right]\left[(\gamma+1)+(\gamma-1)\left(\frac{p_2}{p_1}\right)\right]^{-1}$
surface & shock:	$T = \frac{p}{\rho R T_1}$
$x \leq \frac{c_s}{a_1}$	$u = c_c/a_1$
	$p = p_1/p_1$
in driven:	$\rho = \rho_1/\rho_1$
$x \geq \frac{c_s}{a_1}$	$T = T_1/T_1$
	$u = u_1/a_1$

4.2.2 GASPex

Loading GASPex and Grid Generation

The General Aerodynamics Simulation Program (GASP) is a highly complex code that is used to solve computational fluid dynamics (CFD) problems. This program imports a set of data points that form a mesh. The data points are coordinates on a graph that, for this problem, create two rectangular shapes corresponding to the length of the driver and driven sections of the shock tube and the radius. Each rectangle is referred to as a zone by the program. The data points are arranged in a specific way so that they can be saved as a Plot3D (.P3D) grid, as required by GASP. A sample grid plot of a shock tube that contains two zones with dimensions of 0.5m x 0.25m and 1.0m x 0.25m, and its .P3D file are displayed in Figure B.1 (see Appendix B). The grid format begins by listing the total number of zones (2) to be input into the program. To be consistent with the previous sign convention and set up, Zone 1 was selected to represent the driver section and Zone 2 the driven section. Next, the maximum number of points in the x [$x_{max}(1) = 2$] and y directions [$y_{max}(1) = 2$] for Zone 1, and below for Zone 2 [$x_{max}(2) = 3$ and $y_{max}(2) = 2$] are displayed. Under this 4x4 matrix is a column of all of the data points, listed in the following order: all of the x values in Zone 1 repeated $y_{max}(1)$ times, then each y value of Zone 1 repeated $x_{max}(1)$ times, followed by the Zone 2 points written in a similar fashion.

Although the grid may be imported in either English or Metric units, as specified by the user, GASP internally stores the grid in Metric units [6]. GASP will also automatically convert all two-dimensional grids to three-dimensions because it utilizes three-dimensional control volumes [6]. Since, the shock tube is a 3-D cylindrical object, it was imported as a 2-D axi-symmetric problem. This takes the two 2-D rectangular zones and rotates it about the axis of symmetry, assumed to be the x-axis, an amount $+\pi/80$ and $-\pi/80$ (or +2.25 degrees and -2.25 degrees) [6]. The resulting 3-D object, which appears as a pie slice, is displayed in the Graphical User Interface (GUI). This slice is one of many sections that when placed tangent to each other, comprise the full cylindrical shape. When GASP computes the solution, each cell in this 3-D object is analyzed so the user is able to determine what is occurring at any point for any time between 0 seconds and the maximum

time for which the test was run.

File Tab

The reference quantities of density (ρ_{ref}), temperature (T_{ref}), velocity (V_{ref}), and length (L_{ref}) for the system are entered by the user under the File tab. These will help to non-dimensionalize the system for easier computation by reducing possibly problematic round-off error. From these four quantities, other reference quantities can be computed, to also non-dimensionalize them, such as pressure ($p_{ref} = \rho_{ref} * [V_{ref}V_{ref}]$), energy ($e_{ref} = V_{ref}V_{ref}$), and time ($t_{ref} = L_{ref}/V_{ref}$) [6]. Once the calculations are complete, the reference quantities will be re-applied so the results have their respective dimensions. Therefore, the values that are entered are arbitrary and will not change the solution if other values are used. The user must also indicate the units used for the reference quantities (English or Metric). These can be different than that used for the grid because GASPex will make the necessary conversions. Just as for the grid, the values will be converted, if necessary, and stored in Metric units. For the given setup, the values implemented and reasons of choice are:

$$density \ = \ 1.205 \ kg/m^3 \ : \text{approximate density of air at sea level}$$

$$temperature \ = \ 290 \ K \ : \text{initial temperature in driver and driven sections}$$

$$velocity \ = \ 341.35 \ m/s \ : \text{speed of sound with initial conditions}$$

$$length \ = \ 3.641725 \ m \ : \text{overall length of shock tube}$$

The gauge pressure write-in box, was left as equal to 0 N/m^2. This ensures that GASP will make all pressure calculations with the absolute pressure [6].

Flow Solver

The *Flow Solver* is the main folder in GASP's tree view under which all subfolders lie. It contains all information needed to solve the problem, from the initial conditions through the manner in which to export the solution. The first subfolder listed is the *Zones* folder. This folder contains one node for every zone imported from the Plot3D file (*i.e.* geogrid.P3D).

The nodes are labeled using this file name followed by chronological zone number (*i.e.* geogrid:1 and geogrid:2).

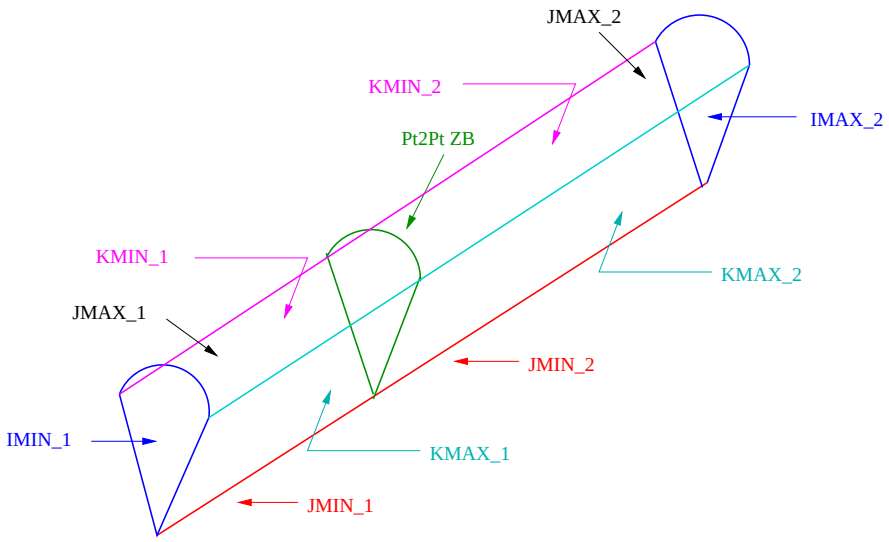

Figure 4.3: 2D axi-symmetric model seen in the GASPex viewing window with each side labeled.

When the grid is imported, all surfaces of the figure are labeled and put into the *Undefined* folder of the *Surfaces* subfolder. There are a total of twelve surfaces: the minimum and maximum boundaries for each direction (i, j, k), for each of the two zones (so each zone has six surfaces). They are labeled in a similar manner as the zones in the *Zones* subfolder, but it also contains the boundary (*i.e.* geogrid:1 IMAX). New folders are created under the *Surfaces* subfolder to group similar boundary conditions and initial conditions. These folders are labeled *Positive Axi-Symmetric*, *Negative Axi-Symmetric*, *Driver Side*, *Driven Side*, and *Axis*. The *Positive Axi-Symmetric* folder contains the KMAX values for both sections (in Figure 4.3, the face closest to the user, encased by the red, blue, cyan, and green lines). On the other hand, the *Negative Axi-Symmetric* folder contains the KMIN values for both sections (the face farther from the user, encased by the red, blue, magenta, and green lines). The *Driver Side* folder contains the IMIN boundary (the driver endwall) and JMAX boundary (the wall of the shock tube) from grid 1 (the left-most blue line, and left-most rounded section of the slice, encased by the blue, cyan, green, and magenta lines). The *Driven Side* folder contains the mirror image, about the vertical y-axis, of surfaces for

the driven section, namely, IMAX and JMAX for Zone 2 (same colors as Zone 1, but on the right-most side of the figure). The *Axis* folder contains the JMIN values for the driver and driven sections (denoted by the red line). The BC button next to each folder is toggled to activate the boundary condition to be specified and defined later.

Table 4.4: Folders for boundary conditions.

Sub-Folder: Folder Name	Surfaces Included	Side	Line Colors from Figure 4.3
Surfaces: Positive Axi-Symmetric	KMAX:1	left	red, blue, cyan, & green
	KMAX:2	right	red, blue, cyan, & green
Surfaces: Negative Axi-Symmetric	KMIN:1	left	red, blue, magenta, & green
	KMIN:2	right	red, blue, magenta, & green
Surfaces: Driver Side	IMIN:1	left	blue
	JMAX:1	left	blue, cyan, green, & magenta
Surfaces: Driven Side	IMAX:2	right	blue
	JMAX:2	right	blue, cyan, green, & magenta
Surfaces: Axis	JMIN:1	left	red
	JMIN:2	right	red
Zonal Boundaries: Pt2PtZB	IMAX:1::IMIN:2	-	green

The final boundary is for the area between the driver and driven sections (depicted by the green lines in Figure 4.3). Here, a point-to-point zonal boundary (denoted as Pt2PtZB in GASPex) is created under the Zonal Bouns tab by pressing the Compute Pt2PtZB button. The result(s) of this will automatically be put into the *Pt2PtZB* folder of the *Zonal Boundaries* subfolder. GASP determines if two zones share a border by checking if each of the four grid points of every cell face from each zone have the same location. This operates with a tolerance relative to the distance between two of the points being checked and is normalized by the size of the cell. If both zones are found to have a common boundary, the program recognizes that there are two sections connected together that could have different initial conditions, but will eventually have flow between them [6]. The two surfaces that matched these conditions were the IMAX surface from Zone 1 and the IMIN surface from Zone 2. A summary of all of the folders discussed above and the surfaces that they contain are listed in Table 4.4

The remaining folder of interest is the *All Output* folder. Under this folder, the user

creates subfolder(s) that contain all of the settings that are required for post-processing. In this manner, if multiple solutions wish to be observed under various conditions, such as at different times for different properties, each can be contained in a separate folder. Therefore, the settings do not have to be adjusted between computations.

Zones Tab

Initialization Tab

The Initialization tab is used to input the initial conditions. Each of the zones are listed separately so that they can reflect the different conditions in the driver and driven sections. These values will be selected once the Q specification (to be discussed shortly) is set up. Along with the zone name, the number of points (dimensions) for each zone are listed for the i, j, and k directions as Idim, Jdim, and Kdim, respectively, and therefore, determine the fineness of the grid. Although the Jdim and Kdim values are the same for both the driver and driven sections, the Idim values differ depending on the zone. This is because the dimensions that are imported correspond with the actual dimensions of the shock tube (where the driver is 1.0033 m long and the driven is 2.6384 m long, but there is a constant radius throughout both zones).

Sequencing Tab

The Sequencing tab is used to make the Fine Grid and Coarse Grid. The Fine Grid is the default setting and the only one originally listed. To create the Coarse Grid, another sequence is added by clicking New Sequences, Auto Sequence, and then Create Grids. By default, this changes the ILev and JLev values from 1 (in the Fine Grid) to 2, meaning that every other grid line will be used. This in turn, reduces the amount of time it takes for the solution to be found. Once the Coarse Grid has been solved, the solution can then be run for the Fine Grid with fewer iterations necessary. This tab also lists the same dimensions as the Initialization tab. Depending on which grid is used, these dimensions will differ by factors of each other. For example, the dimensions of the Coarse Grid will be half of the Fine Grid dimensions (because half of the grid lines have been removed from that sequence).

Physical Models Tab

The physics of the problem is numerically described with the Physical Models Tab. Here the Q specification, boundary conditions, and type of flow (inviscid, viscous, laminar, turbulent) are established.

QSpec

The Q specification (QSpec) is used to store flow conditions to be used as initial conditions or running conditions. The three properties that are required are density, either temperature or pressure, and either Mach number or velocity magnitude. The flow angles can be adjusted if desired, but the shock waves are assumed to be traveling along the length of the tube (*i.e.* following the x-axis), so the normalized default of $u/|V| = 1$ is used. From these properties, other flow variables can be calculated, such as mixture quantities (mixture density and the speed of sound), viscosity quantities (viscosity, thermal conductivity, and Reynolds number), and thermodynamic quantities (total temperature, total pressure, gamma, static energy, etc.). Two QSpecs were made, one for each zone of the shock tube (driver and driven). The initial conditions of pressure, Mach number, and density of their respective sections were entered in the type-in boxes in Metric units, and are listed in Table 4.5. Although the Mach number should be zero (since there is no initial flow), the program does not allow this because the velocity is used to compute other parameters and having a value of zero would cause a floating point exception (according to Reece Neel, employee of Aerosoft- the company that created GASP). Once the QSpec values are entered, the initial conditions can then be applied to the Initialization section of the Zones tab, by selecting the correct QSpec for each zone.

Table 4.5: Initial conditions entered into QSpec.

Section	Pressure $[N/m^2]$	Mach Number	Density $[kg/m^3]$
Driver	156483	1e-12	1.88013
Driven	101325	1e-12	1.21741

Boundary Conditions

All of the folders previously mentioned under the Flow Solver section (and displayed in Table 4.4) are listed under the Boundary Conditions tab, as long as they have been activated (BC button toggled). The flow boundary condition of the surfaces contained within the *Positive Axi-Symmetric* folder is Positive Axi-Symmetric Wall. This assumes that the flow is axi-symmetric and that the axis of symmetry lies about the x-axis [6]. Similarly, the *Negative Axi-Symmetric* folder has a Negative Axi-Symmetric Wall boundary condition. The X-Axis Axi-Symmetric condition is used for axi-symmetric flows where the x-axis and singular axis lie along the same line, and therefore, is applied to the *Axis* folder. The *Driver Side* and *Driven Side* folders will both have the same boundary conditions, which depend on whether the flow is considered to be inviscid or viscous. If it is inviscid, then the Tangency condition applies. This assumes that the flow is indeed inviscid and that the solid walls are impermeable [6]. On the other hand, if the flow is viscous, then the No Slip Adiabatic condition is utilized. This implies that for a viscous flow, the pressure and species densities are extrapolated such that the temperature gradient at the solid wall surface is equal to zero [6]. Table 4.6 summarizes the boundary conditions of all of the folders. The surfaces in the *Pt2PtZB* folder are not included in this section because the folder and its location already imply a "soft boundary" that is only temporarily there to separate the initial conditions (as previously mentioned).

Table 4.6: Boundary Conditions for Inviscid (I) and Viscous (V) Flows.

Folder Name	Flow Type	Boundary Condition	Flux	QSpec
Positive Axi-Symmetric	I/V	Positive Axi-Symmetric Wall	Full	-
Negative Axi-Symmetric	I/V	Negative Axi-Symmetric Wall	Full	-
Axis	I/V	X-Axis Axi-Symmetric	Split	-
Driver Side	I	Tangency	Full	-
Driver Side	V	No Slip Adiabatic	Full	Driver
Driven Side	I	Tangency	Full	-
Driven Side	V	No Slip Adiabatic	Full	Driven

After each boundary condition is chosen, GASP will select either a full or split flux setting to accompany it. For full flux, the value at the cell face will only depend on the

boundary value, meaning that it must reside on a physical surface [6]. Split flux differs because it looks at the state to both the left and right of the cell, one of which will be the boundary condition and the other is determined through interpolation. This flux will also create ghost cells, cells that only exist for computational purposes but have no physical meaning, to find the boundary state. As displayed in Table 4.6, the only one that has the split flux option is the *Axis* folder because it is the only surface that does not have any walls to enforce specific boundary conditions, or tangent surfaces (as the positive and negative axi-symmetric surfaces do).

For certain boundary conditions, additional information about the flow conditions may be required, as shown by the QSpec column in Table 4.6. The two sets of surfaces that require this lie in the *Driver Side* and *Driven Side* folders. As shown, this is only necessary for the viscous case and not for the inviscid case. In addition, the Tangency boundary condition will not effect the properties along the solid walls. However, the No Slip Adiabatic condition, requires the initial conditions to be able to complete the calculations and determine the viscous effects that are occurring by the walls.

Inviscid Tab

For the Global/Marching Strategy, the Global Iteration option was selected because it means that GASP will simultaneously solve for a solution over both of the zones. For the type of problem being solved, namely that of air traveling at or near the speed of sound (also known as a transonic problem), this selection is necessary because the hyperbolic nature of the governing equations causes the characteristic waves to move in every direction [6].

Although the number of dimensions for the given problem (*i.e.* 2-D) should match the number of active inviscid flux schemes (therefore, 2), for axi-symmetric problems, a scheme should be chosen for all three directions (i, j, k). The reasoning behind this is that when the fluxes are summed about each control volume, the fluxes in the third direction will not cancel each other [6]. The Roe scheme was selected for the i and j directions, whereas Full Flux was chosen for the k direction. The Roe flux-difference splitting scheme was chosen because it is one of the better choices for analyzing boundary layer flows, which was the major purpose of the experiment. This representation of the standard Roe formulation is

derived from characteristic wave disturbances and is capable of exactly attaining stationary discontinuities (such as shock waves) [6]. Originally, it was desired to use a No Flux scheme for the k direction because there were no fluxes of interest in this direction. However, when GASP was set to run the test, it failed. Through trial-and-error, it was discovered that the No Flux option was the cause of the error and the Full Flux option needed to be utilized instead. A Full Flux scheme is mainly used for problems requiring space marching (*i.e.* for supersonic flow traveling in one of the grid coordinate directions, where the flow may be efficiently "marched" downstream and each point is solved for by using the upstream points) [7]. Although it initially seemed incorrect to make this selection, the solutions that resulted were very similar to what was predicted.

After the flux scheme has been selected, the accuracy of this scheme must be chosen. For a finite volume, the cell averages are used to reconstruct a pointwise field. This is necessary because in order to determine the flux at the cell faces, the state variables at the cell faces must be known [6]. The accuracies at which this was calculated at were 2nd Order Upwind Biased for the i and j directions, and 1st order for the k direction. With these selections, a value of κ is inserted by default, as part of the MUSCL formulation (**M**onotone **U**pstream-centered **S**chemes for **C**onservation **L**aws), used to solve higher-order pointwise reconstruction [6]. Under this system, anything that falls within the bounds of $-1 \leq \kappa \leq 1$ is considered to need higher-order reconstruction. The 2nd Order Upwind Biased accuracy yields $\kappa = 0$, meaning that the solution performs a linear interpolation between the upstream and downstream cells [6]. For first order accuracy of the k direction, the κ value lies outside the previously mentioned range ($\kappa = 2$).

When solving a problem, the convergence, accuracy, and monotonicity (or the consistent increasing or decreasing of a series of terms) must be considered, but only two of the three can be implemented at a time [6]. For GASP's current setup, only accuracy (previously discussed) and monotonicity (controlled by limiters) are utilized. The limiters that were selected were Minimum-Modulus (Min-Mod) for the i and j directions, and No Limiter for the k direction. The Min-Mod limiter is used for higher-order computations and generates a 2nd order upwind interpolation, which matches the accuracy selection [5]. If the forward and backward gradients have the same sign, then the magnitude is taken and the smaller of

the two becomes the limit. However, if they are opposite signs, then the limit is taken to be zero [5]. This essentially looks at the bounds of the neighboring cell faces and ignores any reconstruction outside of them [6]. Although this can cause residual limit cycles, it proved to not be a problem in the computation and running of GASP. For 1st Order accuracy in the k direction, the only option that was available is No Limiter.

Viscous Tab

Under the Viscous Tab and within the Viscous Flux Mode option, the user specifies whether the flow is inviscid, laminar, or turbulent (the latter two referring to viscous flows). For the inviscid case, nothing else in this tab needs to be selected because it does not have any meaning or impact on the solution. The other case to be observed is for viscous laminar flow. It is essential that for wall bounded flows, the directions normal to a no-slip surface be selected (refer to Table 4.6 for a listing of the boundary conditions). The reason for this is because it will allow GASP to calculate the viscous fluxes on every cell face [6]. As a result, all three of the viscous flux terms, I-Direction, J-Direction, and K-Direction, are selected.

Under the Laminar Transport Properties section, the method in which to solve the problem must be selected for the Viscosity, Conductivity, and Diffusivity. For Viscosity, the only model available for selection is Sutherland's Viscosity Law (or Sutherland, as labeled in the program). This uses the "Sutherland curve fits for species laminar viscosity," where each species' viscosity is calculated by using a common equation [6]. Sutherland's Conductivity Law was chosen for the Conductivity model. The Sutherland curve fits are also utilized here, but this time as a function of temperature in order to determine the species conductivity [6]. The Diffusivity Model used the Constant Schmidt Number option, the only one available for selection. This is used to determine a binary diffusion coefficient, which is utilized by Fick's law of diffusion (a simpler form of the Stefan-Maxwell equations) to determine the species diffusion, assuming it acts as a binary mixture [6]. The binary diffusion coefficient (Di) is found by using $Di = \mu * Sc$, where Sc is the Schmidt number [6]. By default, the values for Prandtl number and Schmidt number are already entered into the type-in box as 0.72 and 0.7, respectively.

The final option to be selected under the Viscous tab is for the Wall-Gradient Calculations. Here the 2nd Order Accurate button should be toggled. This implies that at the physical boundary, the derivatives of the viscous terms will be computed with a one-sided, second-order accurate difference formula [6]. This option should always be used for the wall-gradient.

Thermo-Chem Tab

Under the Thermodynamics-Chemistry Tab, the Chemistry Model is used to describe the molecules that are present in the reaction and their reaction rate with respect to temperature [6]. Therefore, a perfect gas model was chosen because there is only one species, air (listed as Pgas under the Species title), in both the driver and driven sections, and therefore, no reactions take place. For similar reasons, the Chemistry Mode was selected to be frozen, and by default, the Reactions are listed as Frozen Flow - No Reactions. The Thermodynamics Model (or Thermo Model in GASP) is used to describe the molecules state of internal-energy in the flow [6]. From initial calculations and assumptions it was determined that the temperature during the experiment would not exceed 800 K. It was assumed that there was very little, if any, vibrational energy contribution, and could therefore be neglected [6]. As a result, the equilibrium translation and rotation option (abbreviated by GASP as Eq. Trans & Rot.) was selected. Finally, since the entire reaction occurs in such a short time (in a matter of milliseconds), there is no time for water in the air to condense in the shock tube, so the Condensation Model is selected to be None.

Run Definitions Tab

The Run Definitions tab is used to set up the manner in which GASPex will solve the given problem. Under the Main sub-tab, the Residual Output should be Global, and for the first run, the Current Sequence should be Coarse Grid. As previously mentioned, this will reduce the complexity and the time that it takes the program to solve the problem. The Current Sequence pull-down box is used to select the grid that GASP will use (*i.e.* fine, coarse, etc.). If multiple run definitions are created to match each sequence, then the Execute This Run Definition option should only be toggled for the one the user wishes

to currently solve. This will turn the font red in color, instead of the regular white, on the left side of the screen under the Run Definitions title. The Interp Solution Up option will interpolate the solution to the next sequence level one time after the run definition is complete.

Temporal and Solver Info

GASP is programed to solve the problem either as a steady state flow or as a time dependent flow [6]. The shock tube flow is an inherently unsteady problem. As a result, the Explicit Runge Kutta algorithm was chosen. The Explicit Runge Kutta, based on the Runge Kutta scheme, will advance the solution forward in time (from $t = 0$ seconds up to the final time). This algorithm requires that the accuracy be either 1st, 2nd, or 4th order, so 2nd order was chosen to be consistent with spatial accuracy, which is also 2nd order. Although the maximum time step allowed is smaller than Implicit Dual Time Stepping (the alternative to Runge Kutta), it requires less time to calculate one time step [6]. The only option available for the Run Type (under the Solver Information title) is Runge Kutta due to the temporal algorithm selected. The Flow Solver Type was chosen so that the results of the flow, instead of the sensitivity, could be determined.

Time Dependent and Convergence Info

The Time Dependency Information section allows the user to input the number of iterations to perform over a given time and how often to save the data. All of GASP's runs begin at time $t = 0$ seconds, and will finish when either the maximum number of steps (Max # of Steps) or the maximum time alloted (Max Time) is reached. The Max # of Steps is a function of the Max Time (a user defined value) and the time step (Δts) as shown in Eq (4.3).

$$\text{Max \# of Steps} = \frac{\text{Max Time}}{\Delta ts} \tag{4.3}$$

The Time Step input box is used by GASP to establish a constant time increment at which the program will move forward. The value used here must satisfy the Courant-Friedrichs-Lewy (or CFL) condition, as stated in Eq (4.4), where C is the Courant number and must be less than or equal to 1 (*i.e.* $C \leq 1$) [10].

$$C = \frac{\Delta ts}{\Delta t_{CFL}} \tag{4.4}$$

The denominator of Eq (4.4), Δt_{CFL}, is defined by Eq (4.5) [10]. Here, the numerator (Δx, Δy) refers to the grid spacing in either the x or y direction (where Δx = 5.017e-03 m, Δy = 2.9e-05 m) and λ is one of three eigenvalues (see Table 4.7) that come from the Jacobian matrix A. A is used in the non-conservative form of the 1-D Euler equation, Eq (4.6), which can also be written in the conservative form as Eq (4.7).

$$\Delta t_{CFL} = \min_i \frac{\Delta x,\, \Delta y}{|\lambda_i|} \tag{4.5}$$

$$\frac{\partial Q}{\partial t} + A\frac{\partial Q}{\partial x} = 0, \quad A = \frac{\partial F}{\partial Q} \tag{4.6}$$

$$\frac{\partial Q}{\partial t} + \frac{\partial F}{\partial x} = 0 \tag{4.7}$$

$$\begin{aligned} Q &= [Q_1\ Q_2\ Q_3]^T = [\rho\ \rho u\ \rho e]^T \\ \text{where} \quad F &= [F_1\ F_2\ F_3]^T \\ &= [\rho u \quad \rho uu + p \quad \rho eu + pu]^T \end{aligned}$$

Since the flow is initially at rest, the value of the velocity (u) in Table 4.7 is 0 m/s. The variable a, as previously mentioned, is the speed of sound in air ($a = \sqrt{\gamma RT}$ = 341.35 m/s).

Table 4.7: Eigenvalue equations and calculated values.

Equations	Results for u = 0 m/s
$\lambda_1 = u$	= 0 m/s
$\lambda_2 = u + a$	= 341.35 m/s
$\lambda_3 = u - a$	= -341.35 m/s

There are two different estimates for the time step value. The first estimate is based on the viscous stability as shown in Eq (4.8). Since the grid spacing is smaller in the y direction than in the x direction, the value for Δy will be used. The kinematic viscosity (ν) is equal to 1.33e-05 m^2/s. The second estimate utilizes Eq (4.5) and Table 4.7, where the magnitudes of λ_2 or λ_3 will yield a minimum Δt_{CFL} value. Eq (4.9) takes these results and rearranges Eq (4.4) to solve for Δts. For both estimates, the constant C was arbitrarily chosen to be 0.5, which is a typical value for this variable. By plugging in the known values

for each equation and taking the smaller of them to determine the limiting factor, it was discovered that the time step should be 4e-08 seconds, calculated from Eq (4.9).

$$\text{time step} = \Delta ts = \frac{\Delta y^2}{\nu} * 0.5 = \text{3e-05 sec} \tag{4.8}$$

$$\text{time step} = \Delta ts = \frac{\Delta y}{a} * 0.5 = \text{4e-08 sec} \tag{4.9}$$

The final feature of the Time Dependent Information to be input is the Save Increment. This instructs GASP to save the solution and grid at a specified, constant increment from $t = 0$ until the maximum time. The value selected was 0.0001 seconds, meaning that the program produces a solution at $t = 0$ sec, 0.0001 sec, 0.0002 sec, 0.0003 sec, etc. For the Convergence Information, the Write Restart Every input box is used to save data to a file after a specified number of cycles (chosen to be 1000) has passed. The value entered here will not effect the calculated results, but it is used as a measure to prevent the loss of data in the event that the program is terminated early for any reason [6]. Table 4.8 summarizes all of the selections made in the Run Definitions tab.

Table 4.8: Selections from the Run Definitions Tab.

Info Section	Item	Value Chosen
Temporal	Accuracy	2nd Order
	Algorithm	Explicit Runge Kutta
Solver	Run Type	Runge Kutta
	Solver Type	Flow
Time Dependent	Max # of Steps	use Eq (4.3)
	Time Step	4e-08 sec
	Max Time	(user defined) sec
	Save Increment	0.0001 sec
Convergence	Write Restart Every	1000

Post Processing Tab

GASP allows the user to either export data to a file at each time step while the program is running, or the user can wait until the program has finished solving the problem and then select the data to export to a file at a specific instant of time. The former option

(Option 1) was used to imitate the data that would be seen by the pressure transducers, in the experimental setup. All of the information needed for this (such as variables to be exported and the file name to save the data to) must be established in the Post Processing tab before GASP begins its calculations. The latter option (Option 2) was used to export the properties of the flow at specific times to see the interactions with the walls, the boundary layer formation, and compare the results to the theoretical predictions. Unlike the first option, this one does not require initial preparation and all settings can be applied once GASP has finished running.

The iterations performed to find the solution are performed outside the GUI, in the terminal window. The solve command (gasp –solve -i geogrid.xml, where geogrid is the name of the xml file where all of the conditions to solve the problem are stored) begins this process. Once completed, GASP can once again be launched and the results found in the Post Processing tab. In the tree view, two copies of the *Zones* folder are inserted under the *All Output* folder. One folder will contain the Post Processing settings for Option 1 (and will only have Zone 2 inside, the reason for which will be explained shortly), and the other folder will hold the Option 2 settings (and contains both Zone 1 and Zone 2). In order to activate the Post Processing tab, one of these folders must be highlighted (selected).

Grid Range

The Grid Range sub-tab is used to describe the type of range, where to interpolate the grid to, and the type of points to include in the output. Between Option 1 and Option 2, the Range Type is the only setting that differs. Option 1 uses a point range, whereas Option 2 uses the volume range. For the point range, the x coordinate, corresponding to the transducer location on the shock tube, needs to be entered into the I Range input box. This coordinate is measured from the diaphragm location at $x = 0$ m (where Zone 2 begins), as has been previously established. The points that were used for each grid (coarse or fine) and transducer, are listed in Table 4.9. As shown, the amount of error found was less than 1%, so it was concluded that these points would be good selections because they almost perfectly match the locations on the experimental shock tube. The J Range and K Range are measured at their maximum values, which imitates a location on the tube wall.

The point range option can only be used for one zone because it can only extract data from one location per folder.

Table 4.9: Point selected corresponding to the transducer location for Option 1.

Transducer #	Shock Tube Location (x coordinate)	Grid Type	GASP Location (x coordinate)	Point (I Range value)	% Error
1	1.483 m	Coarse	1.479 m	149	0.24%
(*i.e.* B)		Fine	1.484 m	298	0.09%
2	2.030 m	Coarse	2.029 m	204	0.08%
(*i.e.* C)		Fine	2.029 m	407	0.08%

Option 2 uses the volume range to create output files which contain the solutions for Zone 1 and Zone 2. Instead of just using one point on the tube wall, the volume range uses all of the points, from the minimum (the centerline) to the maximum (the tube wall), and does this for the entire length of the tube (*i.e.* all points in the I Range, J Range, and K Range are utilized).

The Cell Centers interpolation type was used for both options. This interpolation type was chosen because the solution variables (such as pressure, density, and velocity) that GASP calculates are stored at the cell centers. If a different interpolation type was chosen (such as Nodes), then the solution would need to be interpolated out to the nodes, and thereby possibly introduce some error into the results. This is a good choice, especially for Option 1, because it gives the most accurate results for the discrete flow quantities (such as pressure, temperature, and Mach number) [6]. The cell center is defined by GASP as the center of a control volume enclosed by 8 grid points. For the X-Axis Axi-Symmetric boundary, the only boundary that has split flux, the value at the cell center on the boundary face is averaged. However, for all other boundaries (which all have full flux), the actual boundary value is used [6].

The Display Cell Types section is used to control the display of grid points on the screen, within GASP, and define the manner in which to output the data for analysis with another program, such as Tecplot [6]. The default options of Discrete Cells, Interp Cells, and Proj Cells were chosen by default. No other boxes were toggled because there were no

holes in the grid to define.

Solution

The Solution sub-tab is used to select the properties that the user wishes to export, and describes how to depict the data on screen within the program. The Available Variables Filtered By section is split up into categories which contain the variables that the user can pick from. Option 1 used time from the Miscellaneous Variables section and pressure from the Fundamental Variables section. Option 2 used the X and Y coordinates from the Geometric Variables, and density, pressure, temperature, and u velocity from the Fundamental Variables section. The time feature used with Option 1 outputs the current time, which is why it was utilized for analysis while GASP was running. The Geometric Variables gives the x and y coordinates for both zones and depends only on its geometry. The density output is the mixture density, determined by taking the sum of all of the component densities. The pressure calculated is the static pressure, and the temperature is the static translational temperature. Finally, the u velocity is the velocity in the x direction [6]. In order to use these variables, they must be placed in the Active Variables list, accomplished by selecting the variable and pressing the Add button. Table 4.10 summarizes, for each option, the variables used and the category from which they originated.

Table 4.10: List of the variables to be exported for analysis.

Option	Category	Variables
1	Miscellaneous Variables	Time
	Fundamental Variables	Pressure
2	Geometric Variables	X Coordinate
		Y Coordinate
	Fundamental Variables	Density
		Pressure
		Temperature
		U Velocity

Export

The purpose of the Export sub-tab is to take the information from the previous sub-tabs (Grid Range and Solution) and export it to a file. Option 1 outputs the file in ASCII

Line Output format, whereas Option 2 uses Tecplot format. In the ASCII format, the first two lines list the variables and its corresponding units as column headers, and each line that follows represents a point on the grid. Since Option 1 is recording the data to the file during the run, the Append to File box must be toggled. Also, the Output From Solver should have the During Run (time steps) option selected along with Every 200 Time Steps. (Note that 200 was an arbitrary number selected that proved to export a significant number of data points for analysis without slowing down the solving process.) These three selections, in combination, instruct GASP to record the data once every 200 time steps during the run and add it to the file after the previous entry. Option 2 uses the Tecplot option to export the data. This will create a file in ASCII format (rather than Binary), and adds the necessary Tecplot formatting at the top of the file. The None option from the Output From Solver section is selected so no data is exported during the run. When GASP has finished the computations and the variables to export for a desired time (chosen under the Time Levels box under the tree view) are selected, the file is created by pressing the Output button under the Output From GUI section.

Chapter 5

Results

5.1 Experimental Results

The shock tube experiment was performed ten times under very similar conditions to determine the uncertainty in the measurements. As previously mentioned, the driver section was pressurized with 8 psig or 22.69 psia of air, and the driven section remained at atmospheric conditions (14.69 psia), represented as p_4 and p_1, respectively. Table 5.1 lists the initial conditions for each test (since not every test had the exact driver pressure) as well as the corresponding non-dimensionalized pressure ratios.

Table 5.1: Initial conditions for each test run.

Test	1	2	3	4	5	6	7	8	9	10
p_4 (psia)	22.67	22.39	22.44	22.59	22.68	22.47	22.68	22.76	22.57	22.67
p_1 (psia)	14.69	14.69	14.69	14.69	14.69	14.69	14.69	14.69	14.69	14.69
p_4/p_1	1.54	1.52	1.53	1.54	1.54	1.53	1.54	1.55	1.54	1.54

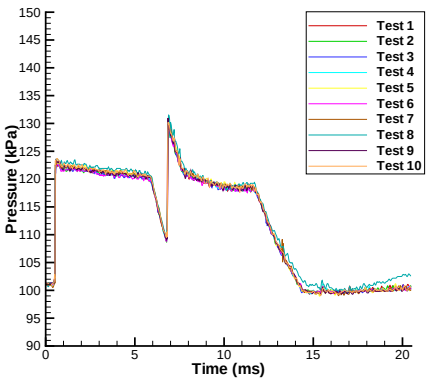

Figure 5.1: Experimental test data from Channel 1 (*i.e.* transducer B).

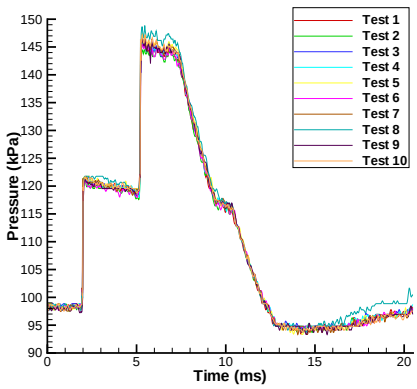

Figure 5.2: Experimental test data from Channel 2 (*i.e.* transducer C).

The voltage traces from the pressure transducers are easily changed to pressure by applying Eq (4.1). The resulting pressure versus time graphs for each transducer are displayed in Figures 5.1 and 5.2. Note that Channel 1 refers to transducer B and Channel 2 refers to transducer C. For the first pressure transducer (Figure 5.1), the pressure at the starting point of the graph (very close to $t = 0$ seconds) is the experimental value of the pressure in the driven section (p_1). After a very short time, the pressure rises rapidly (in an approximate vertical jump) due to the shock wave passing by this transducer. The higher pressure is the experimental value of p_2 and should, ideally, remain at that pressure for some time. However, due to the boundary layer effects and possibly the short duration of time that the pressure transducers are able to hold their charge for before "bleeding out" from extended use, the pressure was found to decrease slightly in this region. All in all, the pressure here only drops by about 2068 N/m^2 (or 0.3 psi), which is not a significant amount to be concerned over. After approximately 5 ms has passed, the pressure makes a significant drop followed by a large rise. The pressure decrease is due to the reflected expansion wave reaching the pressure transducer, whereas the increase is from the reflected shock wave arriving at the same transducer. Everything else from this point on in the graph are due to the interactions of the reflected waves with each other or the endwalls.

Figure 5.2, which shows the pressure traces from the second transducer, also begins at p_1 and rises up to p_2 due to the propagating shock wave. At approximately 5 ms (or a short time before), the pressure rises once again to a pressure of p_5 due to the reflected shock wave reaching the transducer. As for the first transducer, everything that occurs after this point is due to the wave interactions. Table 5.2 summarizes the pressures that were read from the graphs and the resulting pressure ratios. Since there was fluctuation in the pressure traces (meaning that the lines were not as straight as proposed by the theory), the values are only an approximate estimate.

From Figures 5.1 and 5.2 and Table 5.2, it can be seen that the ten tests performed for each channel yielded similar results. This proves that for similar initial conditions, the experiment is repeatable. As a result, for every time recorded, the pressure values of each test were averaged together, and are displayed in Figure 5.3. From this graph, the two time differences previously discussed and labeled in the figure (Δt_1 and Δt_2), can be determined.

As a reminder, Δt_1 refers to the time it takes the shock wave to travel from the first to the second pressure transducer. As indicated on the graph, this value is found by taking the difference in times between when the rise occurs for the first transducer and when it occurs for the second. The time it takes the shock wave to pass the second transducer, reach the endwall, and reflect back to the same transducer is referred to at Δt_2. Hence, it is found by taking the time difference between the first and second rise of transducer 2. The averaged-data graph is used here for simplicity, but the time differences can be found for each test (with an accuracy of about 0.02 ms) and are listed in Table 5.3. The values of Δt_1 found for each test can then be used to calculate the speed of the shock wave (c_s) since the distance between the two transducers (x_{BC}) is known, *i.e.* $c_s = x_{BC}/\Delta t_1$, where $x_{BC} = 0.548$ m. These results are also listed in Table 5.3.

Table 5.2: Experimental results from Channels (Ch.) 1 and 2.

Test	Ch.	p_1 (N/m^2)	p_2 (N/m^2)	p_5 (N/m^2)	p_2/p_1	p_5/p_2
1	1	101146	122313	N/A	1.21	N/A
	2	98250	120727	144997	1.23	1.20
2	1	101284	122313	N/A	1.21	N/A
	2	98181	119900	143963	1.22	1.20
3	1	101146	122313	N/A	1.21	N/A
	2	98526	121072	145204	1.23	1.20
4	1	101146	122451	N/A	1.21	N/A
	2	98181	120934	145410	1.23	1.20
5	1	101146	122796	N/A	1.21	N/A
	2	98043	121210	146789	1.24	1.21
6	1	101146	122175	N/A	1.21	N/A
	2	98181	120038	144859	1.22	1.21
7	1	100939	122658	N/A	1.22	N/A
	2	97906	120865	145686	1.23	1.21
8	1	101008	123002	N/A	1.22	N/A
	2	98250	121486	148168	1.24	1.22
9	1	101146	122520	N/A	1.21	N/A
	2	97906	120520	145548	1.23	1.21
10	1	101008	122865	N/A	1.22	N/A
	2	98250	121279	146376	1.23	1.21

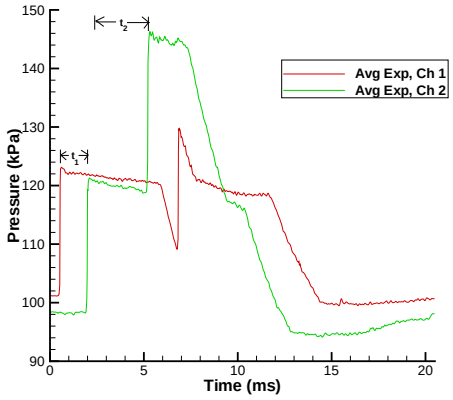

Figure 5.3: Averaged test results from both pressure transducers.

Table 5.3: Experimental results from Channels 1 and 2.

Item	1	2	3	4	5
Δt_1 (ms)	1.44	1.46	1.45	1.46	1.46
Δt_2 (ms)	3.23	3.23	3.23	3.22	3.22
c_s (m/s)	379.55	375.64	376.94	375.39	376.16
Item	6	7	8	9	10
Δt_1 (ms)	1.46	1.45	1.45	1.46	1.46
Δt_2 (ms)	3.23	3.23	3.23	3.22	3.22
c_s (m/s)	376.16	378.24	377.98	375.13	375.13

5.2 Theoretical Results

By using the equations from Chapter 3, the theoretical values that result from the initial conditions of the experiment can be calculated. From the dimensionless ratios and known quantities, the values of pressure, temperature, and density for regions 2, 3, and 5 can also be determined. The results are listed in Tables 5.4, 5.5, 5.6, 5.7, 5.8, and 5.9 for the pressure, velocity, temperature and density, Mach number, time, and reflection, respectively.

The average data for each of the ten tests and the given shock tube dimensions were used to create a graph (Figure 5.4) for both pressure transducers to display what, theoretically, should happen during a test. As described in the previous section, the pressure begins at p_1. The time it takes the shock wave to travel from the diaphragm to the first transducer

Table 5.4: Theoretical Results, Pressure

Test	p_2/p_1	p_3/p_4	p_5/p_2	(N/m^2) $p_2 = p_3$	(N/m^2) p_5
1	1.24	0.80	1.23	125392	154257
2	1.23	0.81	1.22	124640	152465
3	1.23	0.81	1.22	124775	152785
4	1.24	0.80	1.23	125178	153746
5	1.24	0.80	1.23	125419	154321
6	1.23	0.81	1.23	124855	152977
7	1.24	0.80	1.23	125419	154321
8	1.24	0.80	1.23	125633	154833
9	1.24	0.80	1.23	125124	153618
10	1.24	0.80	1.23	125392	154257

Table 5.5: Theoretical Results, Velocity (in m/s)

Test	$u_2 = u_3$	c_s	c_l	c_r	c_c
1	52.89	374.56	-341.35	-277.88	52.89
2	51.38	373.57	-341.35	-279.70	51.38
3	51.65	373.57	-341.35	-279.38	51.65
4	52.46	374.28	-341.35	-278.40	52.46
5	52.95	374.60	-341.35	-277.82	52.95
6	51.81	373.85	-341.35	-279.18	51.81
7	52.95	374.60	-341.35	-277.82	52.95
8	53.37	374.88	-341.35	-277.30	53.37
9	52.35	374.21	-341.35	-278.53	52.35
10	52.89	374.56	-341.35	-277.88	52.89

was calculated by using the speed of the shock wave and the distance on the shock tube between these two points ($t = x_B/c_s$, where $x_B = 1.482$ m). When the shock wave reaches this location, it causes the pressure to rise to p_2. It should remain at this pressure until another wave (either the reflected shock wave or the reflected expansion wave) passes by the transducer. The final time used was the time that the reflected shock wave would reach the same transducer. As mentioned in the theoretical computions section, this is composed of the time it takes to reach the endwall (calculated by using c_s) and the time for the reflected wave to reach the transducer (calculated by using W_r). The second transducer was calculated in a similar fashion for the first three points (the p_1 and the p_2 regions), but

Table 5.6: Theoretical Results, Temperature and Density

Test	T_3/T_4	T_2/T_1	T_3/T_2	(K) T_3	(K) T_2	ρ_3/ρ_2	(kg/m^3) ρ_3	(kg/m^3) ρ_2
1	0.94	1.06	0.88	272.30	308.33	1.13	1.60	1.42
2	0.94	1.06	0.89	272.80	307.79	1.13	1.59	1.41
3	0.94	1.06	0.89	272.71	307.89	1.13	1.59	1.41
4	0.94	1.06	0.88	272.45	308.18	1.13	1.60	1.42
5	0.94	1.06	0.88	272.29	308.35	1.13	1.60	1.42
6	0.94	1.06	0.89	272.66	307.95	1.13	1.60	1.41
7	0.94	1.06	0.88	272.29	308.35	1.13	1.60	1.42
8	0.94	1.06	0.88	272.15	308.50	1.13	1.61	1.42
9	0.94	1.06	0.88	272.48	308.14	1.13	1.60	1.41
10	0.94	1.06	0.88	272.30	308.33	1.13	1.60	1.42

Table 5.7: Theoretical Results, Mach Number

Test	$M_s = M_1$	M_2	M_3
1	1.10	0.15	0.16
2	1.09	0.15	0.16
3	1.09	0.15	0.16
4	1.10	0.15	0.16
5	1.10	0.15	0.16
6	1.10	0.15	0.16
7	1.10	0.15	0.16
8	1.10	0.15	0.16
9	1.10	0.15	0.16
10	1.10	0.15	0.16

Table 5.8: Theoretical Results, Time (in ms)

Test	Δt_1	Δt_2
1	1.46	3.45
2	1.47	3.45
3	1.47	3.45
4	1.46	3.45
5	1.46	3.45
6	1.47	3.45
7	1.46	3.45
8	1.46	3.45
9	1.46	3.45
10	1.46	3.45

using a different distance (from the diaphragm to the second transducer, $x_C = 2.030$ m). The next jump to p_5 occurs when the reflected shock wave returns to this location. As with the final time computed for the first transducer, the time when p_5 is seen is a sum of the time to reach the endwall and the time to once again reach the transducer. The final point in the graph was arbitrarily chosen to be the same time as that used for the first transducer. It should be noted that this figure is a simplified version of the pressure changes seen in a shock tube, and therefore does not include the interactions of the reflected expansion waves.

Table 5.9: Theoretical Results, Reflection

Test	M_r	(m/s) $-W_r$	p_5/p_2	(N/m^2) p_5	(K) T_5	(kg/m^3) ρ_5
1	1.09	332.25	1.22	154257	327.22	1.64
2	1.09	332.80	1.21	152465	326.15	1.63
3	1.09	332.70	1.21	152785	326.35	1.63
4	1.09	332.40	1.22	153746	326.91	1.64
5	1.09	332.23	1.22	154321	327.25	1.64
6	1.09	332.64	1.21	152977	326.46	1.63
7	1.09	332.23	1.22	154321	327.25	1.64
8	1.10	332.07	1.22	154833	327.55	1.65
9	1.09	332.44	1.22	153618	326.84	1.64
10	1.09	332.25	1.22	154257	327.22	1.64

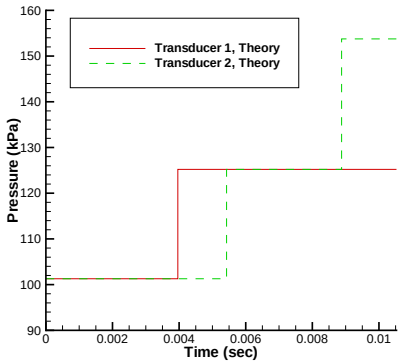

Figure 5.4: Theoretical graph of the pressure traces from both transducers, not including the reflected expansion.

5.3 Matlab Results

The purpose of the Matlab program was to create an output that was independent of time. This was accomplished by non-dimensionalizing the data output in the manner listed in Table 5.10. Most of these properties are non-dimensionalized by the initial driven conditions. For the distance, the initial speed of sound was used along with the time. Since the expansion wave is composed of multiple waves (varying in speeds from c_l to c_r), each one will interact with the wall and/or other expansion waves causing the governing equations to become very complicated and difficult to solve. For these reasons, the resulting graphs

are valid for any time before the expansion wave reaches the driver endwall, which occurs before the shock wave reaches the driven endwall.

Table 5.10: How the properties were non-dimensionalized.

Property	Description	Non-Dimensional Property
x	distance along the x-axis	$x/(a_1 t)$
p	pressure	p/p_1
ρ	density	ρ/ρ_1
T	temperature	T/T_1
u	velocity	u/a_1

In order to test the validity that the graphs can be used for any time (since the code requires an arbitrary time input), the program was run at $t = 0.00147$ seconds and at $t = 0.00293$ seconds. The first time corresponds to when the expansion is approximately half way down the driver section and the second time is approximately when the expansion reaches the endwall. The resulting graphs for the pressure, density, temperature, and velocity for these times are displayed in Figures 5.5 - 5.12. These figures can be seen as snap-shots of everything that is occurring in the shock tube at a given instant of time. To recall, the Matlab code was broken up into five regions and appear from left to right on the graphs in the following order: in the driver section, in the expansion wave, between the expansion wave and contact surface, between the contact surface and shock wave, and in the driven section. In Figures 5.5 and 5.6, the non-dimensionalized pressure begins (at the left end of the graph) with the initial condition in the driver section, for the area in front of the expansion fan. As the expansion wave propagates into the driver section, it decreases the pressure. The pressure remains constant for the regions between the expansion wave and contact surface and between the contact surface and shock wave because the pressure does not change across the contact surface. Finally, on the other side of the shock wave, the pressure drops down to the initial pressure in the driven section because the shock wave has not yet reached the endwall. The density, as with the pressure, begins at the initial conditions in the driver section as shown in Figures 5.7 and 5.8. Similarly, as the expansion wave travels down the driver, it lowers the density because the gas is no longer confined in such a small volume. The density is constant from the other side of the expansion wave

up to the contact surface. Across the contact surface, the density, unlike the pressure, does not remain the same. The other side of the contact surface up to the shock wave has a lower density than the previous side (expansion wave to contact surface). However, this density is higher than the initial density in the driven section, which is on the other side of the shock wave (represented by the vertical line connecting the last two plateaus). For the temperature graphs, Figures 5.9 and 5.10, the initial conditions in both driver and driven sections are the same. Due to the ideal gas law ($p = \rho RT$), the remaining three regions in between are dependent on how the pressure and density change. In the expansion region, since the pressure decreases, the temperature must also decrease because the flow here is isentropic, Eq (5.1). The temperature remains constant until it reaches the contact surface. In this region (the other side of the contact surface up to the shock wave), the pressure does not change, but the density is lowered to a new constant value. As a result, the temperature must increase (and remain at this new value) to satisfy the ideal gas law. Finally, on the other side of the shock wave, the temperature returns to the initial condition. Figures 5.11 and 5.12 show that the initial velocity in both sections begin at 0 m/s, since there is no initial flow in the shock tube. The expansion wave gradually increases the velocity to a higher value. It will remain at this value across the contact surface and up to the shock wave. The other side of the shock wave returns the value to 0 m/s (as previously mentioned) because the air there has not been disturbed by any waves.

$$\frac{p_3}{p_4} = \left(\frac{T_3}{T_4}\right)^{\frac{\gamma}{\gamma-1}} \tag{5.1}$$

For each property, the graphs at $t = 0.00147$ seconds and at $t = 0.00293$ seconds show similar values for each of the five regions. The major difference between them is the length of the undisturbed driver and driven regions, which display the initial conditions. For the earlier time ($t = 0.00147$ sec), these regions were longer along the x-axis, whereas the later time had shorter regions. If these two times are plotted together on the same graph using the non-dimensionalization by $a_1 t$, it can be shown that both of the regions lie on top of each other, as displayed in Figures 5.13 - 5.16. This confirms that the graphs are valid for any time input into the program which is less than or equal to 0.00293 seconds. In more

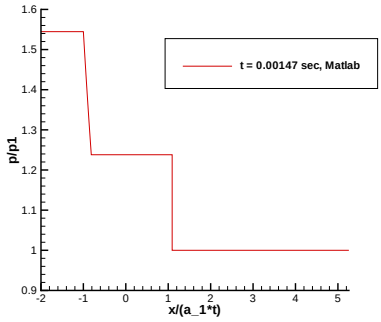

Figure 5.5: Matlab results of non-dimensionalized pressure at $t = 0.00147$ sec.

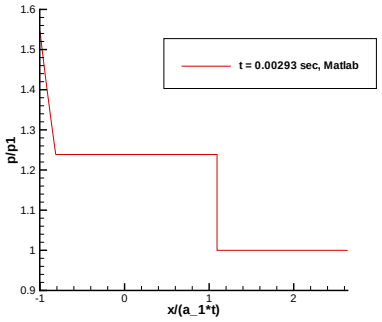

Figure 5.6: Matlab results of non-dimensionalized pressure at $t = 0.00293$ sec.

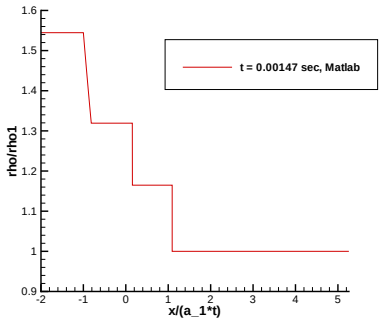

Figure 5.7: Matlab results of non-dimensionalized density at $t = 0.00147$ sec.

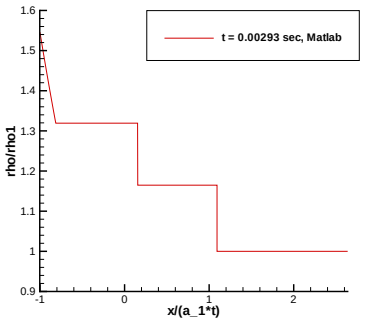

Figure 5.8: Matlab results of non-dimensionalized density at $t = 0.00293$ sec.

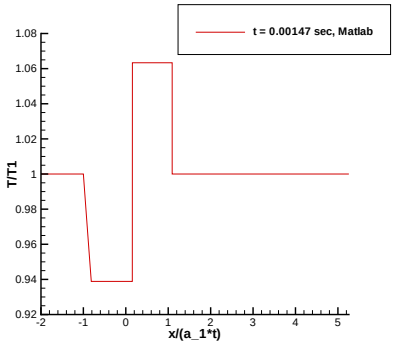

Figure 5.9: Matlab results of non-dimensionalized temperature at $t = 0.00147$ sec.

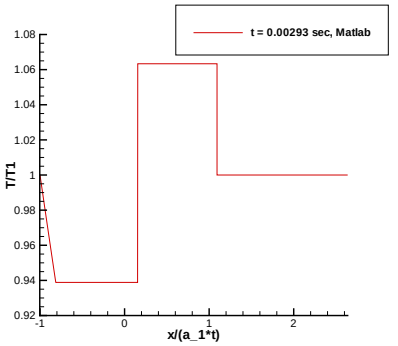

Figure 5.10: Matlab results of non-dimensionalized temperature at $t = 0.00293$ sec.

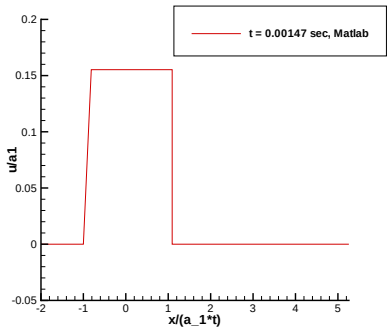

Figure 5.11: Matlab results of non-dimensionalized velocity at $t = 0.00147$ sec.

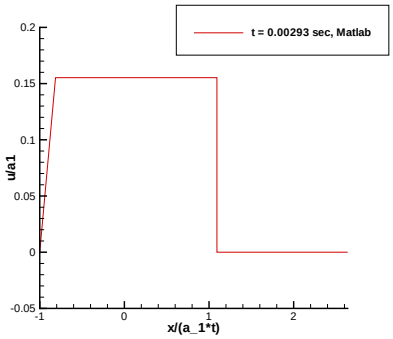

Figure 5.12: Matlab results of non-dimensionalized velocity at $t = 0.00293$ sec.

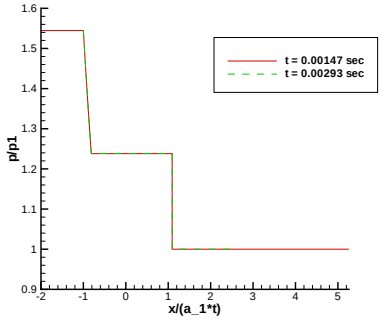

Figure 5.13: Comparison of the non-dimensionalized pressure at $t = 0.00147$ sec and $t = 0.00293$ sec.

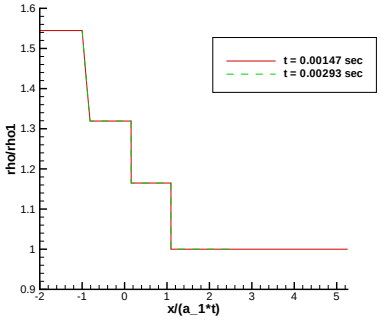

Figure 5.14: Comparison of the non-dimensionalized density at $t = 0.00147$ sec and $t = 0.00293$ sec.

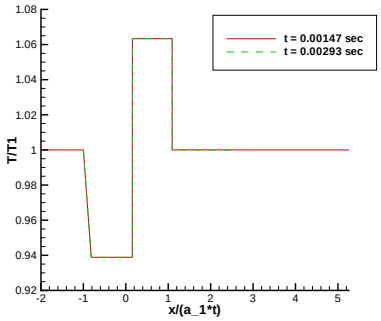

Figure 5.15: Comparison of the non-dimensionalized temperature at $t = 0.00147$ sec and $t = 0.00293$ sec.

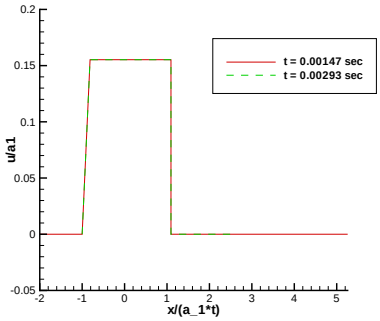

Figure 5.16: Comparison of the non-dimensionalized velocity at $t = 0.00147$ sec and $t = 0.00293$ sec.

general terms, the Matlab code is valid up to the time at which either the expansion or shock reaches its respective boundary.

5.4 GASP results

When GASP was run, the type of grid and the type of flow needed to be selected. The grid type began as geometrically stretched normal to the wall and then progressed to uniform spacing to better incorporate the boundary layer (to be discussed shortly). The geometrically spaced grid type can either be selected to be coarse or fine, where the fine setting has twice as many grid points. The advantage of choosing the fine option is that the solution is more accurate and can see changes sooner. However, since there are more points, the computation takes longer than the coarse grid. For the flow type, an inviscid or viscous flow can be implemented. The inviscid flow was the original assumption so that the theoretical shock tube equations would be valid to use. The viscous case uses laminar flow and takes into consideration the interaction with the walls and the formation of the boundary layer. By using a combination of grid and flow types, the viscous and inviscid flows can be compared to see if the inviscid shock tube assumption is valid, and if this is influenced by the grid spacing to determine whether a longer computation time is necessary.

5.4.1 Evenly Spaced vs. Geometrically Spaced Grid

The first type of grid that was created in GASP was evenly spaced along the x-axis and y-axis for each zone (driver and driven). The purpose of this was to check if the correct settings were used for the inviscid case. The plots of the resulting graphs of the pressure (Figure 5.17), density (Figure 5.18), temperature (Figure 5.19), velocity in the x-direction (Figure 5.20), and the pressure traces (Figures 5.21 and 5.22) had the same trends as what was to be expected, and therefore it was concluded that the selections were correct.

Since the purpose of the experiment is to analyze the boundary layer effects, the grid spacing must be small enough to to see what is occurring within it. The boundary layer thickness (BL) in the driven section is estimated by using Eq (5.2). Here, the dynamic viscosity (μ) at T_2 (about 35 degrees Celsius) was found in a table to be 1.89e-5 $kg/m \cdot s$,

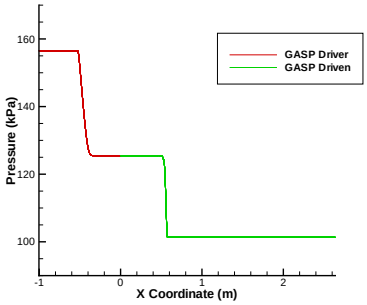

Figure 5.17: Pressure along the shock tube at $t = 0.00147$ seconds for the uniformly spaced grid.

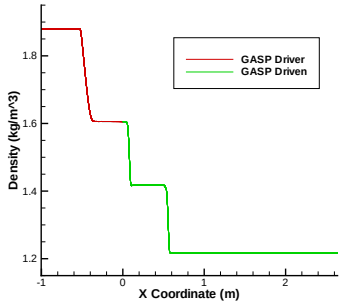

Figure 5.18: Density along the shock tube at $t = 0.00147$ seconds for the uniformly spaced grid.

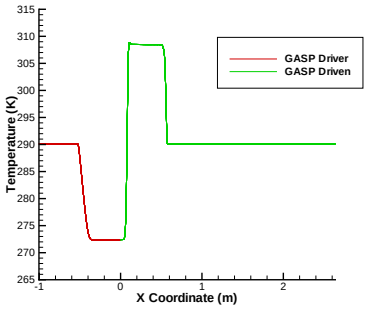

Figure 5.19: Temperature along the shock tube at $t = 0.00147$ seconds for the uniformly spaced grid.

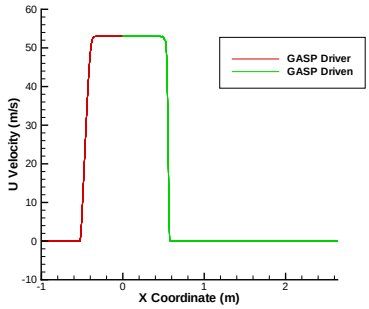

Figure 5.20: Velocity along the shock tube at $t = 0.00147$ seconds for the uniformly spaced grid.

and therefore, the kinematic viscosity (ν) is equal to 1.33e-5 m^2/s and the boundary layer (BL) is approximately 0.31 mm.

$$BL \sim \sqrt{\nu t} \;=\; \sqrt{\nu \frac{L_{driven}}{c_s}} \text{ , where } \nu = \frac{\mu(T_2)}{\rho_2} \tag{5.2}$$

The y-spacing for each zone in the uniform grid was only 2.6 mm, and would therefore be insufficient. As a result, a partially geometric and partially uniformly spaced grid was created to compensate for this difference. This grid begins as a geometrically spaced grid at the shock tube wall where it is only 0.029 mm thick. As the y value decreases to the centerline (where $y = 0$), the cells become a little larger. At an arbitrary y location (calculated by a Matlab code to be the 40th point out of 75 points), the spacing switches such that the last geometric spacing is the thickness of the uniform spacing, which is equal

to approximately 0.674 mm. This is useful because the grid is small enough to achieve approximately ten points in the boundary layer and then grows to a certain thickness, which it maintains so that the points are not too spaced apart as it reaches the centerline. If the 0.029 mm spacing was used for the uniformly spaced grid, the program run time would dramatically increase because there are many more cells to be computed. Table 5.11 summarizes the grid size for the coarse and fine grids with uniform and geometric spacing in the x and y directions. As shown, the number of cells increases by a factor of four between the coarse and fine grids. This is because the coarse grid uses every other line (making each cell larger), thereby cutting the number of cells in half for both directions (x and y).

Table 5.11: Summary of the cell size for geometric and uniform spacing of the coarse (C) and fine (F) grids.

	Δx (mm)		Δy_{min} (mm)		Δy_{max} (mm)		# of Cells	
Type	C	F	C	F	C	F	C	F
Uniform	10	5	5.29	2.64	5.29	2.64	2562	9490
Geometric	10	5	0.058	0.029	1.35	0.674	13908	54750

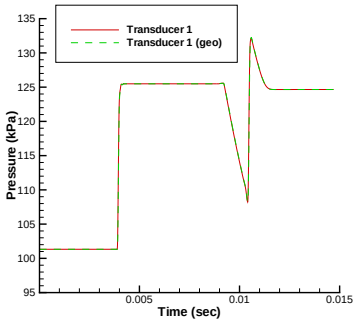

Figure 5.21: Comparison of the uniform and geometric grid spacings for transducer 1 at $t = 0.00147$ sec.

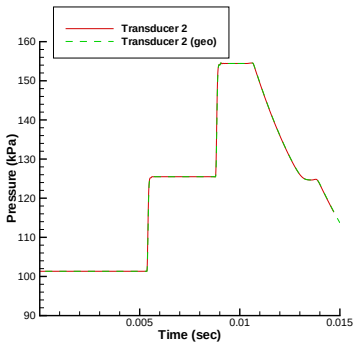

Figure 5.22: Comparison of the uniform and geometric grid spacings for transducer 2 at $t = 0.00147$ sec.

For comparison of the two grid types, the pressure traces as seen by each transducer are plotted together in Figures 5.21 and 5.22 for the inviscid case. The green line which is labeled "geo" refers to the geometrically spaced grid, and the other red line refers to the evenly space grid. As shown, at 0.00147 seconds, the two graphs lie directly on top of one

another, as expected. All in all, in order to have a small boundary layer spacing without compromising the run time, the geometric grid is preferred and will be used by GASP from this point forward for the remainder of the analysis.

5.4.2 GASP Transducer Output

GASP was programmed to mimic data that would emerge from pressure transducers by recording the pressure with respect to time at the corresponding x locations on the shock tube. The data was recorded for 0.011 seconds for each transducer under different flow conditions and grid spacings. Note that the geometric grids (coarse and fine) were used for all GASP calculations.

Coarse vs. Fine Grid

The first comparison was to determine the effect of grid spacing for a given flow type (either inviscid or viscous). Figures 5.23 and 5.24 compare the spacing for inviscid flow, whereas Figures 5.25 and 5.26 are for viscous flow. As a reminder, transducer 1 corresponds to location B on the shock tube, and transducer 2 to location C. Although not visible in the figures, upon closer inspection it was found that for the first transducer under the inviscid flow condition, the pressure began to change from p_1 (101.325 kPa) to p_2 slightly sooner (0.03 ms) and ended a little later (0.05 ms) for the coarse grid. The pressure at this plateau (p_2) was found to be about 125.50 kPa for the fine grid and 125.49 kPa for the coarse grid, which is in very good agreement. After some time, the reflected expansion wave reaches the pressure transducer, causing the pressure to drop, followed by the reflected shock wave which causes it to rise. The pressure that the wave reached as the result of the reflected expansion wave was about 0.76 kPa greater and the reflected shock was found to be about 1.03 kPa greater for the fine grid. These differences are most likely due to the fine grid having more data points which provide a more complete view of the pressure trends. This allows the pressure to begin to rise and fall in the appropriate places without leaving gaps at points of transition. For the second transducer, the inviscid results almost perfectly matched for both coarse and fine grids, differing by no more than 0.01 ms and 0.4 kPa. The pressure began at 101.325 kPa, the initial condition in the driven section of the shock

tube (p_1). When the shock wave passed this transducer, it caused the pressure to rise (virtually simultaneously for both grids) to 125.49 kPa for the fine grid and 125.40 kPa for the coarse grid. When the reflected shock wave returned to this transducer, another pressure increase to p_5 at 154.46 kPa for the fine grid and 154.34 kPa for the coarse grid. By comparing these pressures for both grids, it can be concluded that they are consistent with each other. In summary of the inviscid flow, the coarse and fine grids are in very good agreement with each other for both transducers.

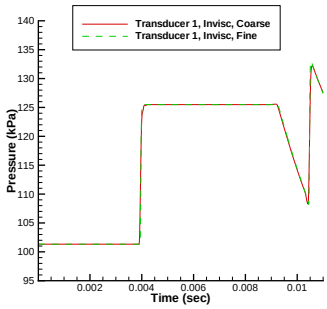

Figure 5.23: Comparison of the grid spacings for transducer 1 with inviscid flow.

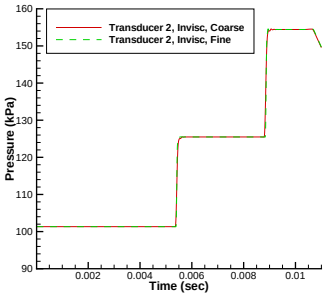

Figure 5.24: Comparison of the grid spacings for transducer 2 with inviscid flow.

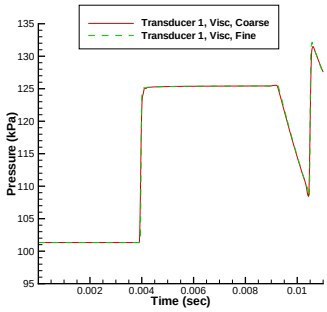

Figure 5.25: Comparison of the grid spacings for transducer 1 with viscous flow.

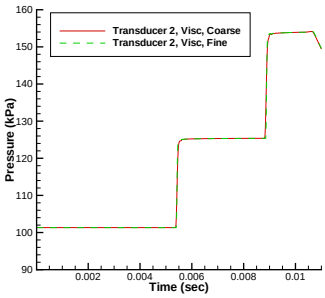

Figure 5.26: Comparison of the grid spacings for transducer 2 with viscous flow.

The viscous flow condition for the first transducer (Figure 5.25) followed the same trends as for the inviscid flow, such as the earlier start and later end of the pressure rise up to p_2. The pressure obtained at this point (p_2) was within 0.02 kPa between the two grid types (125.35 kPa for the fine and 125.33 kPa for the coarse). When the reflected expansion wave arrives at the transducer location, the minimum pressure obtained was

approximately 0.76 kPa greater for the fine grid. When the reflected shock wave passed by the transducer, it increased the pressure to a maximum which is greater than p_2 but less than p_5. By comparing the two grids in this location, the fine grid was found to be about 0.71 kPa greater than the coarse grid. The coarse and fine grid spacings for the second transducer were very similar and differed by no more than 0.05 ms and 0.20 kPa. The values obtained for p_2 and p_5 were 125.26 kPa and 153.81 kPa for the fine grid, and 124.87 kPa and 153.80 kPa for the coarse grid, respectively. The times at which these pressure changes took place were almost exactly the same for both grids. As a result, either the coarse or fine grid can be used as a good approximation for the viscous and inviscid flow as seen by the pressure transducers.

Inviscid vs. Viscous Flow

The next property to analyze is that for a given grid spacing, how do the flow types compare. Using a coarse grid for the first transducer, both flow types begin at $p_1 = 101.325$ kPa, and begin and end the pressure rise to p_2 at approximately the same time (within 0.03 ms of each other) as shown in Figure 5.27. The inviscid case remains at 125.47 kPa, while the viscous maintains a value of 125.32 kPa before the reflected expansion arrives. This difference of 0.15 kPa is small and considered to be insignificant. The minimum point that the drop in pressure due to the reflected expansion reaches, differs by about 0.39 kPa, where the viscous flow surpasses the inviscid flow. On the contrary, the maximum point attained from the reflected shock is greater for the inviscid flow by approximately 0.93 kPa. These differences could be contributed to the viscous flow taking into consideration the boundary layer effects and the interaction with the endwalls. The coarse grid of the second transducer (Figure 5.28) began at the given initial condition ($p_1 = 101.325$ kPa) and rose at almost the same time (only 0.4 ms difference, at most) to reach a p_2 value of 125.35 kPa for the inviscid flow and 125.13 kPa for the viscous flow. The next pressure increase up to p_5 also occurred a little later for the viscous flow (0.7 ms maximum difference), and resulted in 154.48 kPa and 153.81 kPa for the inviscid and viscous cases, respectively. As shown in this figure, the viscous results appear to slope upwards for the p_2 and p_5 regions, where they begin below the constant inviscid flow pressures and by the end are in more agreement (a

difference of as much as 1 kPa at the beginning and 0.40 kPa by the end). Again, this is most likely due to the interactions with the walls of the shock tube.

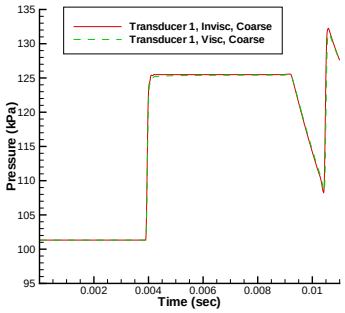

Figure 5.27: Comparison of the flow types for transducer 1 with coarse grid spacing.

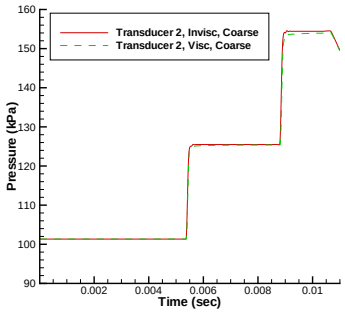

Figure 5.28: Comparison of the flow types for transducer 2 with coarse grid spacing.

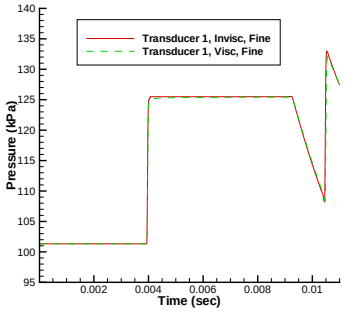

Figure 5.29: Comparison of the flow types for transducer 1 with fine grid spacing.

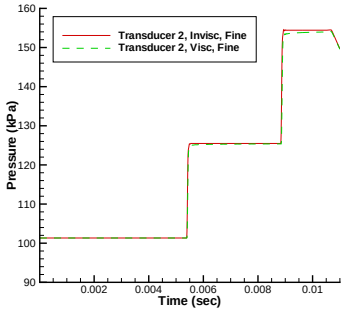

Figure 5.30: Comparison of the flow types for transducer 2 with fine grid spacing.

The fine grid for the first transducer followed similar trends to the coarse grid, as illustrated in Figure 5.29. The maximum time difference when the shock wave arrived was 0.4 ms, and p_2 was found to be approximately 125.49 kPa for the inviscid flow and 125.33 kPa for the viscous flow. Similar to the coarse grid with viscous flow of transducer 2, the viscous pressure seems to have a positive slope, where it begins 0.37 kPa below the inviscid flow and ends 0.02 kPa above it. The same reasoning for this difference is applied here- it is due to the wall interactions. Although the coarse grids for the first transducer somewhat exhibit this trend, the difference is much smaller and the viscous flow appears to continuously lie below the inviscid flow. The reflected waves cause the pressure for the

viscous case to drop about 0.57 kPa below the inviscid flow, but the inviscid pressure rise was found to be 0.65 kPa above the viscous flow (see Figure 5.30). These differences of less than 1 kPa are considered to be insignificant. The fine grids of the second transducer began at 101.325 kPa and increased to p_2 virtually simultaneously (with a maximum difference of 0.02 ms) followed by another increase in pressure to p_5 (which differed the most by 0.06 ms). The p_2 values were determined to be 125.49 kPa for the inviscid flow and 125.25 kPa for the viscous flow, and the p_5 values were 154.47 kPa and 153.83 kPa for the inviscid and viscous flows, respectively. As the last two cases have described, the viscous flow begins less than the inviscid flow but due to its positive slope, it becomes in better agreement by the end. This is more noticeable for the p_5 region (where the starting to ending difference is 0.59 kPa) than for the p_2 region (where the difference is 0.37 kPa). All in all, for the fine grids, the viscous and inviscid flows are in relative agreement, differing the most in the p_2 region for transducer 1 and in p_2 and p_5 for transducer 2. In conclusion of the transducer comparison of the coarse and fine grids with inviscid and viscous flows, if the flow type was kept constant, the grid types were in good agreement with each other. However, for a constant grid spacing, the inviscid and viscous results differed more in the p_2 and p_5 regions because the inviscid flow remained constant but the viscous flow gradually sloped upwards to a better agreement. Although these differences were not very large, if precise calculations need to be made, choosing the appropriate flow type could have an impact on the accuracy of the results.

5.4.3 GASP Properties Output

GASP is also capable of exporting the data of a chosen property (in this case pressure, density, temperature, and velocity) and direction (x, y, and/or z) at a specific time during the test (to the pre-selected 0.0001 second accuracy). This information was used to compare the grid spacings (fine or coarse) and the flow types (inviscid or viscous) at a time of 0.0035 seconds and 0.011 seconds during the experiment. At $t = 0.0035$ seconds, the expansion wave has reached the endwall and just begun to reflect back, displaying the properties in regions 1 (the initial condition in the driven tube), 2 (between the shock wave and contact surface), and 3 (between the contact surface and expansion wave). At $t = 0.011$ seconds,

the shock wave has reached the endwall and reflected past transducer 2, displaying the properties in region 5 (the reflected shock wave region). The next four sections will look at these properties along the distance of the tube (x-direction) at the aforementioned times.

Pressure

Figures 5.31 and 5.32 compare the grid spacings with constant flow types, whereas Figures 5.33 and 5.34 compare the flow types with a constant grid spacing. For the inviscid flow (Figure 5.31), the coarse and fine grid results are virtually identical, only differing at the corners where the coarse grid ends ever-so-slightly sooner than the fine grid. Also, at the driver endwall, the pressure is about 0.98 kPa lower for the fine grid most likely due to the closer proximity to the wall in comparison to the coarse grid which is slightly farther away. The pressure reaches a maximum in regions 2 and 3 ($p_2 = p_3$) of about 125.483 kPa for the coarse grid and 125.488 kPa for the fine grid. This value is maintained up to the shock wave location ($x = 1.344$ m), where on the other side of the wave, the pressure is still at the initial atmospheric condition ($p_1 = 101.325$ kPa). The viscous flow (Figure 5.32) followed a very similar trend to that of the inviscid flow. For example, the pressure began at the endwall about 1.01 kPa lower for the fine grid, the corners extended a little farther out for the fine grid, and at $x = 1.343$ m, the pressure returned to atmospheric. The pressure in regions 2 and 3 were also close, attaining values of approximately 125.442 kPa and 125.455 kPa for the coarse and fine grids, respectively. One difference in this region is that where the inviscid flow remained constant, the viscous flow had a slight decrease in pressure from start to end by as much as 0.38 kPa. This is probably due to the boundary layer formation as the waves propagate down the tube in their respective directions.

The comparison of the coarse grid spacings (Figure 5.33) began at the driver endwall where the pressure was about 0.61 kPa higher for the viscous flow. Pressures of 125.483 kPa and 125.442 kPa were reached for regions 2 and 3 for the inviscid and viscous flows, respectively. In this figure, the downwards slope of the viscous flow can be observed, especially towards the end, right before the shock wave location. After $x = 1.344$ m (on the other side of the shock wave closest to the driven endwall), the pressure has not been altered and therefore is still at its p_1 value. The fine grid spacing (Figure 5.34), also displayed

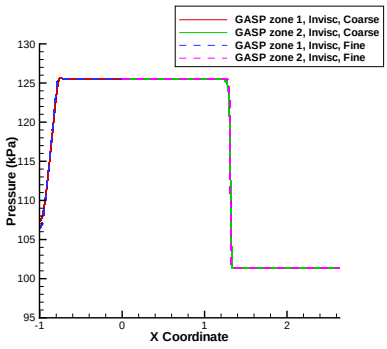

Figure 5.31: Compare p of the grid spacings with inviscid flow at $t = 0.0035$ seconds.

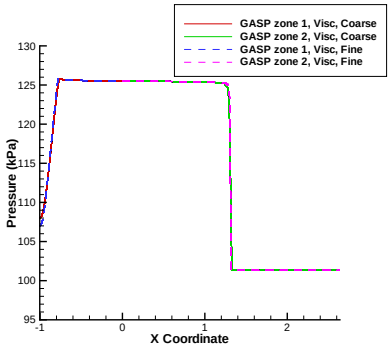

Figure 5.32: Compare p of the grid spacings with viscous flow at $t = 0.0035$ seconds.

similar trends to that of the coarse grid. First, the pressure at the driver endwall was about 0.58 kPa higher for the viscous flow. After this point, the values between the two flows almost matched up, except for the p_2 and p_3 regions, where, again, the viscous pressure was not as constant as that of the inviscid flow. Here the pressure began a little greater and ended a little less than the inviscid flow values. Finally, on the other side of the shock wave, the pressure was at atmospheric conditions. In summary, for the pressure trends at $t = 0.0035$ seconds, the fine grid provided the most information, especially at the endwalls, where the coarse grid fell about 1 kPa short. The viscous flow also provided a more accurate presentation of the flow in the shock tube by displaying the decreasing trend in regions 2 and 3, which the inviscid case did not display. Since the differences are small, a quick estimate of the shock tube values and trends can be made by using the coarse grid with inviscid flow, but ideally, the fine grid with viscous flow will yield the best results.

Figures 5.35 and 5.36 compare the pressure trends of the different grid spacings with respect to the distance along the shock tube at $t = 0.011$ seconds, whereas Figures 5.37 and 5.38 compare the flow types. All of the graphs begin at a low pressure (about 1 kPa below p_1) due to the expansion wave. The next section where the pressure quickly rises and then slopes up to a constant value is the interaction of the reflected expansion wave with the reflected shock wave. When these waves meet, they interact with each other and weaken the reflected shock. The final section is where the pressure reaches a maximum and appears to be constant. This final section will be the focus of the comparison because it represents the properties of region 5 (that of the reflected shock wave). The inviscid

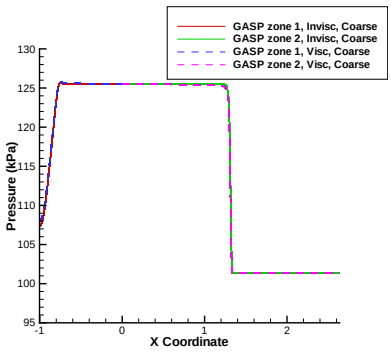

Figure 5.33: Compare p of the flow types with coarse grid spacing at $t = 0.0035$ seconds.

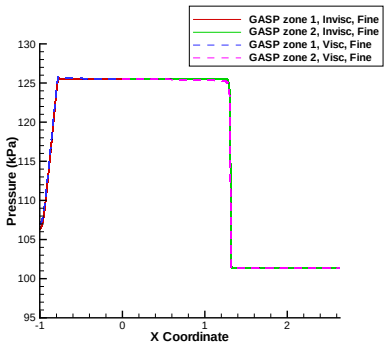

Figure 5.34: Compare p of the flow types with fine grid spacing at $t = 0.0035$ seconds.

graph (Figure 5.35) shows very similar results in all parts of the shock tube. In fact, in region 5, the pressure was found to be about 154.475 kPa and 154.437 kPa for the coarse and fine grids, respectively, and remained constant to the driven endwall. Similarly, the viscous graph (Figure 5.36) yielded similar results for the coarse and fine grid spacing. In region 5, the coarse grid reached a pressure of 154.136 kPa while the fine grid attained 154.071 kPa. Unlike the previous time ($t = 0.0035$ seconds), this value was almost constant to the endwall, differing by only 0.1 kPa. This is most likely due to its proximity to the endwall, and therefore the reflected shock wave did not travel enough distance for the boundary layer to develop enough to have an impact. Also, there is some interaction with the previous boundary layer which could have some effect on this result.

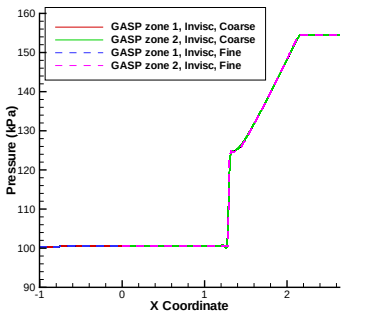

Figure 5.35: Compare p of the grid spacings with inviscid flow at $t = 0.011$ seconds.

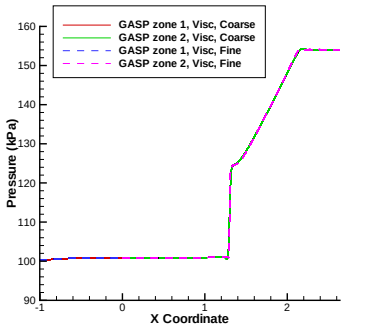

Figure 5.36: Compare p of the grid spacings with viscous flow at $t = 0.011$ seconds.

The coarse grid spacing comparison (Figure 5.37) showed slightly different results for

the inviscid and viscous flows. In the reflected expansion region, the viscous grid has an increasing slope, which ends up being about 0.63 kPa greater than its inviscid counterpart right before the vertical jump at about 1.3 m. Also, in the reflected shock region (region 5), the viscous flow results were found to be a little less than the inviscid ones (by about 0.3 kPa). The pressure in this region was found to be approximately 154.475 kPa and 154.136 kPa for the inviscid and viscous flows respectively. The comparison of the fine grid spacing (Figure 5.38) showed similar trends to that of the coarse spacing graph. Namely, the viscous pressure was slowly increasing in the reflected expansion region but the values matched slightly better (differing by only 0.39 kPa). Also, the viscous flow was found to be slightly less than the inviscid flow in region 5, where the pressures were found to be 154.437 kPa for the inviscid flow and 154.071 kPa for the viscous flow. The difference in these values is due to the viscous flow's interaction with the pre-existing boundary layer. In conclusion, at $t = 0.011$ seconds, either grid can be used for a given flow type because they yielded almost the same results. On the other hand, a specific flow type needs to be selected because the results are a little different. In conclusion of the pressure analysis at both times, the overall grid spacing results were found to be similar so a coarse grid could be used instead of the fine grid for a good estimate. As shown at the final time ($t = 0.011$ seconds), the difference is a little greater between the inviscid and viscous flows (about 0.37 kPa), so for a more accurate result, the appropriate flow type should be chosen.

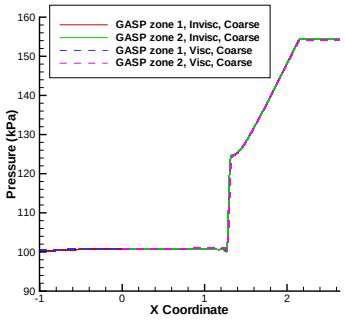

Figure 5.37: Compare p of the flow types with coarse grid spacing at $t = 0.011$ seconds.

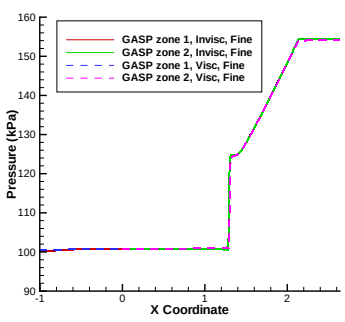

Figure 5.38: Compare p of the flow types with fine grid spacing at $t = 0.011$ seconds.

Density

The grid spacings and flow types of the density values are compared for $t = 0.0035$ seconds and $t = 0.011$ seconds in Figures 5.39 - 5.46. As shown here, the viscous results vary over a range for a given x location. This is because, unlike the pressure which is constant at a given cross-section, the density varies depending on its location with respect to the tube wall due to the effect of the boundary layer. Throughout this section, two values, representing the upper and lower bounds, will be compared to the inviscid case, which assumes that the property is constant for any y location. The line that is closest to the inviscid line is the bound representing the data at the centerline (or in the middle) of the shock tube. The innermost line (closest to the abscissa in the figures and farthest from the previously discussed line) represents the value at the shock tube wall.

At $t = 0.0035$ seconds, the reflected expansion has just begun to travel toward the driven tube. The first maximum density that is seen (at about x = -0.7 m) represents ρ_3, the density between the expansion wave and contact surface. At about $x = 0.25$ m, the density has fallen to a lower value, known as ρ_2 or the density between the contact surface and shock wave. The final drop in density is to the initial density in the driven tube under atmospheric conditions, which occurs at about $x = 1.3$ m. In Figure 5.39, the grid spacings of the inviscid flow are compared, and the values were found to be almost exactly the same. For example, in region 3, the density was calculated to be 1.60598 kg/m^3 for the coarse grid and 1.60586 kg/m^3 for the fine grid. Similarly, in region 2, the densities were 1.41787 kg/m^3 and 1.4179 kg/m^3 for the coarse and fine grid, respectively, before returning to the initial condition of $\rho_1 = 1.21741$ kg/m^3 (on the other side of the shock wave). It should also be noted that for each of these regions (1, 2, and 3), the values remained constant throughout. For the viscous flow (Figure 5.40), the data obtained at the centerline was found to be a constant value of 1.60403 kg/m^3 for the coarse grid and a constant value of 1.60388 kg/m^3 for the fine grid in region 3. At the wall, the values were found to be a little lower for the same region, in that the coarse grid had a constant density of 1.60052 kg/m^3 and the fine grid had a constant density 1.60039 kg/m^3. This implies that the density in the boundary layer is slightly less than the density in the center of the tube. Since the wall is adiabatic, the total temperature of the flow in a given region is approximately constant across the

boundary layer. Thus, the static temperature rises across the boundary layer from the center to the wall. Since the pressure is constant across the boundary layer, the density decreases in accordance with the ideal gas law. By comparing the densities at either the centerline or the wall, the values for both grids were found to be similar. In region 2, the values at the centerline were 1.41693 kg/m^3 and 1.41707 kg/m^3, and at the wall were 1.41431 kg/m^3 and 1.41439 kg/m^3 for the coarse and fine grids, respectively. Here it can also be seen that the wall values are slightly less than the centerline values. Although the grids are in good agreement with each other at the wall, they are a little different at the centerline, but still within reason. The greatest difference between the centerline and wall values occurs between these two regions, where the density at the wall decreases about 12 cm before centerline density. This is because in order to get from region 3 to region 2, the contact surface is crossed. Looking at the far end of region 2, right before the shock wave, and following the density lines back towards the contact surface, it can be seen that the wall density and centerline density grow farther apart from each other. This trend continues up to the transition from the contact surface to region 3, where the distance becomes constant. After this point, the reflected expansion causes the density values in these two locations to become very close to the same, hence the appearance of one line to the driver endwall. As previously mentioned and to summarize, by looking back from the shock wave, the boundary layer is forming behind the shock wave, which is the reason for the delay in the density change across the contact surface. Hence, although the grid spacings are similar, for the viscous grid, the location (wall or centerline) must be taken into consideration.

Figures 5.41 and 5.42 were found to follow the same trends as previously mentioned from the grid comparisons. In both of these figures, it was found that the centerline value of the viscous grid was very similar to that of the inviscid grid. For the coarse grid (Figure 5.41) in region 3, these values differed by about 0.0008 kg/m^3, which is in very good agreement. In region 2, the inviscid and viscous values were almost exact, differing by only 0.0009 kg/m^3. These differences were just about the same for the fine grid for both of these regions. For both grid types, at the wall the densities were lower than at the centerline, again, due to the boundary layer formation. In conclusion, either grid would be a good representation of

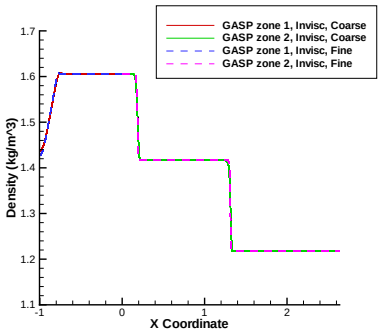

Figure 5.39: Compare ρ of the grid spacings with inviscid flow at $t = 0.0035$ seconds.

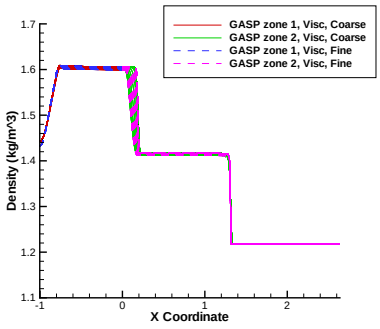

Figure 5.40: Compare ρ of the grid spacings with viscous flow at $t = 0.0035$ seconds.

density trends. The inviscid flow type only describes what is happening at the centerline and assumes that value is valid throughout. The viscous flow type, on the other hand, gives a more accurate description of what is occurring in the shock tube at a given cross-section, which can be seen by the varying density. In this sense, the viscous flow using a fine grid would give the most accurate results since the fine grid would provide more data points for a clearer transition from one density to the next for a given x location.

As with the pressure, the region of interest with the density graphs at $t = 0.011$ seconds is region 5, the reflected shock region. Here, the density is at a maximum and is coming off of the driven endwall (the right-most section of the graph). The grid spacings of the inviscid flow (Figure 5.43) show a constant value of 1.64433 kg/m^3 for the coarse grid and 1.64402 kg/m^3 for the fine grid. These values are in very good agreement with each other. Just as at $t = 0.0035$ seconds, the values for the inviscid grid are those at the centerline, and hence, there only exists one line for each spacing. In Figure 5.44, the viscous flow has a density of 1.64208 kg/m^3 and 1.64155 kg/m^3 for the centerline value, and 1.63914 kg/m^3 and 1.63869 kg/m^3 for the wall value of the coarse and fine grids, respectively. The centerline values for both grids are in good agreement with each other, as are the values at the wall. Comparing the grid spacings with one another, they are not as close as the location values, but they are still very similar to each other.

In comparing the flow types of the coarse grid (Figure 5.45), the viscous value at the centerline only differed from the inviscid flow value by 0.002 kg/m^3. The value at the

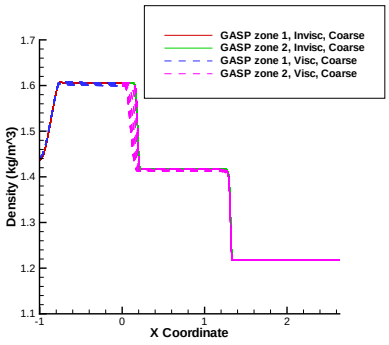

Figure 5.41: Compare ρ of the flow types with coarse grid spacing at $t = 0.0035$ seconds.

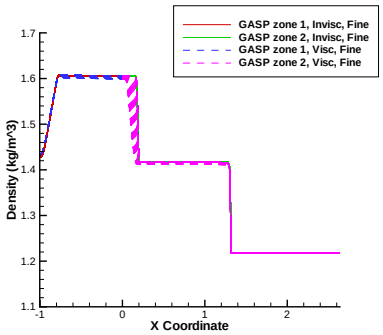

Figure 5.42: Compare ρ of the flow types with fine grid spacing at $t = 0.0035$ seconds.

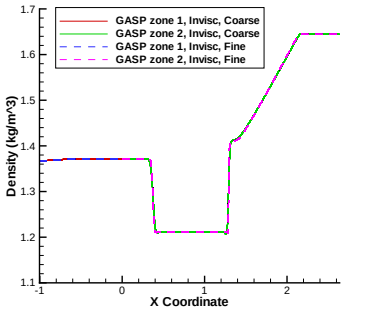

Figure 5.43: Compare ρ of the grid spacings with inviscid flow at $t = 0.011$ seconds.

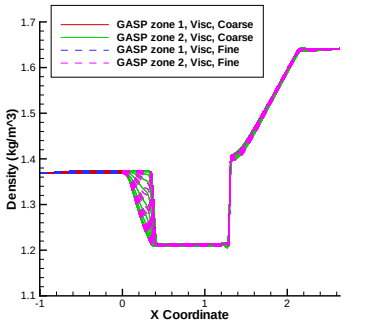

Figure 5.44: Compare ρ of the grid spacings with viscous flow at $t = 0.011$ seconds.

endwall was also not far behind and differed by only 0.005 kg/m^3. Figure 5.46, which compared the flow types of the fine grid, was found to yield the same differences in the flow types as the coarse grid had. Overall, the differences in region 5 were not as great as in regions 2 and 3 (and between these regions) because the reflected shock has not traveled a significant distance in order to develop the boundary layer enough that it would show a larger variation in density. In conclusion of the density comparisons, the grid spacing was not as significant as the flow type used. The viscous flow provides more information about the variations in density from the centerline to the endwall. If more detail about this progression is required, then the viscous flow should be coupled with the fine grid.

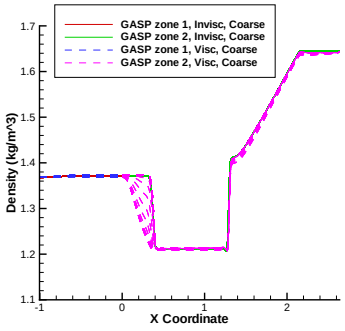

Figure 5.45: Compare ρ of the flow types with coarse grid spacing at $t = 0.011$ seconds.

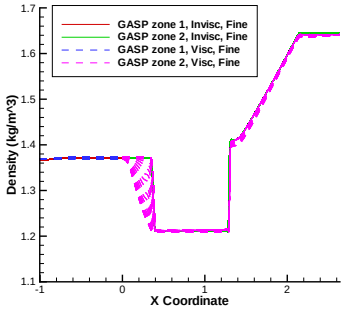

Figure 5.46: Compare ρ of the flow types with fine grid spacing at $t = 0.011$ seconds.

Temperature

The general trend for the temperature at $t = 0.0035$ seconds begins with the reflected expansion coming off the driver wall. On the other side of this wave, at about x = -0.74 m, is a constant temperature for region 3. The contact surface located around $x = 0.16$ m causes the temperature to rise to a maximum for region 2. This region ends at approximately $x = 1.2$ m, where the shock wave is located. Since the shock has not yet reached the end of the driven section, the air in front of this wave is undisturbed and hence is at 290.101 K (the atmospheric temperature). Figures 5.47 and 5.48 display these trends for a constant flow condition (inviscid for the first and viscous flow for the latter), and Figures 5.49 and 5.50 compare the flow types for a constant grid spacing (coarse for the first and fine for the second).

The coarse and fine grid spacings with inviscid flow matched very well and only differed slightly transitioning into the contact surface and into the shock wave (from left to right on Figure 5.47). The temperature in region 3 was found to be 272.413 K for the coarse grid and 272.37 K for the fine grid, which is very close. Similarly, in region 2, the temperature was 308.48 K and 308.475 K for the coarse and fine grids, respectively, which is even closer than in region 3. The values in both of these regions did not fluctuate much (on the order of 0.01 K), and therefore are assumed to be constant. The viscous flow comparison of grid spacings (Figure 5.48) is similar to what was seen in the density section. In the reflected expansion region, the temperature varies between the value at the wall and the value at

the centerline by only a little. In region 2, this value grows a little more to about 1 K. The temperature at the center of the tube was found to be 272.47 K and 272.426 K for the coarse and fine grid in region 3. At the wall, the temperature was 273.526 K for the coarse grid and 273.49 K for the fine grid. These values changed slightly in this region, namely that the centerline values decreased by about 0.1 K, whereas the wall values increased by about 0.1 K, and therefore are considered to be constant. The largest difference is at the transition from region 3 to the beginning of the contact surface. Here, from left to right on the graph, the value at the wall began to rise by as much at 12 cm before the temperature at the centerline. By the end of the contact surface, this difference was only about 0.5 cm. The temperatures found in this region (region 2) were 308.399 K and 308.399 K at the centerline and 309.47 K and 309.512 K at the wall for the coarse and fine grids, respectively. From the beginning to the end of this region, the values decreased by as much as 0.3 K, which is small enough for these values to be considered constant here. From about $x = 1.3$ m to the driven endwall, the difference in when the temperature changes is almost non-existant (where the fine grid changes at most by about 3.9 mm before the coarse grid does). Overall, the coarse and fine grids match up very well with each other for both flow types. For the viscous flow, though, the vertical position in the tube must also be taken into consideration because the grids spacings at the wall values match up, as they do at the centerline, but the wall and centerline values differ from each other by about 1 K.

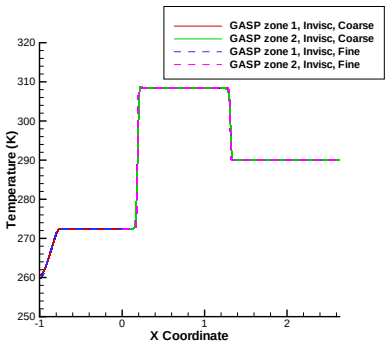

Figure 5.47: Compare T of the grid spacings with inviscid flow at $t = 0.0035$ seconds.

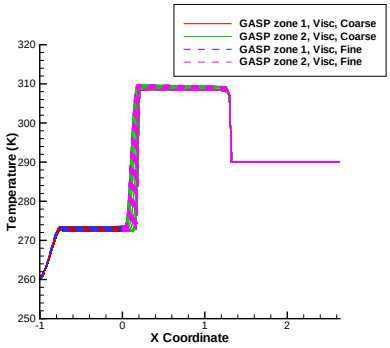

Figure 5.48: Compare T of the grid spacings with viscous flow at $t = 0.0035$ seconds.

The flow type comparisons with the coarse and fine grid (Figure 5.49 and 5.50, respectively) followed the same trend, in that the inviscid flow matched closest with the centerline value of the viscous grid. It should also be noted that the viscous temperature at the wall is greater than at the centerline, which is opposite of what was found for the density (the centerline value was greater than the value at the wall). The reason for this difference is that from the ideal gas law, the density and temperature are inversely proportional to one another for a constant pressure (which as previously seen, did not vary between the flow types). In region 3 of the coarse grid, the difference in temperature of the viscous flow at the centerline with the inviscid flow was only 0.057 K, whereas for the wall temperature, it differed by 1.113 K. In region 2, the differences were found to be 0.081 K for the centerline and 0.99 K for the wall. These results are also very consistant with that found for the fine grid (the differences with the inviscid flow being 0.056 K and 1.12 K for region 3, and 0.076 K and 1.037 K for region 2 for the centerline and wall, respectively). In summary of the temperature comparisons at $t = 0.0035$ seconds, the grid spacings were found to produce almost the same results. The inviscid flow and centerline viscous flow temperatures were also similar, but the extreme viscous value at the wall differed by about 1 K.

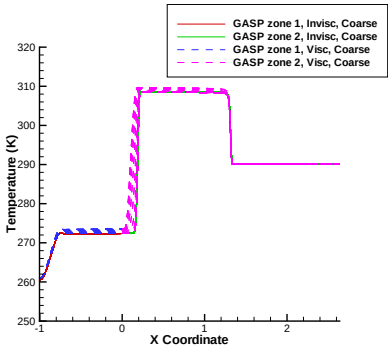

Figure 5.49: Compare T of the flow types with coarse grid spacing at $t = 0.0035$ seconds.

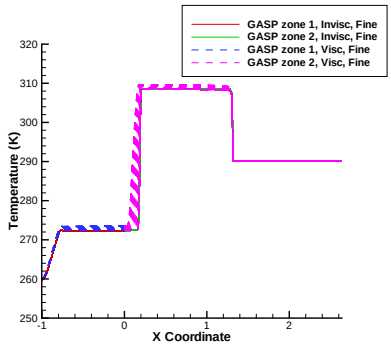

Figure 5.50: Compare T of the flow types with fine grid spacing at $t = 0.0035$ seconds.

At $t = 0.011$ seconds, as with the pressure and density, the area of interest is region 5, located where the maximum temperature lies at the right-most part of Figures 5.51 - 5.54. For the inviscid flow, the coarse and fine grids produced very similar values in this region. The coarse grid had a temperature of 327.433 K and the fine grid had 327.408 K. Throughout this region, these values changed by, at most, only 0.03 K, which is an insignificant

amount. The viscous flow (Figure 5.52) had some variation between the temperature at the center of the tube compared to the temperature at the wall. In the center, the coarse grid was at 327.149 K and the fine grid was at 327.106 K. At the wall, the temperature was a little greater than its centerline counterpart, yielding 327.743 K and 327.721 K for the coarse and fine grids, respectively. Here, the variation from the beginning to end of this region was found to be about 1.3 K, which is much greater than the center temperature variation of about 0.1 K.

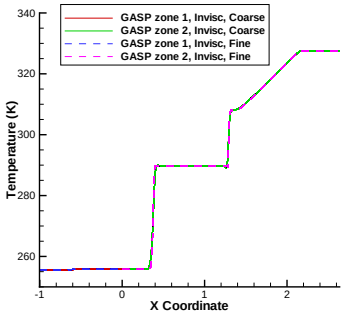

Figure 5.51: Compare T of the grid spacings with inviscid flow at $t = 0.011$ seconds.

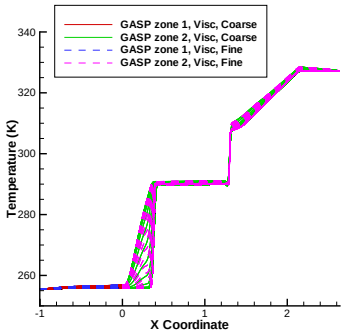

Figure 5.52: Compare T of the grid spacings with viscous flow at $t = 0.011$ seconds.

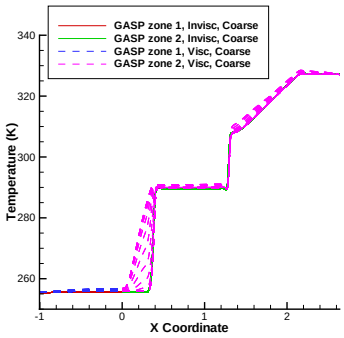

Figure 5.53: Compare T of the flow types with coarse grid spacing at $t = 0.011$ seconds.

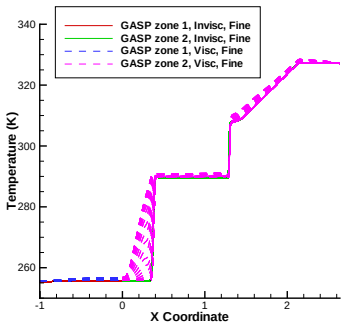

Figure 5.54: Compare T of the flow types with fine grid spacing at $t = 0.011$ seconds.

The comparison of the inviscid flow with the viscous flow for the two grid spacing are shown in Figures 5.53 and 5.54 for the coarse and fine grids, respectively. These results are a little different than that found for the density in this region. Here, the inviscid value for both grids is approximately the average of the viscous extremes at the center and wall. This

is due to the rate at which the values decrease in this region. The inviscid flow decreases by about 0.036 K, whereas the centerline viscous flow decreases by approximately 0.1 K and the wall by 1.3 K. Each of these temperature differences are an order of magnitude apart. The value that was chosen to be T_5 was the average of the temperatures at the beginning and end of the region, causing this difference. By looking at these two graphs, the viscous temperature begins with a larger difference in temperature which decreases toward the inviscid value at the end of region 5. In summary of the temperature results, both grid spacings produced similar results, but the wall temperature for viscous flow differs the most from the inviscid flow. If a detailed progression in temperature change is required, then the best combination to use is a fine grid with viscous flow.

Velocity

The comparison of velocity with respect to distance along the shock tube for a given flow type are displayed in Figures 5.55 for the inviscid flow and 5.56 for the viscous flow at $t = 0.0035$ seconds. The velocity at the driver endwall (all the way to the left in the figures) begins at 0 m/s. The reflected expansion wave causes the velocity to increase to a maximum value, where region 3 begins. This value is maintained through region 2, since the velocity does not change over the contact surface. Here, the inviscid coarse grid was found to have a velocity of approximately 52.9799 m/s, and the fine grid had a value of 52.9814 m/s. Since there was little fluctuation from the start of region 3 to the end of region 2 (only a 0.0077 m/s difference), these values were considered to be constant. The shock wave, located around $x = 1.2$ m in the driven section where the velocity drop occurs, connects the end of region 2 to the beginning of region 1. In this region, the velocity is 0 m/s because the air was initially at rest and nothing has yet disturbed it. When comparing the grid spacings for the viscous flow, it initially appeared that the coarse and fine grid results did not match up. Since GASP's computations were based upon taking the average centroid value and location of each grid cell, the centroids did not align. This gave the illusion of a large difference between the two spacings. Although this also occurred in the corresponding density and temperature figures, it was not that apparent because the values were very close to each other, whereas the velocity varies from 0 m/s to a little

over 50 m/s. In order to compensate for the variation, data points were extracted at the centerline and at a point in the boundary layer ($y = 0.0316$ m), the results of which are illustrated in Figure 5.56. The notation "CL" refers to the data at the centerline where $y = 0$ m, and "BL" represents the data at a fixed point in the boundary layer, namely $y = 0.0316$ m. This notation will be used throughout this section. In the center of the tube, the velocity was found to be 52.9421 m/s for the coarse grid and 52.9466 m/s for the fine grid. This value was not as constant as that found for the inviscid case because the values increased by about 0.49 m/s before decreasing about 0.77 m/s. Since these changes are relatively small, the values found can still be considered a constant value. In the boundary layer at $y = 0.0316$ m, the velocity in regions 3 and 2 begins at approximately 31.5939 m/s for the coarse grid and 31.7949 m/s for the fine grid. The velocity then decreases to a minimum value of 16.9627 m/s and 16.6694 m/s for the coarse and fine grids, respectively, at $x = 0.177134$ m. Once again, the velocity increases at the end of the region to 48.2097 m/s for the coarse grid and 50.5769 m/s for the fine grid. Here is where the largest difference between the coarse and fine grids in the boundary layer occurs. The centerline and boundary layer velocities were found to differ by as much as 36 m/s. This is due to the viscous effects seen at the wall, which retards the speed of the fluid in the boundary layer as the shock wave propagates through the driven tube. The velocities were found to be higher at the beginning of region 3 and the end of region 2 since these are the locations of the expansion and shock waves, respectively. Naturally, the boundary layer is thinner, and thus the velocity at the fixed location $y = 0.0316$ m is higher.

In Figure 5.57, it is shown that for the coarse grid, the inviscid and centerline viscous curves line up very well and differ by only 0.0111 m/s in regions 2 and 3. The fine grid for this section (Figure 5.58) matches even better with a difference of only 0.0006 m/s. As previously mentioned, the velocities near the walls are much smaller than that seen in the center of the tube, differing by as much as 36 m/s for both grids near the region 2 - region 3 interface compared to the centerline velocity. Near the shock wave (or the end of region 2), the fine grids were found to be in better agreement, meaning the centerline, boundary layer, and inviscid velocities were all within 1 m/s of each other (compared with the 3 m/s difference for the coarse grids). As a result, in order to get a full view of what is occurring

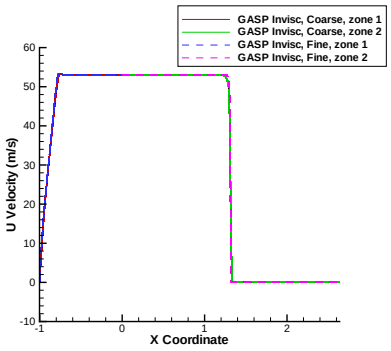

Figure 5.55: Compare u of the grid spacings with inviscid flow at $t = 0.0035$ seconds.

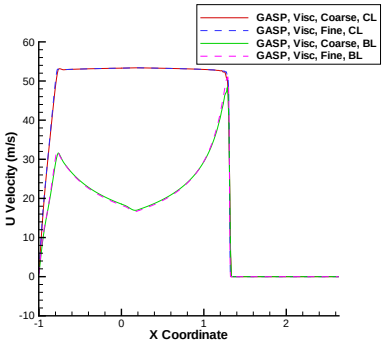

Figure 5.56: Compare u of the grid spacings with viscous flow at $t = 0.0035$ seconds. (Note: CL = centerline, $y = 0$ m; BL = boundary layer, $y = 0.0316$ m)

in the shock tube at any cross section, a viscous flow is required. The fine grid also provides more data points along the huge stretch between 0 m/s and 50 m/s, and therefore should be coupled with the viscous flow for the most complete results from the centerline to the wall.

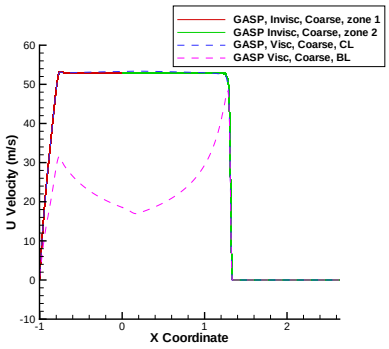

Figure 5.57: Compare u of the flow types with coarse grid spacing at $t = 0.0035$ seconds.

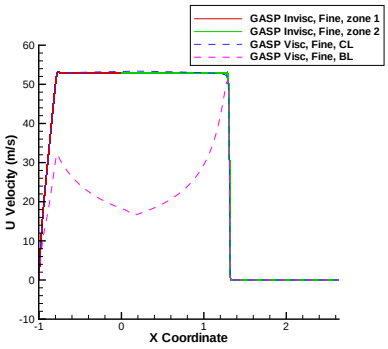

Figure 5.58: Compare u of the flow types with fine grid spacing at $t = 0.0035$ seconds.

As with the pressure, density, and temperature, the region of interest at $t = 0.011$ seconds is the one closest to the driven endwall (region 5). After the large drop in velocity due to the reflected shock wave, the velocity appears to become steady again and close to zero. For the comparison of inviscid flows (Figure 5.59), the coarse grid was found to have a velocity of -0.5941 m/s and the fine grid had a similar velocity of -0.3025 m/s. These values increased by about 1 m/s from the beginning of the region to the end of the region

at the driven endwall. At the endwall, the velocity was 0 m/s, satisfying the conservation laws (because before the shock wave arrived, the velocity was also 0 m/s). Figure 5.60 shows the comparison of the grid spacings for the viscous flow. From $x = 2.16$ m to the endwall (at about $x = 2.64$ m) the centerline velocity for both the coarse and fine grids decreases from approximately 0.6 m/s to 0 m/s, as is to be expected. In the boundary layer (at $x = 2.16$ m), the velocity began at -6.18 m/s for the coarse grid and -6.28 m/s for the fine grid, and increased to approximately 0 m/s. As shown in the figure, the coarse and fine grids were in good agreement, within 0.1 m/s, for their respective y location (either $y = 0$ m or $y = 0.0316$ m). However, the centerline and boundary layer velocities for a given grid spacing (coarse or fine) differed by about 6.8 m/s. It should also be noted that the velocity of the air close to the wall (*i.e.* in the boundary layer) is a little faster than the air in the center of the tube. Although this difference is small here, this topic will be analyzed in another section of this chapter.

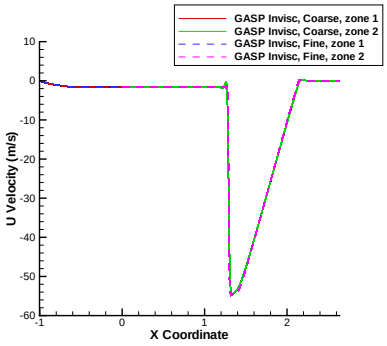

Figure 5.59: Compare u of the grid spacings with inviscid flow at $t = 0.011$ seconds.

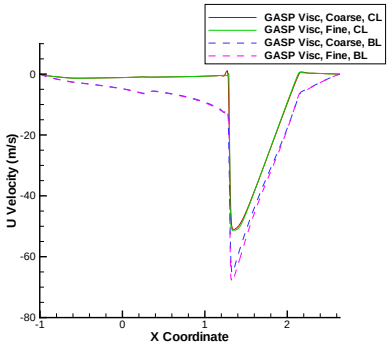

Figure 5.60: Compare u of the grid spacings with viscous flow at $t = 0.011$ seconds.

Figures 5.61 and 5.62 show that the inviscid flow and the centerline viscous flow follow the same trends for the coarse and fine grids. The resulting velocities were found to differ by about 0.5 m/s, which is still in good agreement. The magnitude of the boundary layer velocity was found to be about 6.3 m/s greater for the coarse grid and about 6.5 m/s greater for the fine grid than their corresponding inviscid velocities (at the same x location, $x = 2.15$ m). This can be attributed to the interaction of the reflected wave with the boundary layer, causing the air to travel a little faster in that region, before gradually slowing down to the centerline velocity at a given x location. In summary of the velocity

section, the most accurate description comes from using a viscous flow with a fine grid spacing. This shows how the velocity varies from the wall to the center of the shock tube, whereas the inviscid flow will only describe the properties in the center of the tube and assume that it is uniform throughout the cross-section, which it clearly is not. In conclusion of all of the properties analyzed by GASP, the velocity was found to be the limiting factor in which grid spacing to use (all of the others showed little difference). Also, all were in agreement that the viscous flow provided more information about the changes seen at different locations along the radius of the tube. Hence, the best combination of flow types and grid spacings to use is the viscous flow with a fine grid.

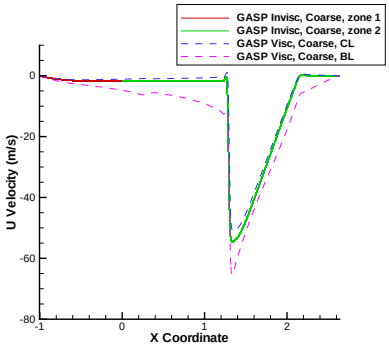

Figure 5.61: Compare u of the flow types with coarse grid spacing at $t = 0.011$ seconds.

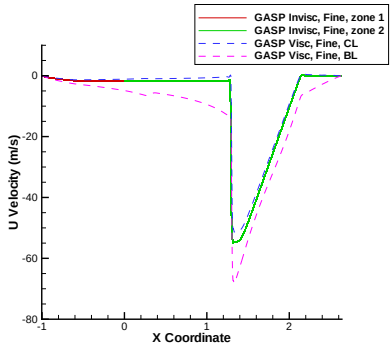

Figure 5.62: Compare u of the flow types with fine grid spacing at $t = 0.011$ seconds.

5.5 Comparisons

5.5.1 Governing Equations with Experiment

In order to compare the averaged experimental results with the averaged theoretical results (obtained from the 1-D governing equations discussed in Chapter 3), the experimental graphs needed to be shifted along the x-axis by about 3.4 ms for both transducers. This is due to the manner in which the experimental pressure traces were recorded. As mentioned in the experimental section, the oscilloscope is triggered to record data when the voltage exceeds a specified amount. Therefore, to compare the experimental results with any of the methods previously discussed, the experimental data must be shifted in time. This was accomplished by aligning the arrival time of the incident shock at the first transducer with

the theoretical result. The results of this shift are illustrated in Figure 5.63 for transducer 1 and Figure 5.64 for transducer 2.

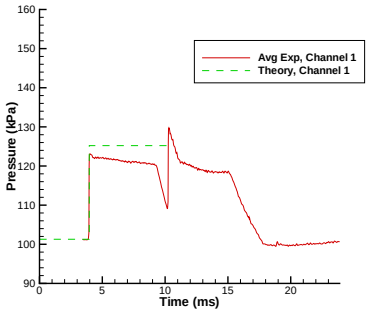

Figure 5.63: Comparison of the experimental and theoretical data from Channel 1.

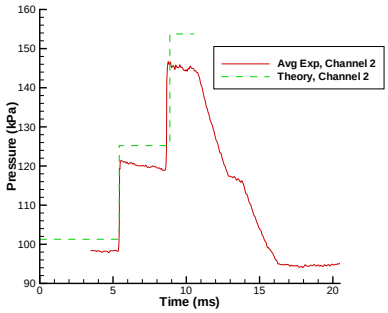

Figure 5.64: Comparison of the experimental and theoretical data from Channel 2.

Table 5.12: Summary of experimental and theoretical results.

	Channel	Experimental	Shifted Experimental	Theoretical	% Error	Shifted % Error
p_1	1	101112 N/m^2	-	101284 N/m^2	0.17%	-
	2	98168 N/m^2	101284 N/m^2	101284 N/m^2	3.08%	0.13%
p_2	1	122541 N/m^2	-	125183 N/m^2	2.11%	-
	2	120803 N/m^2	123919 N/m^2	125183 N/m^2	3.50%	1.01%
p_2/p_1	1	1.21	-	1.24	1.94%	-
	2	1.23	1.22	1.24	0.44%	1.01%
p_5	2	145700 N/m^2	148816 N/m^2	153758 N/m^2	5.24%	3.21%
p_5/p_2	2	1.21	1.20	1.23	1.81%	2.23%
Δt_1	1 & 2	1.45 ms	-	1.46 ms	0.62%	-
Δt_2	2	3.23 ms	-	3.45 ms	6.61%	-
c_s	1	376.63 m/s	-	374.28 m/s	0.63%	-

As shown in Figure 5.63, the initial pressure in the driven section (p_1) was found to match the theoretical (atmospheric) value almost perfectly for the first transducer, as should be expected. The pressure directly behind the shock wave (p_2), had a slightly higher theoretical value than experimental. As shown in Table 5.12, the difference between these two values is approximately 2%, and therefore the results are still relatively close to one another. By taking the ratio of these two pressures (p_1 and p_2), the shock strength can be determined. The shock strength error was found to be similar to that of p_2, since p_2

had more error than p_1 (0.17%). The final point of the theoretical results occurs where the experimental pressure is rising. Recall that this theoretical value was the time when the reflected shock wave reached the pressure transducer. This confirms that the reflected expansion reached the first transducer before the reflected shock and the reason why the pressure drops (due to the reflected expansion) before rising (from the reflected shock).

The initial pressure for transducer 2 in Figure 5.64 illustrates that the theoretical values determined for p_1, p_2, and p_5 were found to be a little higher than the experimental results. Since the initial pressure and the pressure behind the shock wave were found to have similar amounts of error (approximately 3.1% and 3.5%, respectively), this indicates that there is a systematic error, most likely due to a miscalibration of the pressure transducer or a pressure transducer that may need recalibration. The pressure resulting from the reflected shock was found to have about 5% error. From repeated use, the slope of the transducer curve is shifted downwards. If this were compensated for and the graph was shifted in pressure by about 3.12 kPa (to align the p_1) values, the amount of error decreased by 2% or more, as shown in the "shifted" columns of Table 5.12. Note that the p_1 value was used to adjust the graph because it should be reading atmospheric pressure, which is a known value. All in all, the pressure differences between the theoretical and experimental results were very small, and therefore were in good agreement, as well as their resulting pressure ratios (p_2/p_1 had 0.44% error and p_5/p_2 had 1.81%).

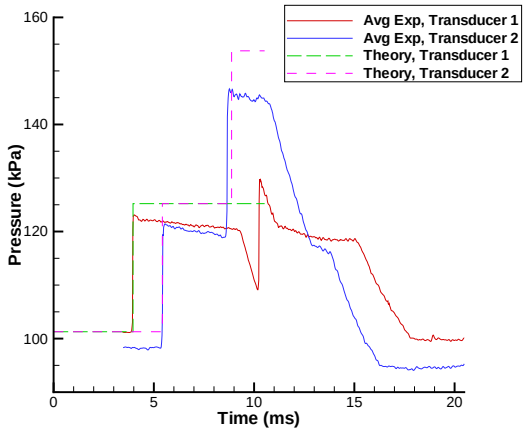

Figure 5.65: Combined experimental and theoretical data from both transducers.

The time differences (Δt_1 and Δt_2) were compared by plotting the experimental and theoretical graphs together (illustrated in Figure 5.65). The time to travel between the two transducers was found to be similar for both the experimental and theoretical results, with less than 1% error. Since the shock speed was calculated by using this time, it yielded a similar amount of error. The time for the shock wave to reach the endwall and reflect back to the final transducer was found to be slightly longer for the theoretical than the experimental time. Since there was such a small difference between the experimental and theoretical values obtained for Δt_1, the 7% error found for the Δt_2 calculations may be, in part, due to viscous effects.

5.5.2 GASP with Experiment

The results of the pressure traces obtained at two locations from GASP, which correspond to the pressure transducer locations in the experimental setup, are plotted with the experimental results in Figures 5.66 and 5.67. As previously mentioned in the Comparison of the Governing Equations with the Experiment section, the experimental results need to be shifted in time since the oscilloscope begins recording data when the system is triggered and not at $t = 0$ seconds. By lining up the first rise times, it was determined that both transducers needed to be shifted by 3.4 ms. These values are the same as that used to shift the theoretical versus experimental graphs, thereby showing the consistency between the theoretical, experimental, and GASP results, and justifies the amount which the experimental data was shift by.

In Figure 5.66, the GASP and experimental results begin at the same pressure (p_1). After the incident shock reaches the first transducer, it sees an immediate rise in pressure. The GASP results show a higher final pressure (p_2) than that determined by the experiment, which the theoretical results also showed. This could have been because of the idealized case that the GASP program was running at in comparison to the actual setup which has imperfections. Although GASP remains constant at this pressure, the experimental data begins to slowly decrease because the transducers can only hold their charge for a given amount of time. The sharp drop in pressure due to the reflected expansion wave occurs at a slightly later time than the experiment, but it is still within good agreement.

The second rise in pressure, when the reflected shock wave reaches the same transducer, again occurs at a slightly later time for the GASP results. For these last two pressure changes, it should be noted that both methods read approximately the same pressure at the extremes. Comparing the remainder of the graph, the trends between them are the same, but the values are different. For instance, the pressure decreases up to the same point as before getting hit by the expansion before leveling off (or for the experiment, attempting to become level). The next section decreases the pressure some more before reaching close to the initial driven pressure (p_1).

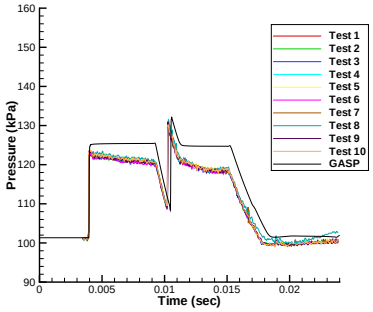

Figure 5.66: Comparison of the viscous GASP and experimental results for pressure at the first transducer for 24 ms.

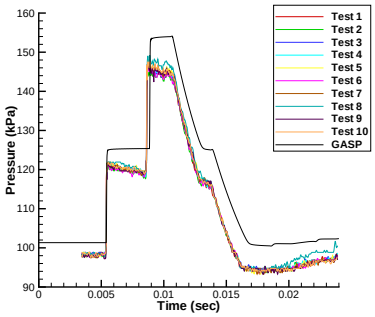

Figure 5.67: Comparison of the viscous GASP and experimental results for pressure at the second transducer for 24 ms.

In Figure 5.67, the experimental and GASP results for transducer 2 begin at different initial pressures (p_1), with the GASP results having a higher pressure, as did the theoretical results. Again, this difference is due to a systematic error with this transducer. As with the first transducer, the pressure increase from the shock wave shows a greater p_2 for the GASP results. Also, the experimental results display a gradual reduction in pressure, most likely from the transducers bleeding off the charge. When the reflected shock wave reaches this transducer, the pressure rises again at almost the same instant for both methods, but the GASP results very slightly lag behind. The new pressure (p_5) is, again, higher for GASP than the experiment. The experimental results also begin slowly declining after reaching their maximum peak at this pressure. Similar to the first transducer, the trends from this point forward match, although the values are different (GASP having a greater pressure than the experiment). The pressure begins decreasing at approximately the same point in

time and plateaus at p_2 for a short time before decreasing to a pressure which is close to the initial driven pressure.

5.5.3 Theory with GASP

Transducers

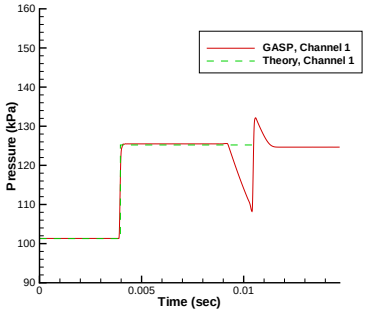

Figure 5.68: Comparison of the viscous GASP and theoretical results for pressure at the first transducer.

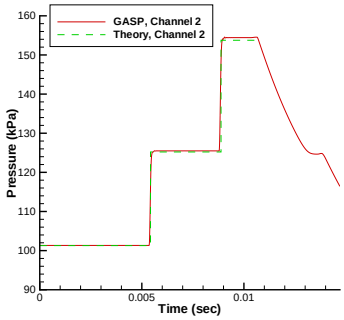

Figure 5.69: Comparison of the viscous GASP and theoretical results for pressure at the second transducer.

In the description of Figures 5.66 and 5.67, there were references made about similarities with the trends of the theoretical results. For a better comparison of the similarities between the theoretical and GASP values, the results were plotted on the same graph and are illustrated in Figures 5.68 and 5.69 for the first and second transducers, respectively. In Figure 5.68, the pressure for both methods begins at p_1, and then rises at the same time (from the incident shock wave). The new pressure, p_2, is slightly lower for the theoretical results than for GASP. Similarly, in Figure 5.69, the initial pressure values are the same, as are the values for p_2. However, after the reflected shock wave reaches the second transducer, the pressure, p_5, is slightly lower for the theoretical method. Since the governing equations become very complicated after this point due to reflections of the expansion and shock waves, the theoretical results end here.

Properties: Pressure, Density, Temperature

The theoretical results were based on the assumption that the flow is inviscid. Since GASP is able to simulate the flow in a shock tube for both the inviscid and viscous case, these

results can be compared to the theoretical ones. It is expected that the GASP inviscid flow should be in the best agreement along with the GASP viscous flow at the center. Although the latter is a viscous flow, the flow in the center of the tube is straighter (*i.e.* parallel to the wall) because it does not see any interaction with the wall. Note that since the theoretical equations are based on inviscid flow conditions, the viscous flow at the wall (where the viscous effects occur) will be ignored. Table 5.13 summarizes the percentages of how the four GASP cases compared with the theoretical results for the pressure, density, and temperature in regions 2, 3, and 5. For the pressure in regions 2 and 3, it was found that the viscous coarse simulation was in the closest agreement, shortly followed by the viscous fine, the inviscid coarse, and the inviscid fine, respectively. A similar comparison was found for p_5, but the inviscid fine grid agreed slightly better than the coarse grid. The pressure results were found to be very similar to each other (differing at most by 0.09%), so the results are inconclusive. The densities in regions 2, 3, and 5 showed that the viscous grid spacings were in the best agreement with the theoretical results, followed by the inviscid cases. The difference between the viscous and inviscid cases were only 0.06% for region 3, 0.05% for region 2, and 0.07% for region 5. The temperature in region 3 showed that the viscous results and the inviscid results were in very good agreement. In region 2, the viscous results were the best followed closely by the inviscid results. In region 5, the difference in results was only 0.04%, with the inviscid results performing slightly better. The temperature, usually determined by using the pressure and density results along with the ideal gas law, demonstrated that the small differences found for the other properties were magnified in the temperature results. It should be noted that this comparison was based on averaged values. For the theoretical results, each of the 10 experimental initial conditions were used to calculate the pressure, density, and temperature for regions 2, 3, and 5. These numbers were averaged together and that final number was used in the comparison. As previously shown for the viscous cases, the regions typically have some slope. The number that was used for comparison with the theoretical results was the average of the highest and lowest point in the region. Overall, the results were found to be in very good agreement for each of the four cases, with the greatest difference between the theoretical and GASP results being 0.51%. Technically, the viscous results at the

centerline were the best of the best, followed closely by the inviscid results, which was a little different than what was predicted. There was also not much difference between the results with regards to spacing (coarse or fine grid), which is probably due to the values being looked at over a region and not at one specific point.

Table 5.13: Comparison of the theoretical and GASP results (% difference).

Item	Inviscid Coarse	Inviscid Fine	Viscous Coarse center	Viscous Fine center
$p_2 = p_3$	0.26	0.27	0.24	0.25
p_5	0.51	0.49	0.42	0.42
ρ_3	0.34	0.34	0.28	0.28
ρ_2	0.20	0.20	0.15	0.15
ρ_5	0.37	0.36	0.30	0.30
T_3	0.07	0.07	0.07	0.07
T_2	0.10	0.10	0.08	0.08
T_5	0.16	0.16	0.12	0.12

5.5.4 Matlab with GASP

The results obtained from Matlab show the property trends that are seen at any location in the shock tube for a given instant of time. The experimental results, on the other hand, record the pressure from two locations (where the transducers lie) over a period of time. Since GASP was programmed to output both types of data, its results will be compared to Matlab.

When the Matlab code was written, it was assumed that the flow is inviscid and that it would be valid up to the point when either the expansion or shock wave reached the endwall. The validity of this assumption is tested against the GASP results, also for the inviscid case, at $t = 0.00147$ seconds and at $t = 0.0029$ seconds. (In another attempt to slightly decrease GASP's run-time, the data was made accurate to 0.0001 seconds, and therefore the previously determined time when the expansion wave reached the endwall at 0.00293 seconds could not be used.) The results of this comparison are illustrated in Figures 5.70 - 5.77 for the pressure, density, temperature, and velocity, respectively, where the Matlab output has been dimensionalized. For each property and time it was

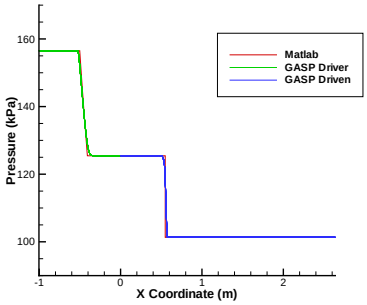

Figure 5.70: Comparison of the Matlab and GASP results for pressure along the shock tube at $t = 0.00147$ seconds.

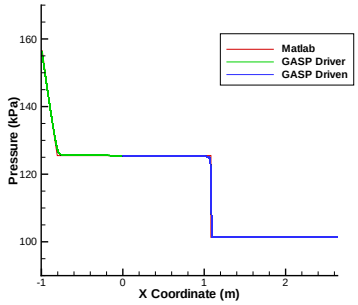

Figure 5.71: Comparison of the Matlab and GASP results for pressure along the shock tube at $t = 0.0029$ seconds.

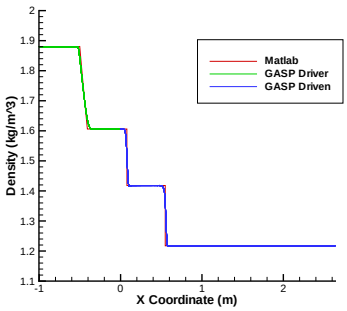

Figure 5.72: Comparison of the Matlab and GASP results for density along the shock tube at $t = 0.00147$ seconds.

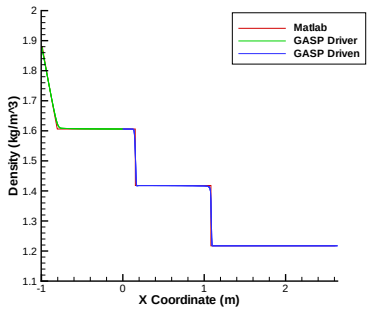

Figure 5.73: Comparison of the Matlab and GASP results for density along the shock tube at $t = 0.0029$ seconds.

shown that both methods yielded the same results. The only difference occurs at the point of change between the five regions (driver, expansion, between the expansion wave and contact surface, between the contact surface and the shock wave, and driven). The Matlab code fits the shock and contact surfaces as the discontinuities (*i.e.* sharp corners), while the GASP code captures them across typically two grid cells.

If the times are compared for each property, it is noticeable that at 0.0029 seconds, the driver region no longer exists and the graph begins with the expansion region. This implies that the expansion wave has reached the endwall (in the driver section), thereby disturbing the originally stationary, undisturbed flow and altering the conditions here. Another observation to make is that the contact surface, depicted by the vertical line close to $x = 0$ m does not move much between the two times. As a result, the regions before and after become elongated for the later time, but still follow the same trend. In

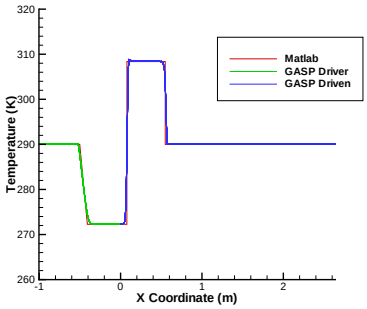

Figure 5.74: Comparison of the Matlab and GASP results for temperature along the shock tube at $t = 0.00147$ seconds.

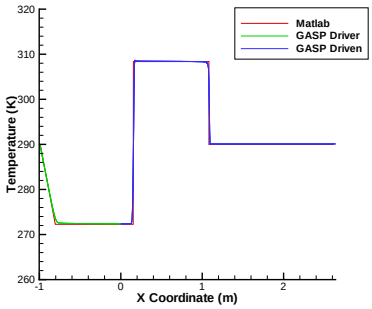

Figure 5.75: Comparison of the Matlab and GASP results for temperature along the shock tube at $t = 0.0029$ seconds.

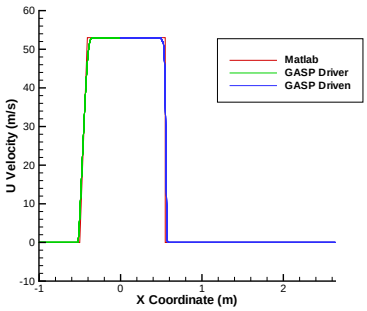

Figure 5.76: Comparison of the Matlab and GASP results for velocity along the shock tube at $t = 0.00147$ seconds.

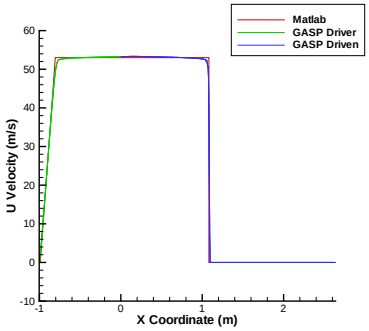

Figure 5.77: Comparison of the Matlab and GASP results for velocity along the shock tube at $t = 0.0029$ seconds.

conclusion, since the GASP and Matlab results matched almost perfectly, and the GASP results matched relatively well to the experimental results, the Matlab results can be said to indirectly match that of the experiment up to $t = 0.0029$ seconds.

5.6 Boundary Layer Effects

As shown in the previous sections of the GASP model, the fine grid with viscous flow provided the most information and will therefore be implemented in this analysis. The pressure plotted with respect to the distance along the shock tube for different times is the best way to track the locations of the expansion wave and shock wave. Figures 5.78 - 5.89 show this progression from $t = 0$ seconds up to $t = 0.011$ seconds, in increments of 0.001 seconds. The purpose of this is to find critical times during the test (such as when

the expansion wave reaches the endwall) and look at the velocity profile to see what is occurring in the boundary layer, comparing the results of the propagating wave with the reflected wave. At $t = 0$ seconds, the initial pressure in the driver and driven sections are illustrated (Figure 5.78), referring to p_4 and p_1, respectively. From this point until about $t = 0.003$ seconds (Figures 5.79 - 5.81), the expansion wave (represented as the first drop in pressure) moves to the left and the shock wave (represented by the second drop in pressure) moves to the right, thereby expanding the spatial extent of regions 2 and 3. At about $t = 0.003$ seconds, the front end of the expansion wave reaches the driver endwall, as is illustrated in Figure 5.81 by the absence of region 4 (the initial driver conditions). By taking incremental times, it was discovered that between $t = 0.0032$ seconds and $t = 0.0033$ seconds, the pressure flips from being greater than the pressure in regions 2 and 3, to being less than it. This indicates that the right-most part of the expansion wave has reached the endwall and begun to reflect back toward the driven section. The reason for the drop in pressure is that although the expansion wave moves to the left, the flow is traveling to the right. The expansion wave, in a way, acts like a vacuum that pulls the air opposite to the direction of the expansion wave. The final pressure that is seen as the result of the expansion passing through (*i.e.* behind the reflected expansion wave) is approximately the atmospheric pressure as shown in Figure 5.82.

From about $t = 0.004$ seconds to $t = 0.007$ seconds, the shock wave and reflected expansion wave travel to the right (see Figures 5.82 - 5.85). Between $t = 0.007$ seconds and $t = 0.0071$ seconds, the pressure changes from being less than that of regions 2 and 3 to being much greater, which is opposite of what was seen for the reflection of the expansion wave. Since the flow is moving to the right at a high speed, when it reaches the end of the tube, it strikes the endwall with a great deal of force, and thereby causes the pressure to increase by about 50 kPa.

From about $t = 0.008$ seconds to $t = 0.009$ seconds (Figures 5.86 - 5.87), the reflected expansion wave continues to move to the right, decreasing the pressure behind it, and the reflected shock wave moves to the left, creating the constant pressure of region 5 behind it. As shown in these figures, regions 2 and 3 decrease with each time step as region 5 begins to increase. At about $t = 0.0098$ seconds, the reflected shock wave and the front end of the

reflected expansion wave meet. The interaction of these waves is illustrated in Figures 5.88 - 5.89 for $t = 0.010$ seconds and $t = 0.011$ seconds, respectively. At $t = 0.010$ seconds, the end of region 5 is curved, whereas at $t = 0.009$ seconds, it was more of a sharper corner. By $t = 0.011$ seconds, it appears that the waves have switched positions, meaning that the expansion is now on the right and the shock is now on the left of the interaction location. This is represented in the figure by the sloped line for the reflected expansion and vertical line for the reflected shock wave. As a result, it appears as though the waves have passed through each other with the reflected shock strength weakened by its interaction with the reflected expansion wave.

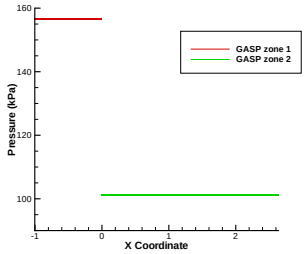

Figure 5.78: Viscous GASP results, $t = 0$ seconds.

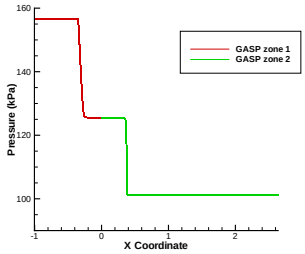

Figure 5.79: Viscous GASP results, $t = 0.001$ seconds.

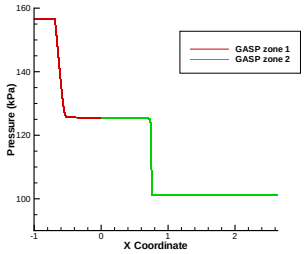

Figure 5.80: Viscous GASP results, $t = 0.002$ seconds.

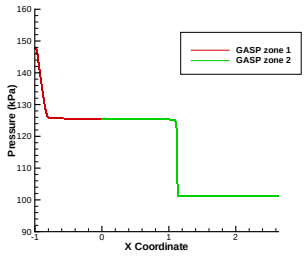

Figure 5.81: Viscous GASP results, $t = 0.003$ seconds.

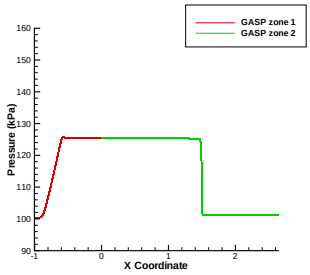

Figure 5.82: Viscous GASP results, $t = 0.004$ seconds.

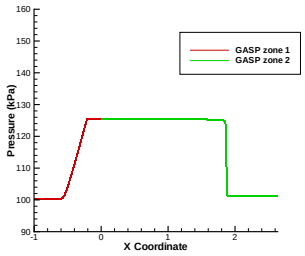

Figure 5.83: Viscous GASP results, $t = 0.005$ seconds.

By looking at these figures and from the previous discussion, two times of interest at two locations along the shock tube will be used to analyze the velocity profile. The first location will be at $x = 0$ m at $t = 0.0032$ seconds (referred to as t_1) and at $t = 0.0068$ seconds (referred to as t_2). The first time is when the expansion wave is just about to reach the

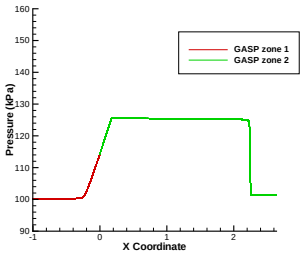

Figure 5.84: Viscous GASP results, $t = 0.006$ seconds.

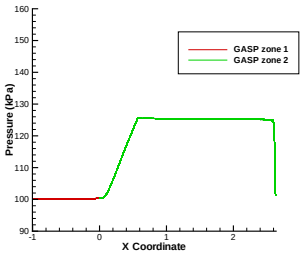

Figure 5.85: Viscous GASP results, $t = 0.007$ seconds.

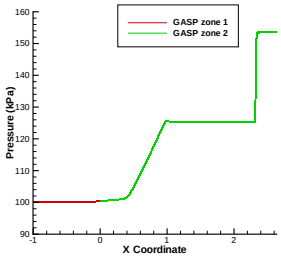

Figure 5.86: Viscous GASP results, $t = 0.008$ seconds.

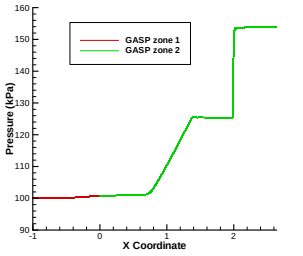

Figure 5.87: Viscous GASP results, $t = 0.009$ seconds.

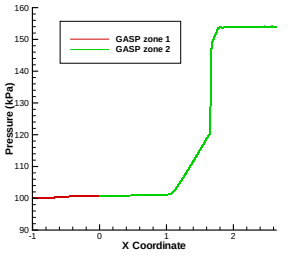

Figure 5.88: Viscous GASP results, $t = 0.01$ seconds.

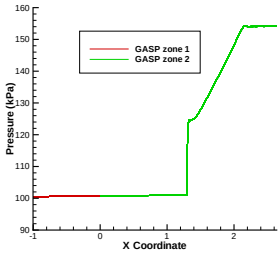

Figure 5.89: Viscous GASP results, $t = 0.011$ seconds.

driver endwall, and the second time is when the left boundary of the expansion reaches $x = 0$ m. By comparing these times, the differences of the expansion wave as it propagates down the tube and when it reflects back will be analyzed. At time t_1, the expansion wave is moving to the left towards the driver end, but the air flow is moving to the right towards the driven end. As a result of this, the velocity profile, shown in Figure 5.91, shows the flow moving to the right. The flow is just about constant at $u = 53.27$ m/s from the center of the shock tube out to a radius of about 0.0307 m. From this y location to the tube wall (approximately one millimeter, where the boundary layer is forming), the velocity decreases to zero at the wall. The large difference in values is due to the interactions with the wall, and is what is typically seen for flow of a fluid in a tube. Here, the no-slip condition causes a boundary layer to form, thereby causing the velocity profile to develop. At the same location after 0.0036 seconds has passed (at t_2), the flow from the centerline out to a radius of about 0.0301 m is still moving to the right, but at the much slower speed of about 1.99 m/s. In the area above this, the boundary layer, the velocity is traveling at a

much greater speed in the opposite direction as shown in Figure 5.93. This flow, known as a wall jet, also looks like the parabolic flow shown before, where at its peak the velocity is approximately -21.71 m/s, and decrease to 0 m/s at the wall. Upon closer inspection, the flow was found to divert up towards the boundary layer, as illustrated in Figure 5.94, in the wake of the reflected expansion wave (meaning x less than 0 m). Between $x = 0$ m and about $x = 0.44$ m, the flow is still angled upward, but to a lesser degree. After this point, the flow is once again directed parallel to the shock tube wall (as would be expected). The arrows in Figure 5.94 represent the velocity in the driver (colored red) and driven (colored green) sections. The trends described above are for the area close to the tube wall. For a constant x location, it was found that as y decreased from the wall to the center of the tube, these velocity vectors gradually began to change from being angled upward towards the boundary layer to being aligned with the axis of the shock tube. If the expansion wave is once again thought of as a vacuum, moving the flow to the right, there must be some air flow moving to the left to maintain the atmospheric pressure. This is why the velocity vectors, although small after the reflected expansion, are showing that the flow is directed into the boundary layer and travels in the opposite direction.

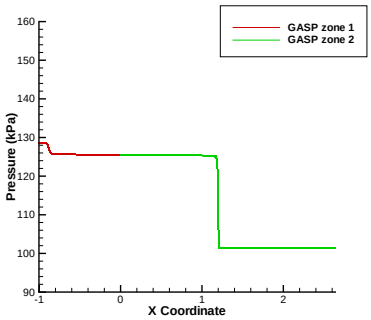

Figure 5.90: Expansion wave reaches the endwall at $t = t_1 = 0.0032$ seconds.

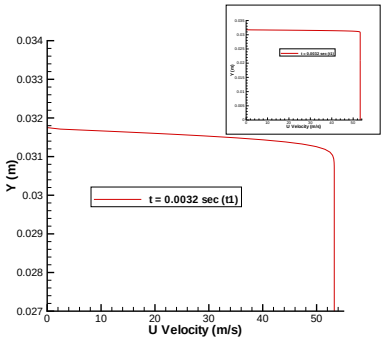

Figure 5.91: Velocity plotted with respect to the y-axis at t_1 and $x = 0$ m.

The second location to be analyzed is at $x = 2$ m at the times $t = 0.0071$ seconds (t_3) and $t = 0.010$ seconds (t_4). Similar to the other location, the first time corresponds to the wave reaching the endwall and the second time is when the reflected wave passed $x = 2$ m. However, this time the wave to be analyzed is the shock wave. At time t_3, the velocity profile (Figure 5.96) shows that the flow from the centerline to a radius of 0.0317 m is

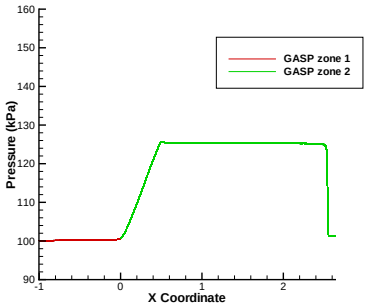

Figure 5.92: Left boundary of the expansion wave reaches $x = 0$ m at $t = t_2 = 0.0068$ seconds.

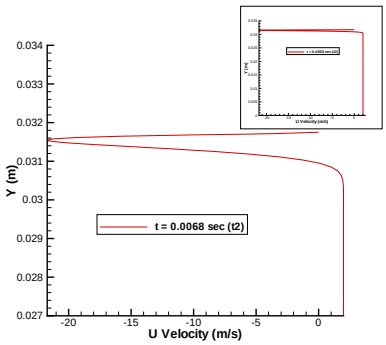

Figure 5.93: Velocity plotted with respect to the y-axis at t_2 and $x = 0$ m.

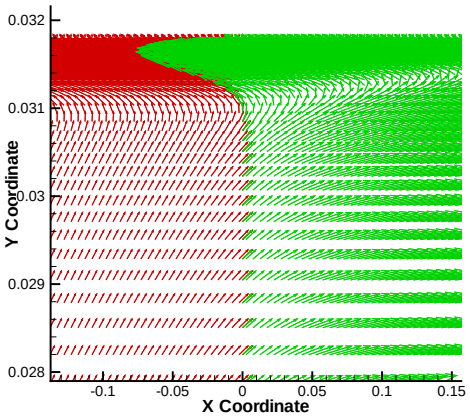

Figure 5.94: Vector diagram of velocity at $t = t_2 = 0.0068$ seconds.

traveling at a speed of about 52.95 m/s. Above this radius to the tube wall, the velocity decreases to zero at the wall. Similar to the expansion wave, the velocity profile is created from the no-slip condition which also leads to the formation of a boundary layer on the driven side. The flow from about $x = 0.55$ m towards the right (the driven endwall), the parabolic flow stretches from the centerline to the shock tube wall. To the left of this point, however, the flow is separated into two regions. The first region is the mainstream flow, which moves to the right as it does after this point. Above this region, closer to the tube wall, the air moves in the opposite direction towards the driver endwall. By looking at Figure 5.95, this point of change is found to lie shortly behind the front end of the reflected

expansion wave.

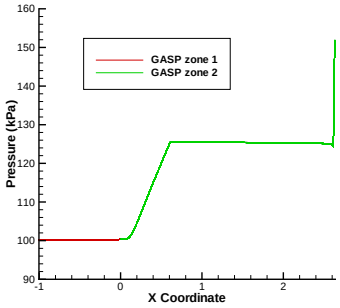

Figure 5.95: Shock wave reaches the endwall at $t = t_3 = 0.0071$ seconds.

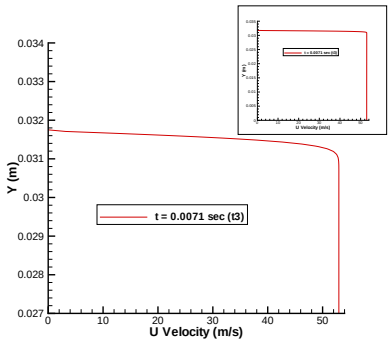

Figure 5.96: Velocity plotted with respect to the y-axis at t_3 and $x = 2$ m.

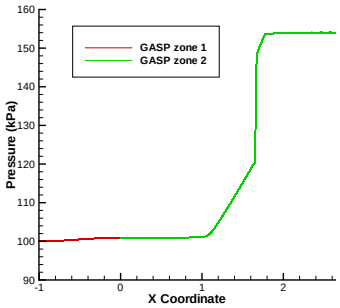

Figure 5.97: Reflected shock passes $x = 2$ m at $t = t_4 = 0.010$ seconds.

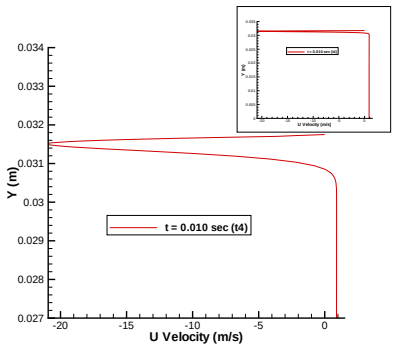

Figure 5.98: Velocity plotted with respect to the y-axis at t_4 and $x = 2$ m.

At time t_4 and location $x = 2$ m, the velocity from the center of the shock tube to a radius of 0.0302 m is found to be traveling to the right (driven end) at a speed of about 0.89 m/s as illustrated in Figure 5.98. The reason why this value is so small is because it is a representation of the net velocity, meaning that the air flowing to the right in the wake of the original shock wave is slightly stronger than the air flowing to the left as a result of the reflected shock wave. In the boundary layer, the velocity was found to travel to the left at -20.93 m/s at the center of the parabolic flow and decrease to 0 m/s at the wall. The parabolic flow in the boundary layer (*i.e.* the wall jet) develops as a result of the shock wave striking the endwall, which changes the pressure from $p_2 = p_3$ to p_5. At this point, the only place for the air to go is in the space between the parabolic shock wave and the tube

wall. Since the flow in the boundary layer was minimal, it allows the flow reflecting off the endwall to move freely and quickly through it. Upon further analysis of the velocity before this point, it was found that at about $x = 1.02$ m, the mainstream flow changes direction, so that before this point it is moving to the left and after it is moving to the right. This phenomenon is most likely due to the interaction of the reflected expansion wave with the reflected shock wave at approximately $x = 1.82$ m. Here, the reflected expansion wave, which has had some time to develop, once again appears as a parabolic flow. The reflected shock, on the other hand, appears as a uniform flow, with a small velocity.

Chapter 6

Conclusions - Future Work

6.1 Conclusion

In conclusion, the ten experimental tests that were performed showed that the results, which were output from the oscilloscope, were consistent with one another. By using the initial pressures from each of these experimental tests, the one-dimensional flow equations were also found to show consistency with the calculated properties. By comparing the properties from the experimental and theoretical results, they were found to be in relative agreement (no more than 7% difference) with one another. The greatest difference for the first transducer was seen for the pressure in region 2, where the theoretical results were about 2.6 kPa greater. Transducer 2, on the other hand, showed the greatest differences, especially for the pressure in region 5 (where the theoretical was 8.1 kPa greater) and the time for the shock to leave the last transducer, reflect off of the endwall, and return to the same location (where it was 0.22 ms greater). Since the pressure ratios (p_2/p_1 and p_5/p_2) for this transducer were in good agreement (less than a 2% difference), it most likely means that there is a consistent error in the calibration of the transducer which is causing this systematic error.

The two computer simulations that were used to model the shock tube were Matlab and GASP. The Matlab results showed the trends for non-dimensionalized pressure, density, temperature, and velocity with respect to the respective property in region 1. These results are only valid up to $t = 0.00293$ seconds, which is when the expansion reaches the endwall. The final time and an intermediate time ($t = 0.00147$ seconds) were compared and the results were found to be consistent with one another. The only difference was that the earlier time had longer 1 and 4 regions, which is not critical since these values are entered into the program to compute the values in regions 2 and 3. GASP used a

geometrically spaced grid (ranging from 0.029 mm to 0.674 mm in the radial direction) rather than a uniformly spaced grid (about 2.6 mm) because the former was able to resolve the boundary layer (approximately 0.31 mm thick) without compromising computational time. The transducer and properties (pressure, density, temperature, and velocity) were analyzed at $t = 0.0035$ seconds (after the expansion reaches the endwall and reflects) and at $t = 0.011$ seconds (after the reflected shock wave passes the final transducer for the second time). At these times, the coarse and fine grid spaces were compared along with the inviscid and viscous flows. In general, the calculated results for the coarse and fine grids matched well. The inviscid flows were found to be stable for each region, meaning that the value was constant from the beginning to the end. However, the viscous flows were found to have a slight slope, either upwards or downwards, depending on the property. Although these differences in the flow types are small, if precise calculations need to be made, it could cause some error. Overall, the best GASP simulation comes from using a combination of a fine grid with a viscous flow. When the Matlab and GASP simulations were compared, they were found to match extremely well. The only difference was found in the corners, where GASP showed a smooth transition from one region to the next but Matlab illustrated sharp corners (discontinuities).

Comparing the experimental results with the transducer output from GASP showed that the experimental results were a little lower than what was predicted by GASP. The reason for this could be that GASP is running under ideal conditions and does not have the imperfections which the experimental setup contains, such as fluctuations in the transducer readings or need for recalibration. Also, the transducers cannot hold their charge for a long period of time, causing the pressure to slowly decline, whereas GASP does not. The GASP results were also compared to the theoretical results for the transducer outputs and for the properties. The former showed that the theoretical results were found to be a little less than the GASP results, but still within very good agreement. When the properties in regions 2, 3, and 5 were compared, it was observed that the viscous flow in the center of the tube with either grid spacing was found to match the theoretical results the best, followed closely by the inviscid flow with either grid spacing. The viscous flow at the tube wall was found to be less consistent, which proves that the boundary layer has different properties

than the mainstream flow. Upon closer inspection of the boundary layer, it was found that when the waves reached the endwall and reflected back, a wall jet was created in the boundary, which did not exist for the propagating waves. It was also shown that the wall jet moves in the opposite direction of the mainstream flow. This is due to the mainstream flow being represented as a net flow, so although it appears as if it is traveling slowly, it is actually traveling at a great speed while going against another flow which is slightly slower. Overall, the inviscid flow is a good assumption for determining the properties in the center of the tube, but at the wall, a viscous flow is necessary in order to show the differences in boundary layer flow compared to the mainstream flow.

6.2 Future Work

All of the tests described previously have been for a constant set of initial conditions, namely $p_4 = 22.69$ psia (or 156483 N/m^2) and $p_1 = 14.69$ psia (or 101325 N/m^2). It would be interesting to see how adjusting the pressure ratio of p_4/p_1 will change the results. For example, if a greater pressure ratio (*i.e.* a stronger shock) were used, perhaps it would create a lambda shock. Another study could be done to further analyze the effects of the interaction of the reflected expansion wave with the reflected shock wave.

Appendix A

Reflected Pressure Ratio Derivation

The reflected pressure ratio (p_5/p_2) was derived from the continuity equation (Eq A.1) and the momentum conservation (Eq A.2) equations [8].

$$\rho_2(W_r + u_p) = \rho_5 W_r \tag{A.1}$$

$$p_2 + \rho_2(W_r + u_p)^2 = p_5 + \rho_5 W_r^2 \tag{A.2}$$

By solving Eq A.1 for ρ_5 and substituting it into Eq A.2, results in Eq A.3.

$$p_2 + \rho_2(W_r + u_p)^2 = p_5 + \left[\frac{\rho_2}{W_r}(W_r + u_p)\right] W_r^2 = p_5 + \rho_2(W_r + u_p)W_r \tag{A.3}$$

Rearranging Eq A.3 results in Eq A.4.

$$p_2 + \rho_2(W_r + u_p)^2 - \rho_2(W_r + u_p)W_r = p_5 \tag{A.4}$$

Dividing Eq A.4 by p_2 and expanding gives Eq A.5.

$$\frac{p_5}{p_2} = 1 + \frac{\rho_2}{p_2}[W_r^2 + 2W_r u_p + u_p^2 - (W_r^2 + W_r u_p)] = 1 + \frac{\rho_2}{p_2}(W_r u_p + u_p^2) \tag{A.5}$$

Substituting the ideal gas law ($p = \rho RT$) into Eq A.5 for the ratio of density over pressure yields Eq A.6.

$$\frac{p_5}{p_2} = 1 + \frac{u_p}{RT_2}(W_r + u_p) \tag{A.6}$$

The variable u_p is defined as the mass motion induced by the moving shock wave, which is equivalent to the velocity of the air behind the shock wave, defined as u_2. The equation for the Mach number of the reflected shock wave (M_r) can be rearranged as shown in Eq A.7.

$$M_r = \frac{W_r + u_2}{a_2} = \frac{W_r + u_2}{\sqrt{\gamma R T_2}} \Longrightarrow W_r + u_2 = M_r \sqrt{\gamma R T_2} \tag{A.7}$$

Eq A.7 and $u_p = u_2$ can be inserted into Eq A.6 to yield Eq A.8.

$$\frac{p_5}{p_2} = 1 + \frac{u_2}{R T_2} M_r \sqrt{\gamma R T_2} = 1 + u_2 M_r \sqrt{\frac{\gamma}{R T_2}} \tag{A.8}$$

The definition of the temperature ratio (T_2/T_1) is restated in Eq A.9.

$$\frac{T_2}{T_1} = \frac{1 + \frac{\gamma-1}{\gamma+1}\frac{p_2}{p_1}}{1 + \frac{\gamma-1}{\gamma+1}\frac{p_1}{p_2}} = \frac{(\gamma+1) + (\gamma-1)\frac{p_2}{p_1}}{(\gamma+1) + (\gamma-1)\frac{p_1}{p_2}} \tag{A.9}$$

The definition for the speed of sound ($a = \sqrt{\gamma R T}$) can be rearranged to solve for T_1. Solving Eq A.9 for T_2, substituting in the equation for T_1, and taking the inverse results in Eq A.10.

$$\frac{1}{T_2} = \frac{(\gamma+1) + (\gamma-1)\frac{p_1}{p_2}}{(\gamma+1) + (\gamma-1)\frac{p_2}{p_1}} \frac{\gamma R}{a_1^2} \tag{A.10}$$

Multiplying Eq A.10 by γ/R and taking the square root of the quantity yields Eq A.11.

$$\sqrt{\frac{\gamma}{R T_2}} = \frac{\gamma}{a_1} \sqrt{\frac{(\gamma+1) + (\gamma-1)\frac{p_1}{p_2}}{(\gamma+1) + (\gamma-1)\frac{p_2}{p_1}}} \tag{A.11}$$

Eq A.11 can now be substituted into Eq A.8 to produce Eq A.12.

$$\frac{p_5}{p_2} = 1 + M_r \left[\left(\frac{p_2}{p_1} - 1 \right) \sqrt{\frac{2/\gamma}{(\gamma+1)\frac{p_2}{p_1} + (\gamma-1)}} \right] \left[\gamma \sqrt{\frac{(\gamma+1) + (\gamma-1)\frac{p_1}{p_2}}{(\gamma+1) + (\gamma-1)\frac{p_2}{p_1}}} \right] \tag{A.12}$$

In order to more easily simplify this equation, the following represention will be used: $A = p_2/p_1$, $P = \gamma + 1$, and $N = \gamma - 1$. Placing this into Eq A.12 yields Eq A.13.

$$\frac{p_5}{p_2} = 1 + M_r(A-1) \sqrt{\frac{2\gamma}{PA+N}} \sqrt{\frac{P+N/A}{P+NA}} = 1 + M_r(A-1) \sqrt{\frac{2\gamma}{A(P+NA)}} \tag{A.13}$$

Replacing A, P, and N with their corresponding variables, yields the final equation, Eq A.14.

$$\frac{p_5}{p_2} = 1 + M_r \left(\frac{p_2}{p_1} - 1 \right) \sqrt{\frac{2\gamma}{\frac{p_2}{p_1}\left[(\gamma + 1) + (\gamma - 1)\frac{p_2}{p_1} \right]}} \tag{A.14}$$

Appendix B

Example Grid Generation Data Points and Figure

```
2
2       2
3       2
0.0
0.5
0.0
0.5
0.0
0.0
0.25
0.25
0.5
1.0
1.5
0.5
1.0
1.5
0.0
0.0
0.0
0.25
0.25
0.25
```

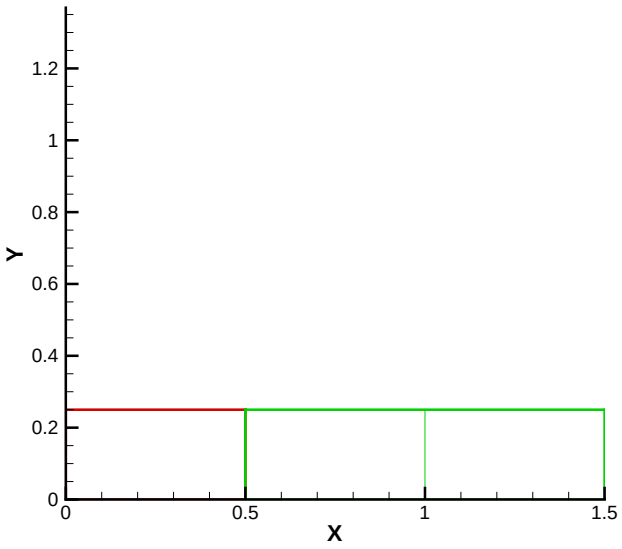

Figure B.1: Sample grid (above) and data points (left).

References

[1] Anatomy of the concorde. http://www.pbs.org/wgbh/nova/supersonic/anatomy.html.

[2] Concorde. http://www.picture-newsletter.com/concorde/index.htm.

[3] F-22 raptor achieves first supersonic flight. http://www.boeing.com/news/releases /1998/news_release_981012n.htm.

[4] F-22 raptor begins first overseas deployment. http://www.aerospacenews.com /content/view/369/44/.

[5] Aerosoft Inc. *GASP Version 4 Technical Reference.*

[6] Aerosoft Inc. *GASP Version 4.1.2 Reference Guide.*

[7] Aerosoft Inc. *A Space-Marching Tutorial*, Dec 2006.

[8] J.D. Anderson. *Modern Compressible Flow, with Historical Perspective.* McGraw Hill, New York, 1982.

[9] V. Daru and C. Tenaud. Numerical simulation of the viscous shock tube problem by using a high resolution monotonicity-preserving scheme. *Computers & Fluids*, June 2008.

[10] D. Knight. *Elements of Numerical Methods for Compressible Flows.* Cambridge University Press, New York, 2006.

[11] P. Kundu and I. Cohen. *Fluid Mechanics.* Elsevier Inc., New York, 3rd edition, 2004.

[12] H. Liepmann and A. Roshko. *Elements of Gasdynamics.* John Wiley, New York, 1956.

[13] H. Mark. The interaction of a reflected shock wave with the boundary layer in a shock tube. *Journal of the Aeronautical Sciences*, 24(4):304–306, April 1957.

[14] P. Oosthuizen and W. Carscallen. *Compressible Fluid Flow.* McGraw Hill, New York, 1997.

[15] H. Reichenbach. Visualization of shock waves in layered media. *High Speed Photography and Photonics*, Volume 1032:837–844, 1988.

[16] A.H. Shapiro. *The Dynamics and Thermodynamics of Compressible Fluid Flow*, volume 1. The Ronald Press Company, New York, 1953.

[17] H.M. Glaz R.E. Ferguson W.J. Glowacki, A.J. Kuhl. Shock wave interaction with high sound speed layers. *Shock Waves and Shock Tubes: Proceedings of the Fifteenth International Symposium on Shock Waves and Shock Tubes*, pages 187–194, 1985.

[18] C.M. Gourlay X. Ligong and R.J. Stalker. Reduction of driver gas contamination in a reflected shock tube by boundary layer suction. *Shock Tubes and Waves: Proceedings of the 16th International Symposium on Shock Tubes and Waves*, pages 637–643, 1987.